# MEASUREMENT AND ANALYSIS OF ERROR IN RIGID-BODY POINT-BASED REGISTRATION SYSTEMS

By

Ramya Balachandran

Dissertation

Submitted to the Faculty of the

Graduate School of Vanderbilt University

in partial fulfillment of the requirements

for the degree of

DOCTOR OF PHILOSOPHY

in

Computer Science

May, 2008

Nashville, Tennessee

Approved:

John Michael Fitzpatrick

Benoit M. Dawant

Robert E. Bodenheimer

Gautam Biswas

Robert F. Labadie

**ACKNOWLEDGEMENTS**

I would like to thank all my committee members for their support throughout my dissertation research. I would like to first thank Dr. Fitzpatrick for being such a great advisor. This dissertation would not have been possible without his guidance and support. I always enjoyed and will continue to enjoy all the exciting research discussions. During every discussion, I always learn something new from him. He also took efforts to improve my writing skills. I am really grateful for his invaluable help during the past few months when I was trying to finish my dissertation and decide on my career. I would like to thank Dr. Labadie for his great support. I am really fortunate to have the opportunity to work in many exciting research projects with him. I am always inspired by his positive approach to problems. I appreciate his help with my dissertation and his support in getting me the research position. I would like to thank Dr. Dawant for his guidance and support. He always motivated research in various directions through frequent research meetings. His suggestions and ideas were useful to my dissertation work. I would like to thank Dr. Bodenheimer for his valuable input in my research. I appreciate his effort to find the necessary references that guided me in the right direction after the proposal. I would like to thank Dr. Biswas for being part of my committee and for his effort and time. I would also like to thank Dr. Cheng for his support and encouragement.

I would like to express my sincere thanks to Dr. Fitzpatrick, Dr. Labadie, Dr. Dawant, and Dr. Cheng for providing financial support during my studies. I would also like to thank Dept. of EECS for offering me teaching assistantship during a semester and Dept. of Otolaryngology for offering me a full-time research position.

I would like to thank all the past and present members of the Medical Image Processing Laboratory. They made my graduate student life really exciting. I would like to specially thank Dr. Duane Yoder for his assistance during the first few months of my stay in Nashville. I would

like to thank Sandy Winters and Linda Koger for handling all the administrative issues. I would like to thank all the members of Dr. Labadie's research group for their support over the past few years. I would also like to thank all the technicians who assisted me with data acquisition, and patients who participated in the research studies for my dissertation.

I would also like to thank all my friends and well-wishers in USA and in India, in particular Shaivya, for their support. I am happy that I made some really good friends during my stay in Nashville.

Last but not least, I would like to thank my parents and my brother for their love and support. They always agree to the decisions I make and support me in every possible way they could. Without their love, support, and understanding, I would not have been able to achieve this success in my life. Their happiness for every achievement of mine encourages me to always aim for more.

I am very grateful to all these good people, who helped me in the successful completion of my dissertation.

**TABLE OF CONTENTS**

Page

## LIST OF TABLES

Table Page

## LIST OF FIGURES

Figure Page

# CHAPTER I

## INTRODUCTION

Registration, as defined in [1, 2], is the determination of a geometrical transformation, or "mapping", that aligns points in one view of an object with corresponding points in another view of that object or another object. When the transformation preserves all distances, it is referred to as a rigid registration. In the absence of such a restriction, it is referred as non-rigid registration. In this dissertation we will be concerned only with rigid registration. So the term "registration" from now on will refer to rigid registration unless otherwise specified.

The invention of three dimensional imaging techniques, like computed tomography (CT), magnetic resonance (MR), positron emission tomography (PET) and single photon emission computed tomography (SPECT), marked the beginning of major advancements in the medical imaging field. A detailed explanation of the major medical imaging techniques can be found in [3]. The term "modality" is used to refer to the method by which the images are acquired. The first modality to be invented was the CT by Hounsfield in early seventies. A three-dimensional CT volume of an object is constructed using a series of X-ray projections of the object acquired at known positions and orientations [4, 5]. MR imaging [6-8] was also invented in the early seventies and depends on the response of hydrogen atoms in the human body to magnetic fields. A detailed explanation of the basics of MR images can be found in [9].

Each of these modalities is good at defining certain information. Bone detail can be seen well in the CT images, but information about soft tissues is limited. On the other hand, typical MR images give a lot of information about the soft tissues and less information about bone. PET and SPECT images provide functional information, like cellular activity, but little anatomical information. Surgeons and radiologists usually refer to images of two or more different modalities

to obtain all the information they require. The use of information from these different images is facilitated by aligning them. This alignment was done manually until the early eighties, and is very difficult, especially if the two images were obtained using different modalities, and/or in different orientations. Registration techniques can be used to align these images. This type of registration is called *image-to-image registration*.

Registration can also be used to provide a mapping between an image and physical space. This type of registration is called *image-to-physical registration*. It facilitates surgical navigation, also called *image-guided surgery* (IGS), which is most often used in neurosurgery. A survey of the use of image-guidance in surgery was published by Peters in 2006 [10].

An overview of registration methods is reported in survey papers on medical image registration by Maurer *et al.*in 1993 [11], Maintz *et al.* in 1998 [12], Pluim *et al.* in 2003 [13], and Crum *et al*. in 2004 [14]. All the registration methods aim at minimizing some kind of cost measure. Some examples of cost measure include

(1) distance between two corresponding surfaces (*surface-based methods*),

(2) distance between two set of corresponding points (*point-based methods*), and

(3) dissimilarity in intensity patterns of corresponding volume elements (voxels) (*intensity-based methods*).

Any of these methods could be used for registering a pair of images of the same or different modalities. The first two methods can be used for image-to-physical registration, while the third is limited to image-to-image registration.

Surface-based methods [15- 20] involve determining corresponding surfaces in the two spaces (image or physical). A transformation is found that best aligns these two surfaces. The "Head and hat" and the "Iterative closest point" (ICP) algorithms are the best known and most commonly used algorithms for surface-based registration. The surface details are extracted from an image volume using segmentation techniques. In the physical space, the surface detail is usually obtained by laser scanning the surface.

Point-based methods [1, 21-26] align points in two different spaces by minimizing the least-squares distance between corresponding points. The corresponding points might be obtained by manually selecting corresponding landmarks in the two spaces, but the most common and most effective method is to use markers that can be localized in both the spaces. Closed-form solutions are available to determine the transformation that minimizes the least-squares distance between corresponding points [27- 38].

Intensity-based methods [39-44], also known as *volume-based methods*, minimize dissimilarity or maximize similarity in the intensity patterns of corresponding voxels. Some of the measures used in these methods are correlation, entropy, joint entropy, mutual information, and normalized mutual information. The transformation that optimizes (minimize/maximize) the similarity measure is found. Mutual information is the most commonly used measure. (See Pluim *et al*. for a survey of its use [13].) These methods usually require preprocessing of images and are iterative in nature. Hence, they take a long time for the registration process. Intensity-based methods cannot be used for image-to-physical registration because of the non-availability of intensity values in physical space.

For IGS systems, one of the spaces is the patient's CT or MR image, and the other space is the patient in physical space. A CT and/or MR scan is done before the surgery. Image-to-image registration techniques (surface-based, point-based, or intensity-based methods) can be used to combine the information from different modality images. Then in the operating room, image space and physical space are related using one of the many available image-to-physical space registration methods—either surface-based or point-based. Then when the surgeon operates on the patient, the tip of surgical tools can be tracked in real-time, and their corresponding positions can be displayed in the image space(s). By viewing that display, the surgeon can decide how to proceed with the surgery. Thus, it is important that the position of the tool be displayed accurately at the corresponding position. An error in the mapping could mislead or confuse the surgeon.

The technique of image-guided surgery was used even before CT or MR imaging techniques were invented. The first use of this technique was in 1906 by Horsley and Clarke [45, 46] with animal subjects. They used a stereotactic frame to rigidly fix the head of the animal. Anatomical drawings were used as images and were used to reach the brain. In 1947 Spiegel [47] reported the first human surgery to be performed in this way. Since then image-guided surgery has become more and more common in the areas of neurosurgery.

IGS is comparatively new in the field of otologic surgery. IGS techniques are especially applicable for otologic surgery because of the fact that the temporal bone, which protects the ear, is rigid. The surgical target region is surrounded by the temporal bone and hence can be assumed to be a rigid object. This rigidity is the same advantage that has made IGS techniques common in brain surgery. There is the entire skull protecting the deformable brain that make the brain behave, at least for minimally invasive surgery, as if it were rigid. The temporal bone protects critical structures such as the facial nerve, the inner ear, the floor of the cranial vault, the internal jugular vein, and the carotid artery. Ear surgery, performed via a mastoidectomy, involves drilling out portions of the mastoid, which is a portion of the temporal bone. Any error in the drilling could damage any of these critical structures resulting in undesired results. Some of the undesired results include paralysis of the face (damage to facial nerve), hearing loss and vertigo (damage to the inner ear), leakage of cerebrospinal fluid (CSF) (damage to the cranial vault), and life threatening blood loss (damage to the internal jugular vein and carotid artery) [48]. When IGS techniques are used, the surgeon can pre-plan the path for drilling using the CT and/or MR images, visualize it during the drilling in the image space with the help of the display, and modify the path during the surgery if needed. Without registration between image and physical space, the surgeon will have to mentally visualize the situation and compare with the images. Thus registration can play an important role in real-time visualization provided to the surgeons.

It is important, however, to realize that errors are inevitable in any IGS system and not to rely on them completely. The point displayed in the image space corresponding to the point in the

physical space is usually not perfect. There are various errors involved, which we will see later, that will not allow it to be perfect. The aim of IGS systems is to have this error to be as small as possible (submillimetric if possible) in order to reduce the likelihood of any damage to critical structures.

Invasive fiducial systems are known to provide submillimetric accuracy [25]. They require that markers be implanted into bone so that they are rigidly attached to it. These markers are localized in image and physical space and used to perform point-based registration. Because of their invasiveness, they are usually used only for malignant cases. For non-malignant cases, such as those common in ear surgery, it is important to find accurate non-invasive fiducial systems. One possible solution is to use skin-affixed markers, but they are less accurate because the skin has a tendency to move relative to the skull. The most optimistic claims of accuracy are in the range of 1.5 mm or higher [48]. Another possible solution is to use surface-based registration by measuring the contours of the skin with a laser in the operating room. Because the skin and tissues deform, this method is also not accurate. The accuracy is in the range of 2.5 mm or higher [49]. We have designed a non-invasive fiducial system for image-guided otologic surgery. Our aim is to achieve accuracy with a non-invasive fiducial system that is comparable to that we get with invasive systems. In a later chapter of this dissertation, the non-invasive system will be described in detail.

Apart from providing visualization, the IGS approach can also be used to facilitate minimally-invasive surgery. The pre-planning process enables the surgeon to plan the surgery such that the amount of drilling needed is minimized. Though this finds application in various fields of surgery, in this dissertation we will look at one possible application in deep-brain-stimulation (DBS) surgeries. DBS procedures involve implanting electrodes deep within the brain to electrically stimulate target nuclei [50, 51]. They are used for treating patients with Parkinson's disease and essential tremor. Because of the small target region, the implantation must be performed with submillimetric accuracy [52]. Targeting frames, or "platforms", are available that

can be used to guide these procedures [53]. Before the platform can be employed, anchors must be implanted into the patient's skull, after which a CT scan is obtained. Based on the locations of the anchors and the target path, a platform is custom made. The platform fits on the anchors such that when a guide is attached to the frame, it aims at the target. More details about these platforms and their accuracy will be discussed later in this dissertation.

### 1. Definition of Errors

In this dissertation we will concentrate on fiducial systems that employ rigid-body, point-based registration. For performing the registration it is important to find corresponding points to be registered. Such points, when used for registration, are referred to as *fiducial points* or just *fiducials*. Errors occur while localizing these points, and those errors lead to other errors. This dissertation will mainly focus on the errors involved in fiducial systems. Thus, it is helpful to provide precise definitions of each type of error.

Fiducial Localization Error (FLE): Point-based registration involves localizing fiducial points in the two spaces before registering them. The localization of the fiducial points is known to be inaccurate, and the error made in this process is termed *Fiducial Localization Error* (FLE). This error is the cause of further errors in the registration process. Each point used in the registration process can be expected to have a fiducial localization error associated with it. The most common definition is that FLE is the Euclidean distance between estimated fiducial points and the true point. In vector sense it is the vector displacement from the true point to the estimated one.

Fiducial Registration Error (FRE): Due to the presence of error in localizing the fiducials, the corresponding fiducial points do not align perfectly after the registration, and the error in their alignment is called *Fiducial Registration Error* (FRE). We can measure the vector displacement

between corresponding fiducials and also the magnitude which is the Euclidean distance between corresponding fiducial points after registration.

Target Registration Error (TRE): Targets are any points that are not fiducial points, i.e., those not used for the registration. The term "target" is used because such points are typically of interest only if they are the target of diagnosis or surgery. The targets also do not align properly like the fiducials after registration because of the presence of FLE. The Euclidean distance between corresponding targets after registration is termed *Target Registration Error* (TRE). In some cases the vector displacement between corresponding targets is given; in others only the magnitude is of interest.

Figure 1 shows a schematic to explain these errors. FLE, FRE, and TRE are here depicted as vector quantities, but they are often reported as scalar values and in statistical reporting the root-mean-square (RMS) values are most common. TRE is the best measure of the accuracy of a system. It is this value that is important to the surgeon or diagnostician.

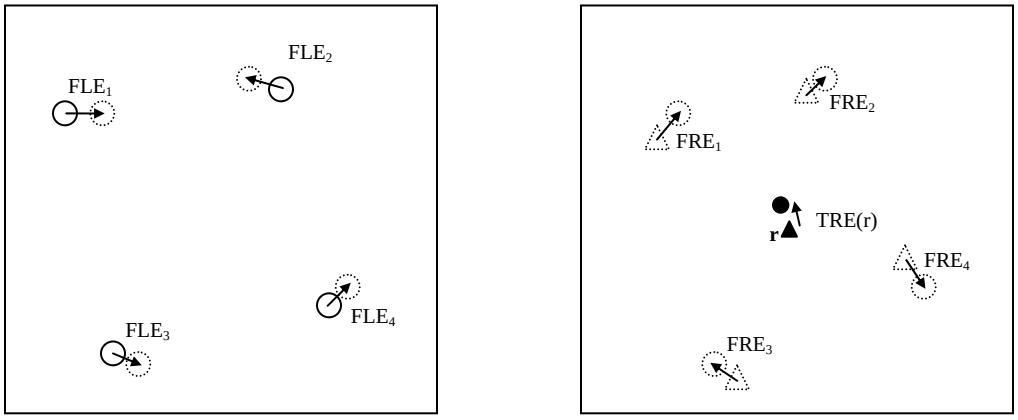


**Figure 1.** Schematic showing various errors in registration. Solid circles represent true position of the fiducials. Dotted circles represent the localized position of the fiducials in space 1. Dotted triangles represent the fiducials transformed from Space 2 (not shown) to Space 1 after registration. The filled circle is the true location of the target. The filled triangle is the target transformed from Space 2 to Space 1 after registration.

## 2. Rigid-body Point-based Registration

The first step in rigid-body, point-based registration is to find the position of the corresponding fiducial points in the two spaces (image and physical spaces, two image spaces, or two physical spaces). Suppose there are *N* fiducial points. Let $\{\mathbf{x}_i\}$ and $\{\mathbf{y}_i\}$, $i = 1, 2, ..., N$ be a set of *N* three-dimensional vectors representing *N* corresponding fiducial points in the image and physical space respectively. (Note that we will use a nonbold font for matrices and scalars, and a bold font for vectors. All vectors are column vectors unless they are transposed. Components of matrices and vectors are in nonbold font as they are scalars. $\langle . \rangle$ will be used to represent expected values.)

A rigid transformation is represented by a 3-by-3 rotation matrix, *R* and a 3-by-1 translation vector, **t**. The transformation, *R* and **t**, is found such that the weighted least-squares distance between the corresponding fiducial points after registration is minimized. Thus, the problem is to find *R* and **t** that minimizes the weighted fiducial registration error

$$\mathrm{FRE}^2 = \frac{1}{N}\sum_{i=1}^{N} w_i^2 \left| R\mathbf{x}_i + \mathbf{t} - \mathbf{y}_i \right|^2, \tag{1}$$

where $w_i$ represents weighting for the $i^{\text{th}}$ fiducial marker and is usually selected based on the FLE for that marker, $\mathbf{F}_i$. The FLE is usually assumed to be isotropic and distributed normally with zero mean and variance $\sigma_i^2$ in each direction, i.e., $\mathcal{N}(0, \sigma)$. Then minimizing Eq. (1) with $w_i^2 = 1/\sigma_i^2$ gives the optimum registration. The transformation represented by *R* and **t** is an "affine" transformation. To limit the affine transformation to a rigid one, the rotation matrix *R* must be orthogonal. The minimization of Eq. (1) for orthogonal *R* is known as the "Orthogonal Procrustes Problem" in the statistics literature, and the "Absolute Orientation Problem" in photogrammetry and robotics. Closed-form solutions are known to exist for this problem. The first solution was given by Green [27]. Later many other solutions were published [28-38]. These solutions include computing rotation matrices using singular-value decomposition (SVD)

introduced by Schönemann [28] or finding unit quaternions to represent rotations [32, 33, 35]. We will follow a simple solution that is described in [1] that uses SVD of the cross-covariance matrix of the fiducial positions.

## 3. Known Error Measures

Fiducial registration error (FRE) can be easily measured directly after registration. FLE on the other hand, can only be estimated statistically. It is typically assumed to be random, isotropic, independent, and identical for all $N$ fiducials in a given space. Suppose the fiducial localization error for a particular marker is different in the two spaces. Let $\left\langle \mathrm{FLE}_1^2 \right\rangle$ and $\left\langle \mathrm{FLE}_2^2 \right\rangle$ be the expected squared fiducial localization error in the two spaces. Then the expected total fiducial localization error is related to the individual ones as follows [54]:

$$\left\langle \mathrm{FLE}^2 \right\rangle = \left\langle \mathrm{FLE}_1^2 \right\rangle + \left\langle \mathrm{FLE}_2^2 \right\rangle . \tag{2}$$

While the individual FLE components in the different spaces cannot be measured directly, Sibson in 1979 [55] found the following approximate relationship between the overall FRE and FLE, which can be used to estimate the expected value of the total FLE. The relationship is

$$\left\langle \mathrm{FRE}^2 \right\rangle = (1 - 2/N)\left\langle \mathrm{FLE}^2 \right\rangle . \tag{3}$$

We can note from this equation that the overall FRE is independent of the fiducial configuration.

An equation for TRE was found in 1998 by Fitzpatrick *et al.* [56]. At any target position **r**, the expected value of squared TRE is approximately given by

$$\left\langle \mathrm{TRE}^2(\mathbf{r}) \right\rangle = \left\langle \mathrm{FLE}^2 \right\rangle \left( \frac{1}{N} + \frac{1}{3} \sum_{i=1}^{3} \frac{d_i^2}{f_i^2} \right), \tag{4}$$

where $d_i^2$ is the squared distance of the target **r** from the principal axis $i$, and $f_i^2$ is the sum of squared distances of all the fiducial points from the principal axis $i$. Later in 2001 [57] an approximate distribution of TRE was derived. It was shown to be distributed as sum of three chi-square variables. It was shown that TRE is anisotropic in nature. The component of TRE along

the direction parallel to the line joining the origin of the principal axes to the target point has a slightly lower value relative to the components along the other two perpendicular directions.

It was also known that the following relation holds good between FRE, FLE, and TRE [56]:

$$\left\langle \mathrm{FRE}^2\left(\mathbf{x}_i\right)\right\rangle = \left\langle \mathrm{FLE}^2\right\rangle - \left\langle \mathrm{TRE}^2\left(\mathbf{x}_i\right)\right\rangle, \tag{5}$$

where $\left\langle \mathrm{FRE}^2\left(\mathbf{x}_i\right)\right\rangle$ is the expected values of individual FRE at $\mathbf{x}_i$.

## 4. Overview of the Dissertation

In this dissertation we will concentrate on an error analysis of fiducial systems employing rigid-body point-based registration. The dissertation consists of three parts. Each part is explained briefly here.

Distribution of FRE of a Fiducial Marker (Chapter II - IV)

For performing the registration it is necessary to find *K* or more corresponding fiducial points in each of two *K*-dimensional spaces (*K* = 3 for practical purposes). Anatomical landmark locations can be chosen to act as fiducial points, but markers attached rigidly to patients are preferred for accurate systems. We will consider from now on that fiducial markers are used for the registration. We know that there is always the potential for error in localizing the fiducials, and that error results in the registration errors—FRE and TRE. TRE statistics has been well analyzed. We know the distribution of TRE at any target **r** [57] and also its magnitude up to first order [56]. From (4) and (5), the magnitude of expected FRE at any marker can be estimated. Sibson [55] derived a distribution for the overall FRE, and gave a relation between the overall FRE and FLE. No study has been done till now though to derive statistical details of the FRE of an individual marker. In Chapter II of this dissertation we derive the approximate distribution for FRE at any individual marker. From this distribution any statistics regarding FRE for individual

markers can be derived. In Chapter III the approximate distribution is verified by means of numerical simulations.

It has been a common practice to remove from the registration process a fiducial marker at position $\mathbf{x}_i$ whose individual error, $\mathrm{FRE}(\mathbf{x}_i)$, is high [58-60]. That marker is ignored, while the remaining markers are used for the registration. This approach is based on the assumption that fiducial marker with high FRE is possibly compromised (moved, bent, etc.), and that removing it will reduce TRE. This approach is reasonable when FRE is extremely high, but "extremely high" has never been quantified. If on the other hand a marker with high FRE has not been compromised, then ignoring that fiducial marker during the registration is unwarranted and will tend to increase TRE. Thus it becomes desirable to find a method for estimating whether a given marker is compromised. Chapter IV suggests a possible approach towards finding compromised fiducial markers using the results of Chapter II.

Validation of a Fiducial Frame System (Chapter V)

Various types of fiducial systems are continually being proposed for use in image-guided surgery. Before they are used to guide surgery, they must be validated, i.e., it must be shown that they can provide the required accuracy and do not cause undesired results. Usually experiments to validate such systems on patients must be done by collecting data during an invasive procedure in order to gain physical access to the point or points in the anatomy at which the system is targeted. It would be very convenient and time saving to collect patient data outside the operating room. The trouble is then to determine whether the fiducial system provides the required accuracy at a specific anatomical location that is reachable only during surgery. We propose a new validation method for validating fiducial frames for image-guided otologic surgery. Using this new validation method, error can be measured at points that are accessible without surgery and, based on that measured error, the error is estimated at points that can be reached only via surgery. In

Chapter V we discuss the theory behind it, explain the experimental procedure, and give results. The accuracy of a point-based fiducial system is also compared to a surface-based system.

Accuracy Evaluation Using Virtual Targets (Chapter VI)

In Chapter VI we present a new concept that employs “virtual targets” for the evaluation of the accuracy of surgical targeting platforms. Targeting platforms are devices that are used to guide surgeons in placing electrodes into the deep-brain area during DBS surgeries. Though previous studies have been performed to measure the accuracy of the system [61], there were difficulties in finding the error contributed by the platform. The method proposed using virtual targets enables us to conduct experiments on skulls and measure the error contributed by just the platform.

In Chapter VII we give conclusions and suggest some directions for future work.

# CHAPTER II

## THE DISTRIBUTION OF FIDUCIAL REGISTRATION ERROR OF A FIDUCIAL MARKER IN RIGID-BODY POINT-BASED REGISTRATION

This chapter presents a derivation of an approximation to the distribution of fiducial registration error (FRE) of a fiducial marker after performing rigid-body point-based registration [62]. In the first section of this chapter we will see some previous work related to the error analysis which forms the basis of our derivation. The notations and part of the derivations in this first section follow the work of Fitzpatrick *et al.* [56, 57]. Then in the second section we proceed with the new set of derivations that is the new theory reported by this dissertation.

### 1. Background

Suppose we have a fiducial system defined by $N$ fiducial markers in a $K$ dimensional space. Let $X$ and $Y$ be $N$-by-$K$ matrices representing the positions of $N$ corresponding fiducial markers in two $K$-dimensional spaces that need to be registered. Thus, each row of $X$ and $Y$ represents the vector positions of two corresponding fiducial points. Sibson found in his work in 1979 [55] that the distribution of registration errors in a system is independent of the gross rigid-body motion, *i.e.*, rotation and translation, and depends only on the configuration of fiducials $X$ in one space, and the localization errors. This fact lets us assume that there is no rigid-body motion between $X$ and $Y$, but that they differ only by the perturbations caused by the fiducial localization error (FLE), which has zero mean. He assumed a normal distribution of errors and also simplified things by setting the localization error in one space to zero. In 1985 [54] Langron and Collins showed that if there are localization errors in both spaces with expected fiducial localization errors in the $X$ and $Y$ spaces equal to $\langle \mathrm{FLE}_X \rangle$ and $\langle \mathrm{FLE}_Y \rangle$ respectively, then if we set the

localization error in $X$ to zero, then the error in the other space, $Y$, should be set to $\left\langle \mathrm{FLE}^2 \right\rangle = \left\langle \mathrm{FLE}_X^2 \right\rangle + \left\langle \mathrm{FLE}_Y^2 \right\rangle$. For the purpose of error analysis we can therefore perturb $X$ using Langron and Collins formula in order to get the perturbed set of fiducial points $Y$. Following Sibson's formalism we have

$$Y = X + \varepsilon F \,, \tag{6}$$

where $\varepsilon$ is a positive dimensionless constant that is small enough to allow us to ignore higher order terms in the derivations that follow, and $F$ is the $N$-by-$K$ perturbation matrix representing the total FLE. The elements of $F$ are independent, identically distributed random variables that are drawn from a zero-mean normal distribution $\mathcal{N}(0,\sigma)$ where

$$\sigma^2 = \left\langle \mathrm{FLE}^2 \right\rangle / K \,. \tag{7}$$

The choice of origin for $X$ is arbitrary as it is just a translation effect in the overall transformation. So Sibson assumes $X$ to be centered at origin. Thus

$$\sum_{a=1}^{N} X_{ak} = 0 \,. \tag{8}$$

The registration problem now becomes finding the rotation matrix, $R$, and translation vector, $\mathbf{t}$, that aligns $X$ and $Y$ optimally by minimizing

$$G \equiv \mathrm{trace}\left( \left( Y - XR - 1_N t^t \right)^t \left( Y - XR - 1_N t^t \right) \right) = \sum_{i=1}^{N} \left| R\mathbf{x_i} + \mathbf{t} - \mathbf{y_i} \right|^2 , \tag{9}$$

which is same as minimizing

$$\mathrm{FRE}^2 \equiv \frac{1}{N} \sum_{i=1}^{N} \left| R\mathbf{x_i} + \mathbf{t} - \mathbf{y_i} \right|^2 , \tag{10}$$

where $\mathbf{x_i}$ and $\mathbf{y_i}$ represent the $i^{\mathrm{th}}$ fiducial in $X$ and $Y$ matrices respectively. $G$ is basically the sum of the individual $\mathrm{FRE}^2$ of all the fiducial markers.

The process of finding the rigid-body transformation begins by finding the translation vector, **t**, which is simply the mean displacement between the centers of the two sets of fiducials [1, 57]. For our set of fiducials,

$$t^t = \frac{\varepsilon 1_N^t F}{N}. \tag{11}$$

It is convenient to define a demeaned version of *F*, which we call $\hat{F}$,

$$\hat{F} = F - \frac{1_N 1_N^t F}{N}. \tag{12}$$

The calculation of *R* begins by finding the demeaned version $\hat{Y}$ of *Y*, where

$$\hat{Y} = Y - \frac{1_N 1_N^t Y^t}{N} = X + \varepsilon \hat{F}. \tag{13}$$

It is not necessary to demean *X* because the origin lies at its mean. Applying (8) and (13) in (10) reduces the problem of finding *R* to the Orthogonal Procrustes problem. Many published methods are available to find *R* [27-38]. The first general solution was given by Schönemann [28] using the singular-value decomposition (SVD) approach, and the later solutions are equivalent to his. The *R* that minimizes $\mathrm{FRE}^2$ is

$$R = BA^t, \tag{14}$$

where $ADB^t$ is the SVD of $\hat{Y}^t \hat{X}$, where $\hat{X}$ is the demeaned version of *X*. *A*, *D*, and *B* are *K*-by-*K* matrices. *A* and *B* are orthogonal, and *D* is diagonal with nonnegative elements along the diagonal. By our assumption that *X* is centered at origin (Eq. (8)), $X = \hat{X}$. Thus,

$$\hat{Y}^t X = ADB^t. \tag{15}$$

Thus the optimal solution for *R* from Eq. (14) yields, $\hat{Y}^t XR = ADA^t$. We also see that $R^t X^t \hat{Y} = ADA^t$. Thus,

$$\hat{Y}^t XR = R^t X^t \hat{Y}. \tag{16}$$

To derive a first-order approximation for *R*, we express it as a power series of $\varepsilon$ as follows:

$$R = R^{(0)} + \varepsilon R^{(1)} + \mathrm{O}\left(\varepsilon^2\right). \tag{17}$$

When $\varepsilon = 0$, $X = Y$. Therefore $R$ is the identity matrix $I$, i.e., $R^{(0)} = I$. Applying this in (17), we see that

$$R = I + \varepsilon R^{(1)} + \mathrm{O}\left(\varepsilon^2\right). \tag{18}$$

We wish to derive an expression for the first-order approximation for $R$, $R^{(1)}$. By analyzing the orthogonal property of $R$, we see that

$$R^t R = I = \left(I + \varepsilon R^{(1)t} + \mathrm{O}\left(\varepsilon^2\right)\right)\left(I + \varepsilon R^{(1)} + \mathrm{O}\left(\varepsilon^2\right)\right) = I + \varepsilon\left(R^{(1)t} + R^{(1)}\right) + \mathrm{O}\left(\varepsilon^2\right). \tag{19}$$

This implies that $R^{(1)t} + R^{(1)} = 0$, meaning that $R^{(1)}$ is antisymmetric, *i.e.*

$$R^{(1)t} = -R^{(1)}. \tag{20}$$

From Eq. (18) if we ignore higher order terms, we see that

$$R^{(1)} = R - I. \tag{21}$$

Applying Eqs. (13), (18), and (20) in (16), and observing the linear terms gives us

$$X^t X R^{(1)} + R^{(1)} X^t X = X^t \hat{F} - \hat{F}^t X. \tag{22}$$

We can solve for $R^{(1)}$ by using the method given by Goodall [63]. We find the SVD for $X$, such that

$$X = U \Lambda V^t, \tag{23}$$

where $U$ and $V$ are orthogonal and $\Lambda$ is diagonal. We assume isotropic perturbations by selecting an identical distribution for all elements of $F$. Thus, we can choose our coordinate system to be along the principal axes of the fiducial points without affecting the system. This makes $V = I$. Thus, we have

$$X = U \Lambda. \tag{24}$$

(Note: The reorientation of the coordinate system and the choice of origin as the center of $X$ simplify the derivation that follows. They can easily be undone at the end.) Using (24) in (22) gives us

$$\Lambda^2 R^{(1)} + R^{(1)}\Lambda^2 = \Lambda U^t \hat{F} - \hat{F}^t U \Lambda \,. \tag{25}$$

Solving for $R^{(1)}$ gives us

$$R_{ij}^{(1)} = \frac{\Lambda_{ii} Q_{ij} - \Lambda_{jj} Q_{ji}}{\Lambda_{ii}^2 + \Lambda_{jj}^2}, \tag{26}$$

where we define $Q$ to be same as Goodall in [63]

$$Q = U^t \hat{F} \,. \tag{27}$$

### 1.1. Two-space FLE Problem

In the beginning of this section we saw that to simplify the error analysis Sibson assumed that the FLE in the $X$ space is zero, and the overall RMS FLE is added to the $Y$ space. Let us see whether there is a change in the expression for $R^{(1)}$ if we do not make that assumption. Let $X$ be the original set of fiducial locations with no localization error. Suppose, in addition $Y$ being perturbed by $F$, that $X$ is perturbed by $E$. Then the perturbed set of fiducials in the $X$ space is

$$X_{\text{pert}} = X + \varepsilon E \,. \tag{28}$$

This time the translation vector $t$ has the form

$$t^t = \frac{\varepsilon 1_N^t \left(F - E\right)}{N} \,. \tag{29}$$

The demeaned version $\hat{Y}$ of $Y$, is still given by Eq. (13). This time we must find the demeaned version $\hat{X}_{\text{pert}}$ of $X_{\text{pert}}$, with the result being

$$\hat{X}_{\text{pert}} = X + \varepsilon \hat{E} \,, \tag{30}$$

where $\hat{E}$ is the demeaned version of $E$ given by

$$\hat{E} = E - \frac{1_N 1_N^t E}{N} \,. \tag{31}$$

Eq. (16) now becomes

$$\hat{Y}^t \hat{X}_{\text{pert}} R = R^t \hat{X}_{\text{pert}}^{\text{t}} \hat{Y} \,. \tag{32}$$

Analyzing the left-hand side of this equation up to first order gives:

$$\begin{aligned}\hat{Y}^t \hat{X}_{\text{pert}} R &= \left(X^t + \varepsilon \hat{F}^t\right)\left(X + \varepsilon \hat{E}\right)\left(I + \varepsilon R^{(1)}\right) \\ &= X^t X + \varepsilon X^t X R^{(1)} + \varepsilon X^t \hat{E} + \varepsilon \hat{F}^t X .\end{aligned} \tag{33}$$

Now looking at the right-hand side of the equation up to first order and using (20):

$$\begin{aligned}R^t \hat{X}^{\text{t}}_{\text{pert}} \hat{Y} &= \left(I + \varepsilon R^{(1)t}\right)\left(X^t + \varepsilon \hat{E}^t\right)\left(X + \varepsilon \hat{F}\right) \\ &= X^t X + \varepsilon X^t \hat{F} + \varepsilon \hat{E}^t X - \varepsilon R^{(1)} X^t X .\end{aligned} \tag{34}$$

Equating (33) and (34) gives us

$$X^t X R^{(1)} + R^{(1)} X^t X = X^t \hat{F} + \hat{E}^t X - X^t \hat{E} - \hat{F}^t X \ . \tag{35}$$

Using (24) we have

$$\Lambda^2 R^{(1)} + R^{(1)} \Lambda^2 = \Lambda U^t \hat{F} + \hat{E}^t U \Lambda - \Lambda U^t \hat{E} - \hat{F}^t U \Lambda . \tag{36}$$

Substituting $P = U^t \hat{E}$ and $Q = U^t \hat{F}$, we have

$$\Lambda^2 R^{(1)} + R^{(1)} \Lambda^2 = \Lambda Q + P^t \Lambda - \Lambda P - Q^t \Lambda . \tag{37}$$

Solving for $R^{(1)}$ gives us

$$R^{(1)}_{ij} = \frac{\Lambda_{ii}\left(Q_{ij} - P_{ij}\right) - \Lambda_{jj}\left(Q_{ji} - P_{ji}\right)}{\Lambda_{ii}^2 + \Lambda_{jj}^2} = \frac{\Lambda_{ii} S_{ij} - \Lambda_{jj} S_{ji}}{\Lambda_{ii}^2 + \Lambda_{jj}^2}, \tag{38}$$

where $S = Q - P$. This expression is similar to (26) which is for the case when the FLE is present in only one space. Thus for the future derivations to find the distribution of individual FRE for a fiducial marker we will consider FLE to be in the *Y* space only.

### 1.2. Some Previously Known Results on FRE

Sibson [55] found that, after performing rigid-body point-based registration, *G*, which is given by (9), is to second order is proportional to $\sigma^2$, and is chi-square distributed with $NK - K\left(K+1\right)/2$ degrees of freedom. Thus, the expected value of *G* is given by

$$\langle G \rangle = \left( NK - \frac{1}{2} K \left( K + 1 \right) \right) \sigma^2 . \tag{39}$$

Considering the three dimensional case ($K$ = 3) and applying (7) in (39) we have

$$\langle G \rangle = \left( N - 2 \right) \left\langle \mathrm{FLE}^2 \right\rangle . \tag{40}$$

Then from (9) and (10) we can see that the expected value of overall $\mathrm{FRE}^2$ is

$$\left\langle \mathrm{FRE}^2 \right\rangle = \left( 1 - 2/N \right) \left\langle \mathrm{FLE}^2 \right\rangle . \tag{41}$$

It must be noted that this is the overall $\mathrm{FRE}^2$ expected when a fiducial system is used.

The formula for finding the magnitude of $\mathrm{FRE}^2$ expected at each individual marker was derived by Fitzpatrick *et al.* in 1998 [56] as part of their analysis on relationship between fiducial misalignment and target registration error (TRE). It was shown that the following relation holds good between FRE, FLE, and TRE:

$$\left\langle \mathrm{FRE}^2 \left( \mathbf{r} \right) \right\rangle = \left\langle \mathrm{FLE}^2 \right\rangle - \left\langle \mathrm{TRE}^2 \left( \mathbf{r} \right) \right\rangle . \tag{42}$$

The approximate expression for $\left\langle \mathrm{TRE}^2 \left( \mathbf{r} \right) \right\rangle$ is given by the following formula [56, 57]

$$\left\langle \mathrm{TRE}^2 \left( \mathbf{r} \right) \right\rangle = \left\langle \mathrm{FLE}^2 \right\rangle \left( \frac{1}{N} + \frac{1}{3} \sum_{i=1}^{3} \frac{d_i^2}{f_i^2} \right), \tag{43}$$

where $d_i^2$ is the squared distance of the point **r** from the principal axis *i*, and $f_i^2$ is the sum of squared distances of all the fiducial points from the principal axis *i*. Substituting (43) in (42), we get

$$\left\langle \mathrm{FRE}^2 \left( \mathbf{r} \right) \right\rangle = \left\langle \mathrm{FLE}^2 \right\rangle \left[ \left( \frac{N-1}{N} \right) - \frac{1}{3} \sum_{i=1}^{3} \frac{d_i^2}{f_i^2} \right]. \tag{44}$$

No previous work has been done though to understand the distribution of $\mathrm{FRE}^2 \left( \mathbf{r} \right)$. We will proceed now to derive an approximation for this distribution.

## 2. Derivation of the FRE Distribution

We begin our derivation of the FRE distribution by analyzing the vector fiducial registration error, $\mathbf{FRE}(\mathbf{r})$, for a fiducial marker **r**. It is given by

$$\mathbf{FRE}(\mathbf{r}) = R\mathbf{r} + \mathbf{t} - (\mathbf{r} + \varepsilon\mathbf{f}_\mathbf{r}) = (R - I)\mathbf{r} + \mathbf{t} - \varepsilon\mathbf{f}_\mathbf{r}, \tag{45}$$

where $\mathbf{f}_\mathbf{r}$ represents the fiducial localization error vector at **r**. Using Eq. (21) as a first-order approximation for $(R - I)$ in Eq. (45), we find that **FRE**(**r**) is to first order given by

$$\mathbf{FRE}(\mathbf{r}) = R^{(1)}\mathbf{r} + \mathbf{t} - \mathbf{f}_\mathbf{r}. \tag{46}$$

As in [57], we define $\boldsymbol{\Omega}$ for a three dimensional space ($K$ = 3) as follows:

$$\boldsymbol{\Omega} = \begin{bmatrix} R^{(1)}_{23} & -R^{(1)}_{13} & R^{(1)}_{12} \end{bmatrix}^t. \tag{47}$$

Using the definition given by Eq. (47) and the fact that $R^{(1)}$ is antisymmetric, stated by Eq. (20), we can rewrite (46) as follows;

$$\mathbf{FRE}(\mathbf{r}) = \boldsymbol{\Omega} \times \mathbf{r} + \mathbf{t} - \mathbf{f}_\mathbf{r}. \tag{48}$$

Let us resolve $\mathbf{FRE}(\mathbf{r})$ into three components— $\mathrm{FRE}_\mathrm{r}$, $\mathrm{FRE}_\mathrm{v}$, and $\mathrm{FRE}_\mathrm{w}$ —along three orthogonal directions, $\hat{\mathbf{r}}$, $\hat{\mathbf{v}}$, and $\hat{\mathbf{w}}$, as shown in Figure 2. In this figure, four of $N$ fiducials are shown—fiducials 1, 2, $i$, and $N$—along with their three principal axes (one other fiducial labeled "…" is shown representing the other $N - 4$ fiducials). In addition, $\hat{\mathbf{r}}$, $\hat{\mathbf{v}}$, and $\hat{\mathbf{w}}$ are shown for fiducial $i$. We choose $\hat{\mathbf{r}}$ to be the unit vector along the radial direction, $\hat{\mathbf{v}}$ to be a unit vector chosen perpendicular to $\hat{\mathbf{r}}$, and $\hat{\mathbf{w}}$ to be a unit vector perpendicular to both $\hat{\mathbf{r}}$ and $\hat{\mathbf{v}}$. These vectors are chosen such that the components of $\mathbf{FRE}(\mathbf{r})$ in these directions are uncorrelated, as described later in this section. If $r$ is the magnitude of the vector **r**, then the three components are given by the following three equations:

$$\mathrm{FRE}_\mathrm{r}(\mathbf{r}) = (\boldsymbol{\Omega} \times \mathbf{r} + \mathbf{t} - \mathbf{f}_\mathrm{r}) \cdot \hat{\mathbf{r}} = \mathbf{t} \cdot \hat{\mathbf{r}} - \mathbf{f}_\mathrm{r} \cdot \hat{\mathbf{r}}, \tag{49}$$

$$\mathrm{FRE}_\mathrm{v}(\mathbf{r}) = (\boldsymbol{\Omega} \times \mathbf{r} + \mathbf{t} - \mathbf{f}_\mathrm{r}) \cdot \hat{\mathbf{v}} = r\boldsymbol{\Omega} \cdot \hat{\mathbf{w}} + \mathbf{t} \cdot \hat{\mathbf{v}} - \mathbf{f}_\mathrm{r} \cdot \hat{\mathbf{v}}, \tag{50}$$

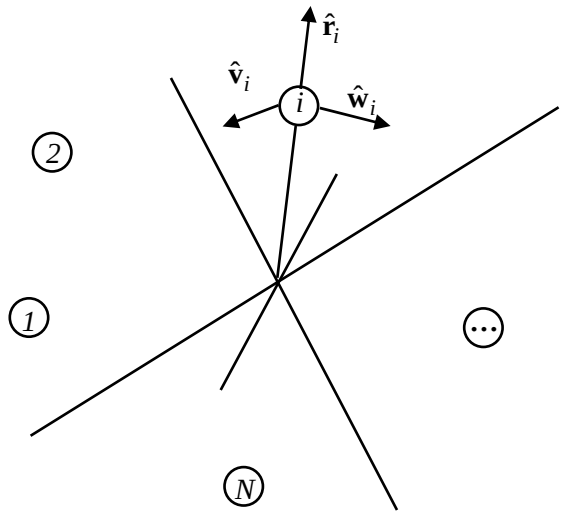


**Figure 2.** Orthogonal directions for $\mathbf{FRE}(\mathbf{r})$. Four fiducials of a configuration of *N* fiducials are shown—fiducials 1, 2, *i*, and *N*—along with their three principal axes (the fiducial labeled "…" is shown representing the other *N* – 4 fiducials). The orthogonal vectors, $\hat{\mathbf{r}}$, $\hat{\mathbf{v}}$, and $\hat{\mathbf{w}}$ are shown for fiducial *i*. $\mathbf{FRE}(\mathbf{r})$ is resolved in to components along these vectors.

$$\mathrm{FRE}_{\mathrm{w}}(\mathbf{r}) = (\boldsymbol{\Omega}\times\mathbf{r} + \mathbf{t} - \mathbf{f}_{\mathrm{r}})\cdot\hat{\mathbf{w}} = -r\boldsymbol{\Omega}\cdot\hat{\mathbf{v}} + \mathbf{t}\cdot\hat{\mathbf{w}} - \mathbf{f}_{\mathrm{r}}\cdot\hat{\mathbf{w}}\,. \tag{51}$$

The individual **FRE** at the fiducial position **r** is given by

$$\mathbf{FRE}(\mathbf{r}) = \mathrm{FRE}_{\mathrm{r}}\hat{\mathbf{r}} + \mathrm{FRE}_{\mathrm{v}}\hat{\mathbf{v}} + \mathrm{FRE}_{\mathrm{w}}\hat{\mathbf{w}}\,. \tag{52}$$

We wish to find a direction for $\hat{\mathbf{v}}$ such that $\hat{\mathbf{v}}$ is perpendicular to $\hat{\mathbf{r}}$, i.e.,

$$\hat{\mathbf{r}}\cdot\hat{\mathbf{v}} = 0\,, \tag{53}$$

and the individual components of **FRE** are uncorrelated, i.e.,

$$\left\langle \mathrm{FRE}_{\mathrm{r}}(\mathbf{r})\,\mathrm{FRE}_{\mathrm{v}}(\mathbf{r})\right\rangle = \left\langle \mathrm{FRE}_{\mathrm{r}}(\mathbf{r})\,\mathrm{FRE}_{\mathrm{w}}(\mathbf{r})\right\rangle = \left\langle \mathrm{FRE}_{\mathrm{v}}(\mathbf{r})\,\mathrm{FRE}_{\mathrm{w}}(\mathbf{r})\right\rangle = 0\,. \tag{54}$$

Eq. (53) and (54) is valid only for certain directions $\hat{\mathbf{v}}$ and hence $\hat{\mathbf{w}}$, which is defined by

$$\hat{\mathbf{w}} = \hat{\mathbf{r}}\times\hat{\mathbf{v}}\,. \tag{55}$$

Fitzpatrick *et al.* [57] derived a solution for $\hat{\mathbf{v}}$ and $\hat{\mathbf{w}}$ that makes the individual **TRE** components uncorrelated. We will show that the same solution holds good for the components of **FRE** too.

We begin by analyzing the cross correlation among the components of translation and rotation.

$$\left\langle t_i t_j \right\rangle = \frac{1}{N^2}\left\langle \left( \sum_{a=1}^{N} F_{ai} \right)\left( \sum_{b=1}^{N} F_{bj} \right) \right\rangle = \frac{1}{N^2}\left\langle \sum_{a=1}^{N}\sum_{b=1}^{N} F_{ai} F_{bj} \right\rangle . \tag{56}$$

Elements of $F$ are independent and are from a zero-mean normal distribution with variance $\sigma^2$. So

$$\left\langle F_{ai} F_{bj} \right\rangle = \delta_{ab}\delta_{ij}\sigma^2 \tag{57}$$

where $\delta$ is the Kronecker delta function defined as $\delta_{ii} = 1$ and $\delta_{ij} = 0$ for $i \neq j$. Applying (57) in (56) gives

$$\left\langle t_i t_j \right\rangle = \frac{\sigma^2}{N}\delta_{ij} . \tag{58}$$

From (26) and (47) the individual elements of $\mathbf{\Omega}$ are defined as follows:

$$\Omega_j = \left( \frac{\Lambda_{kk} Q_{kl} - \Lambda_{ll} Q_{lk}}{\Lambda_{kk}^2 + \Lambda_{ll}^2} \right), \tag{59}$$

where $\{j,k,l\} = \{1,2,3\}$, $\{2,3,1\}$, or $\{3,1,2\}$. Using this definition, we can express the product $\left\langle \Omega_i \Omega_j \right\rangle$ as

$$\left\langle \Omega_i \Omega_j \right\rangle = \left\langle \left( \frac{\Lambda_{aa} Q_{ab} - \Lambda_{bb} Q_{ba}}{\Lambda_{aa}^2 + \Lambda_{bb}^2} \right)\left( \frac{\Lambda_{cc} Q_{cd} - \Lambda_{dd} Q_{dc}}{\Lambda_{cc}^2 + \Lambda_{dd}^2} \right) \right\rangle \tag{60}$$

where $\{i,a,b\}$ and $\{j,c,d\}$ represent the circular sequence of numbers as mentioned before. We will derive an expression for $\left\langle \Lambda_{aa} Q_{ab} \Lambda_{cc} Q_{cd} \right\rangle$ using (27).

$$\left\langle \Lambda_{aa} Q_{ab} \Lambda_{cc} Q_{cd} \right\rangle = \left\langle \sum_{i=1}^{N}\sum_{j=1}^{N} \Lambda_{aa}\Lambda_{cc} U_{ia} U_{jc} \hat{F}_{ib} \hat{F}_{jd} \right\rangle . \tag{61}$$

From (12) we see that

$$\hat{F}_{aj} = F_{aj} - \frac{1}{N}\sum_{b=1}^{N} F_{bj} , \tag{62}$$

from which we get

$$\begin{aligned}\left\langle \hat{F}_{ai}\hat{F}_{bj}\right\rangle &= \left\langle \left(F_{ai}-\frac{1}{N}\sum_{c=1}^{N}F_{ci}\right)\left(F_{bj}-\frac{1}{N}\sum_{d=1}^{N}F_{dj}\right)\right\rangle \\ &= \sigma^2\left(\delta_{ab}\delta_{ij}-\frac{1}{N}\delta_{ij}-\frac{1}{N}\delta_{ij}+\frac{1}{N}\delta_{ij}\right) \\ &= \sigma^2\delta_{ij}\left(\delta_{ab}-\frac{1}{N}\right).\end{aligned} \tag{63}$$

This yields

$$\left\langle \Lambda_{aa}Q_{ab}\Lambda_{cc}Q_{cd}\right\rangle = \sigma^2\delta_{bd}\sum_{i=1}^{N}\sum_{j=1}^{N}\Lambda_{aa}\Lambda_{cc}U_{ia}U_{jc}\left(\delta_{ij}-\frac{1}{N}\right). \tag{64}$$

*U* is an orthogonal matrix. So

$$\sum_{i=1}^{N}U_{ia}U_{ic} = \left(U^tU\right)_{ac} = \delta_{ac}\,. \tag{65}$$

Using (24) and (8) gives us

$$\sum_{i=1}^{N}\sum_{j=1}^{N}\Lambda_{aa}\Lambda_{cc}U_{ia}U_{jc} = \left(\sum_{i=1}^{N}X_{ia}\right)\left(\sum_{j=1}^{N}X_{jc}\right) = 0\,. \tag{66}$$

Applying (65) and (66) in (64) gives us

$$\left\langle \Lambda_{aa}Q_{ab}\Lambda_{cc}Q_{cd}\right\rangle = \sigma^2\delta_{bd}\Lambda_{aa}\Lambda_{cc}\left(U^TU\right)_{ac} = \sigma^2\Lambda_{aa}\Lambda_{cc}\delta_{ac}\delta_{bd}\,. \tag{67}$$

Applying this in (60), we get

$$\begin{aligned}\left\langle \Omega_i\Omega_j\right\rangle &= \left\langle \left(\frac{\Lambda_{aa}Q_{ab}-\Lambda_{bb}Q_{ba}}{\Lambda_{aa}^2+\Lambda_{bb}^2}\right)\left(\frac{\Lambda_{cc}Q_{cd}-\Lambda_{dd}Q_{dc}}{\Lambda_{cc}^2+\Lambda_{dd}^2}\right)\right\rangle \\ &= \sigma^2\left(\frac{\delta_{ac}\delta_{bd}\left(\Lambda_{aa}\Lambda_{cc}+\Lambda_{bb}\Lambda_{dd}\right)-\delta_{bc}\delta_{ad}\left(\Lambda_{bb}\Lambda_{cc}+\Lambda_{aa}\Lambda_{dd}\right)}{\left(\Lambda_{aa}^2+\Lambda_{bb}^2\right)\left(\Lambda_{cc}^2+\Lambda_{dd}^2\right)}\right) \\ &= \frac{\sigma^2\left(\delta_{ac}\delta_{bd}-\delta_{bc}\delta_{ad}\right)}{\Lambda_{aa}^2+\Lambda_{bb}^2}.\end{aligned} \tag{68}$$

This is nonzero only when $a=c$ and $b=d$, or $b=c$ and $a=d$. From the definition of $\Omega_j$ in (59), the first case is possible when $i=j$. The second case is not possible. Thus,

$$\left\langle \Omega_i \Omega_j \right\rangle = \frac{\sigma^2 \delta_{ij}}{\Lambda_{aa}^2 + \Lambda_{bb}^2}. \tag{69}$$

When $i \neq j$, $\left\langle \Omega_i \Omega_j \right\rangle = 0$. We denote $\left\langle \Omega_i^2 \right\rangle$ as $\omega_i^2$ from here on. Thus,

$$\omega_i^2 = \frac{\sigma^2 \delta_{ij}}{\Lambda_{aa}^2 + \Lambda_{bb}^2}. \tag{70}$$

Now analyzing $\left\langle t_i \Omega_j \right\rangle$,

$$\begin{aligned}
\left\langle t_i \Omega_j \right\rangle &= \frac{1}{N} \left\langle \left( \sum_{a=1}^{N} F_{ai} \right) \left( \frac{\Lambda_{kk} Q_{kl} - \Lambda_{ll} Q_{lk}}{\Lambda_{kk}^2 + \Lambda_{ll}^2} \right) \right\rangle \\
&= \frac{1}{N} \left\langle \sum_{a=1}^{N} \sum_{b=1}^{N} \frac{\left( \Lambda_{kk} U_{bk} \left( F_{ai} F_{bl} - \frac{1}{N} \sum_{c=1}^{N} F_{ai} F_{cl} \right) - \Lambda_{ll} U_{bl} \left( F_{ai} F_{bk} - \frac{1}{N} \sum_{c=1}^{N} F_{ai} F_{ck} \right) \right)}{\Lambda_{kk}^2 + \Lambda_{ll}^2} \right\rangle \\
&= \frac{\sigma^2}{N} \left( \sum_{a=1}^{N} \sum_{b=1}^{N} \frac{\left( \Lambda_{kk} U_{bk} \left( \delta_{ab} \delta_{il} - \frac{1}{N} \sum_{c=1}^{N} \delta_{ac} \delta_{il} \right) - \Lambda_{ll} U_{bl} \left( \delta_{ab} \delta_{ik} - \frac{1}{N} \sum_{c=1}^{N} \delta_{ac} \delta_{ik} \right) \right)}{\Lambda_{kk}^2 + \Lambda_{ll}^2} \right).
\end{aligned} \tag{71}$$

We know that

$$\sum_{a=1}^{N} \sum_{b=1}^{N} U_{bk} \left( \delta_{ab} - \frac{1}{N} \sum_{c=1}^{N} \delta_{ac} \right) = \sum_{a=1}^{N} U_{ak} - \frac{1}{N} \sum_{a=1}^{N} \sum_{b=1}^{N} U_{bk} = \sum_{a=1}^{N} U_{ak} - \sum_{b=1}^{N} U_{bk} = 0. \tag{72}$$

This shows that

$$\left\langle t_i \Omega_j \right\rangle = 0. \tag{73}$$

Now looking at $\left\langle F_{ri} \Omega_j \right\rangle$ where $F_{ri}$ is the fiducial localization error for the fiducial **r** under consideration along the axis $i$,

$$\left\langle F_{ri} \Omega_j \right\rangle = \left\langle F_{ri} \left( \frac{\Lambda_{kk} Q_{kl} - \Lambda_{ll} Q_{lk}}{\Lambda_{kk}^2 + \Lambda_{ll}^2} \right) \right\rangle = \left\langle \frac{\left( \sum_{b=1}^{N} \left( \Lambda_{kk} U_{bk} F_{ri} \hat{F}_{bl} - \Lambda_{ll} U_{bl} F_{ri} \hat{F}_{bk} \right) \right)}{\Lambda_{kk}^2 + \Lambda_{ll}^2} \right\rangle. \tag{74}$$

Using the definitions of $F_{ai}$ and $\hat{F}_{bj}$, we see that

$$\left\langle F_{ai}\hat{F}_{bj}\right\rangle = \left\langle F_{ai}\left(F_{bj} - \frac{1}{N}\sum_{c=1}^{N}F_{cj}\right)\right\rangle = \sigma^2\left(\delta_{ab}\delta_{ij} - \frac{1}{N}\sum_{c=1}^{N}\delta_{ac}\delta_{ij}\right) = \sigma^2\delta_{ij}\left(\delta_{ab} - \frac{1}{N}\right). \tag{75}$$

Applying this to (74) gives

$$\begin{aligned}\left\langle F_{ri}\Omega_j\right\rangle &= \sigma^2\left(\frac{\left(\sum_{b=1}^{N}\left(\Lambda_{kk}U_{bk}\delta_{il}\left(\delta_{rb} - \frac{1}{N}\right) - \Lambda_{ll}U_{bl}\delta_{ik}\left(\delta_{rb} - \frac{1}{N}\right)\right)\right)}{\Lambda_{kk}^2 + \Lambda_{ll}^2}\right) \\ &= \sigma^2\left(\frac{\delta_{il}\left(\Lambda_{kk}U_{rk} - \frac{1}{N}\sum_{b=1}^{N}\Lambda_{kk}U_{bk}\right) - \delta_{ik}\left(\Lambda_{ll}U_{rl} - \frac{1}{N}\sum_{b=1}^{N}\Lambda_{ll}U_{bl}\right)}{\Lambda_{kk}^2 + \Lambda_{ll}^2}\right) \\ &= \sigma^2\left(\frac{\delta_{il}\left(r_k - \frac{1}{N}\sum_{b=1}^{N}X_{bk}\right) - \delta_{ik}\left(r_l - \frac{1}{N}\sum_{b=1}^{N}X_{bl}\right)}{\Lambda_{kk}^2 + \Lambda_{ll}^2}\right).\end{aligned} \tag{76}$$

Applying (8),

$$\left\langle F_{ri}\Omega_j\right\rangle = \sigma^2\left(\frac{\delta_{il}r_k - \delta_{ik}r_l}{\Lambda_{kk}^2 + \Lambda_{ll}^2}\right). \tag{77}$$

Looking at $\left\langle F_{ri}t_j\right\rangle$

$$\left\langle F_{ri}t_j\right\rangle = \left\langle F_{ri}\left(\frac{1}{N}\sum_{a=1}^{N}F_{aj}\right)\right\rangle = \frac{\sigma^2}{N}\sum_{a=1}^{N}\delta_{ra}\delta_{ij} = \frac{\sigma^2}{N}\delta_{ij}. \tag{78}$$

Now looking at $\left\langle \mathrm{FRE}_r(\mathbf{r})\mathrm{FRE}_v(\mathbf{r})\right\rangle$

$$\begin{aligned}\left\langle \mathrm{FRE}_r(\mathbf{r})\mathrm{FRE}_v(\mathbf{r})\right\rangle &= \left\langle\left(\mathbf{t}\cdot\hat{\mathbf{r}} - \mathbf{f}_\mathbf{r}\cdot\hat{\mathbf{r}}\right)\left(r\boldsymbol{\Omega}\cdot\hat{\mathbf{w}} + \mathbf{t}\cdot\hat{\mathbf{v}} - \mathbf{f}_\mathbf{r}\cdot\hat{\mathbf{v}}\right)\right\rangle \\ &= r\sum_{i=1}^{K}\sum_{j=1}^{K}\left\langle t_i\Omega_j\right\rangle\hat{r}_i\hat{w}_j + \sum_{i=1}^{K}\sum_{j=1}^{K}\left\langle t_it_j\right\rangle\hat{r}_i\hat{v}_j - \sum_{i=1}^{K}\sum_{j=1}^{K}\left\langle t_iF_{rj}\right\rangle\hat{r}_i\hat{v}_j \\ &\quad -r\sum_{i=1}^{K}\sum_{j=1}^{K}\left\langle F_{ri}\Omega_j\right\rangle\hat{r}_i\hat{w}_j - \sum_{i=1}^{K}\sum_{j=1}^{K}\left\langle F_{ri}t_j\right\rangle\hat{r}_i\hat{v}_j + \sum_{i=1}^{K}\sum_{j=1}^{K}\left\langle F_{ri}F_{rj}\right\rangle\hat{r}_i\hat{v}_j.\end{aligned} \tag{79}$$

Using the results in (57), (58), (73), (77), and (78) yields

$$
\begin{aligned}
\left\langle \mathrm{FRE}_r(\mathbf{r})\mathrm{FRE}_v(\mathbf{r})\right\rangle &= \sum_{i=1}^{K}\sum_{j=1}^{K}\left\langle t_i t_j\right\rangle \hat{r}_i\hat{v}_j - \sum_{i=1}^{K}\sum_{j=1}^{K}\left\langle t_i F_{rj}\right\rangle \hat{r}_i\hat{v}_j \\
&\quad -r\sum_{i=1}^{K}\sum_{j=1}^{K}\left\langle F_{ri}\Omega_j\right\rangle \hat{r}_i\hat{w}_j - \sum_{i=1}^{K}\sum_{j=1}^{K}\left\langle F_{ri}t_j\right\rangle \hat{r}_i\hat{v}_j + \sum_{i=1}^{K}\sum_{j=1}^{K}\left\langle F_{ri}F_{rj}\right\rangle \hat{r}_i\hat{v}_j \\
&= \frac{\sigma^2}{N}\sum_{i=1}^{K}\sum_{j=1}^{K}\delta_{ij}\hat{r}_i\hat{v}_j - \frac{\sigma^2}{N}\sum_{i=1}^{K}\sum_{j=1}^{K}\delta_{ij}\hat{r}_i\hat{v}_j \\
&\quad -r\sigma^2\sum_{i=1}^{K}\sum_{j=1}^{K}\left(\frac{\delta_{il}r_k-\delta_{ik}r_l}{\Lambda_{kk}^2+\Lambda_{ll}^2}\right)\hat{r}_i\hat{w}_j - \frac{\sigma^2}{N}\sum_{i=1}^{K}\sum_{j=1}^{K}\delta_{ij}\hat{r}_i\hat{v}_j + \sigma^2\sum_{i=1}^{K}\sum_{j=1}^{K}\delta_{ij}\hat{r}_i\hat{v}_j \\
&= -r\sigma^2\sum_{i=1}^{K}\sum_{j=1}^{K}\left(\frac{\delta_{il}r_k-\delta_{ik}r_l}{\Lambda_{kk}^2+\Lambda_{ll}^2}\right)\hat{r}_i\hat{w}_j .
\end{aligned}
\tag{80}
$$

For three dimensional situation, i.e., $K=3$,

$$
\begin{aligned}
\sum_{i=1}^{K}\sum_{j=1}^{K}\left(\frac{\delta_{il}r_k-\delta_{ik}r_l}{\Lambda_{kk}^2+\Lambda_{ll}^2}\right)\hat{r}_i\hat{w}_j &= \frac{r_3\hat{r}_1\hat{w}_2}{\Lambda_{33}^2+\Lambda_{11}^2} - \frac{r_2\hat{r}_1\hat{w}_3}{\Lambda_{11}^2+\Lambda_{22}^2} - \frac{r_3\hat{r}_2\hat{w}_1}{\Lambda_{22}^2+\Lambda_{33}^2} \\
&\quad + \frac{r_1\hat{r}_2\hat{w}_3}{\Lambda_{11}^2+\Lambda_{22}^2} + \frac{r_2\hat{r}_3\hat{w}_1}{\Lambda_{22}^2+\Lambda_{33}^2} - \frac{r_1\hat{r}_3\hat{w}_2}{\Lambda_{33}^2+\Lambda_{11}^2} \\
&= r\left(\begin{array}{l}
\dfrac{\hat{r}_3\hat{r}_1\hat{w}_2}{\Lambda_{33}^2+\Lambda_{11}^2} - \dfrac{\hat{r}_2\hat{r}_1\hat{w}_3}{\Lambda_{11}^2+\Lambda_{22}^2} - \dfrac{\hat{r}_3\hat{r}_2\hat{w}_1}{\Lambda_{22}^2+\Lambda_{33}^2} \\
+\dfrac{\hat{r}_1\hat{r}_2\hat{w}_3}{\Lambda_{11}^2+\Lambda_{22}^2} + \dfrac{\hat{r}_2\hat{r}_3\hat{w}_1}{\Lambda_{22}^2+\Lambda_{33}^2} - \dfrac{\hat{r}_1\hat{r}_3\hat{w}_2}{\Lambda_{33}^2+\Lambda_{11}^2}
\end{array}\right) \\
&= 0.
\end{aligned}
\tag{81}
$$

This makes

$$
\left\langle \mathrm{FRE}_r(\mathbf{r})\mathrm{FRE}_v(\mathbf{r})\right\rangle = 0 . \tag{82}
$$

We can similarly prove that

$$
\left\langle \mathrm{FRE}_r(\mathbf{r})\mathrm{FRE}_w(\mathbf{r})\right\rangle = 0 . \tag{83}
$$

Eqs. (82) and (83) are valid for any **v** and **w** that are perpendicular to each other and to **r**. We will begin analyzing $\left\langle \mathrm{FRE}_v(\mathbf{r})\mathrm{FRE}_w(\mathbf{r})\right\rangle$ now. This will impose a constraint on the choice of **v** and **w** for the terms to become zero.

$$\begin{aligned}
&\left\langle \mathrm{FRE}_{\mathrm{v}}(\mathbf{r})\mathrm{FRE}_{\mathrm{w}}(\mathbf{r})\right\rangle = \left\langle \left(r\boldsymbol{\Omega}\cdot\hat{\mathbf{w}}+\mathbf{t}\cdot\hat{\mathbf{v}}-\mathbf{f}_{\mathbf{r}}\cdot\hat{\mathbf{v}}\right)\left(-r\boldsymbol{\Omega}\cdot\hat{\mathbf{v}}+\mathbf{t}\cdot\hat{\mathbf{w}}-\mathbf{f}_{\mathbf{r}}\cdot\hat{\mathbf{w}}\right)\right\rangle \\
&= -r^2\sum_{i=1}^{K}\sum_{j=1}^{K}\left\langle \Omega_i\Omega_j\right\rangle \hat{w}_i\hat{v}_j + r\sum_{i=1}^{K}\sum_{j=1}^{K}\left\langle \Omega_i t_j\right\rangle \hat{w}_i\hat{w}_j - r\sum_{i=1}^{K}\sum_{j=1}^{K}\left\langle \Omega_i F_{rj}\right\rangle \hat{w}_i\hat{w}_j - r\sum_{i=1}^{K}\sum_{j=1}^{K}\left\langle t_i\Omega_j\right\rangle \hat{v}_i\hat{v}_j \\
&+\sum_{i=1}^{K}\sum_{j=1}^{K}\left\langle t_i t_j\right\rangle \hat{v}_i\hat{w}_j - \sum_{i=1}^{K}\sum_{j=1}^{K}\left\langle t_i F_{rj}\right\rangle \hat{v}_i\hat{w}_j + r\sum_{i=1}^{K}\sum_{j=1}^{K}\left\langle F_{ri}\Omega_j\right\rangle \hat{v}_i\hat{v}_j - \sum_{i=1}^{K}\sum_{j=1}^{K}\left\langle F_{ri}t_j\right\rangle \hat{v}_i\hat{w}_j + \sum_{i=1}^{K}\sum_{j=1}^{K}\left\langle F_{ri}F_{rj}\right\rangle \hat{v}_i\hat{w}_j.
\end{aligned} \tag{84}$$

Using the results in (57), (58), (69), (73), (77), and (78), we see that

$$\begin{aligned}
\left\langle \mathrm{FRE}_{\mathrm{v}}(\mathbf{r})\mathrm{FRE}_{\mathrm{w}}(\mathbf{r})\right\rangle &= \sigma^2\sum_{i=1}^{K}\sum_{j=1}^{K}\frac{\delta_{ij}\hat{w}_i\hat{v}_j}{\Lambda_{aa}^2+\Lambda_{bb}^2} - r\sigma^2\sum_{i=1}^{K}\sum_{j=1}^{K}\left(\frac{\delta_{il}r_k-\delta_{ik}r_l}{\Lambda_{kk}^2+\Lambda_{ll}^2}\right)\hat{w}_i\hat{w}_j + \frac{\sigma^2}{N}\sum_{i=1}^{K}\sum_{j=1}^{K}\delta_{ij}\hat{v}_i\hat{w}_j \\
&-\frac{\sigma^2}{N}\sum_{i=1}^{K}\sum_{j=1}^{K}\delta_{ij}\hat{v}_i\hat{w}_j + r\sigma^2\sum_{i=1}^{K}\sum_{j=1}^{K}\left(\frac{\delta_{il}r_k-\delta_{ik}r_l}{\Lambda_{kk}^2+\Lambda_{ll}^2}\right)\hat{v}_i\hat{v}_j - \frac{\sigma^2}{N}\sum_{i=1}^{K}\sum_{j=1}^{K}\delta_{ij}\hat{v}_i\hat{w}_j + \sigma^2\sum_{i=1}^{K}\sum_{j=1}^{K}\delta_{ij}\hat{v}_i\hat{w}_j \\
&= \sigma^2\sum_{i=1}^{K}\sum_{j=1}^{K}\frac{\delta_{ij}\hat{w}_i\hat{v}_j}{\Lambda_{aa}^2+\Lambda_{bb}^2} - r\sigma^2\sum_{i=1}^{K}\sum_{j=1}^{K}\left(\frac{\delta_{il}r_k-\delta_{ik}r_l}{\Lambda_{kk}^2+\Lambda_{ll}^2}\right)\hat{w}_i\hat{w}_j + r\sigma^2\sum_{i=1}^{K}\sum_{j=1}^{K}\left(\frac{\delta_{il}r_k-\delta_{ik}r_l}{\Lambda_{kk}^2+\Lambda_{ll}^2}\right)\hat{v}_i\hat{v}_j.
\end{aligned} \tag{85}$$

Again considering the three dimensional case, we will expand each of the three terms on the right-hand side of the above equation as follows:

$$\sum_{i=1}^{K}\sum_{j=1}^{K}\frac{\delta_{ij}\hat{w}_i\hat{v}_j}{\Lambda_{aa}^2+\Lambda_{bb}^2} = \sigma^2\left(\frac{\hat{w}_1\hat{v}_1}{\Lambda_{22}^2+\Lambda_{33}^2}+\frac{\hat{w}_2\hat{v}_2}{\Lambda_{33}^2+\Lambda_{11}^2}+\frac{\hat{w}_3\hat{v}_3}{\Lambda_{11}^2+\Lambda_{22}^2}\right). \tag{86}$$

$$\begin{aligned}
\sum_{i=1}^{K}\sum_{j=1}^{K}\left(\frac{\delta_{il}r_k-\delta_{ik}r_l}{\Lambda_{kk}^2+\Lambda_{ll}^2}\right)\hat{w}_i\hat{w}_j &= r\left(\begin{array}{l}\dfrac{\hat{r}_3\hat{w}_1\hat{w}_2}{\Lambda_{33}^2+\Lambda_{11}^2}-\dfrac{\hat{r}_2\hat{w}_1\hat{w}_3}{\Lambda_{11}^2+\Lambda_{22}^2}-\dfrac{\hat{r}_3\hat{w}_2\hat{w}_1}{\Lambda_{22}^2+\Lambda_{33}^2} \\ +\dfrac{\hat{r}_1\hat{w}_2\hat{w}_3}{\Lambda_{11}^2+\Lambda_{22}^2}+\dfrac{\hat{r}_2\hat{w}_3\hat{w}_1}{\Lambda_{22}^2+\Lambda_{33}^2}-\dfrac{\hat{r}_1\hat{w}_3\hat{w}_2}{\Lambda_{33}^2+\Lambda_{11}^2}\end{array}\right) \\
&= r\left(\frac{\hat{w}_2\left(\hat{r}_3\hat{w}_1-\hat{r}_1\hat{w}_3\right)}{\lambda_{33}^2+\lambda_{11}^2}+\frac{\hat{w}_3\left(\hat{r}_1\hat{w}_2-\hat{r}_2\hat{w}_1\right)}{\lambda_{11}^2+\lambda_{22}^2}+\frac{\hat{w}_1\left(\hat{r}_2\hat{w}_3-\hat{r}_3\hat{w}_2\right)}{\lambda_{22}^2+\lambda_{33}^2}\right) \\
&= -r\left(\frac{\hat{v}_2\hat{w}_2}{\Lambda_{33}^2+\Lambda_{11}^2}+\frac{\hat{v}_3\hat{w}_3}{\Lambda_{11}^2+\Lambda_{22}^2}+\frac{\hat{v}_1\hat{w}_1}{\Lambda_{22}^2+\Lambda_{33}^2}\right).
\end{aligned} \tag{87}$$

$$\begin{aligned}
\sum_{i=1}^{K}\sum_{j=1}^{K}\left(\frac{\delta_{il}r_k-\delta_{ik}r_l}{\Lambda_{kk}^2+\Lambda_{ll}^2}\right)\hat{v}_i\hat{v}_j &= r\left(\begin{array}{l}\dfrac{\hat{r}_3\hat{v}_1\hat{v}_2}{\Lambda_{33}^2+\Lambda_{11}^2}-\dfrac{\hat{r}_2\hat{v}_1\hat{v}_3}{\Lambda_{11}^2+\Lambda_{22}^2}-\dfrac{\hat{r}_3\hat{v}_2\hat{v}_1}{\Lambda_{22}^2+\Lambda_{33}^2} \\ +\dfrac{\hat{r}_1\hat{v}_2\hat{v}_3}{\Lambda_{11}^2+\Lambda_{22}^2}+\dfrac{\hat{r}_2\hat{v}_3\hat{v}_1}{\Lambda_{22}^2+\Lambda_{33}^2}-\dfrac{\hat{r}_1\hat{v}_3\hat{v}_2}{\Lambda_{33}^2+\Lambda_{11}^2}\end{array}\right) \\
&= r\left[\frac{\hat{v}_2\left(\hat{r}_3\hat{v}_1-\hat{r}_1\hat{v}_3\right)}{\Lambda_{33}^2+\Lambda_{11}^2}+\frac{\hat{v}_3\left(\hat{r}_1\hat{v}_2-\hat{r}_2\hat{v}_1\right)}{\Lambda_{11}^2+\Lambda_{22}^2}+\frac{\hat{v}_1\left(\hat{r}_2\hat{v}_3-\hat{r}_3\hat{v}_2\right)}{\Lambda_{22}^2+\Lambda_{33}^2}\right] \\
&= r\left[\frac{\hat{v}_2\hat{w}_2}{\Lambda_{33}^2+\Lambda_{11}^2}+\frac{\hat{v}_3\hat{w}_3}{\Lambda_{11}^2+\Lambda_{22}^2}+\frac{\hat{v}_1\hat{w}_1}{\Lambda_{22}^2+\Lambda_{33}^2}\right].
\end{aligned} \tag{88}$$

Applying (86), (87), and (88) in (85) gives us,

$$\left\langle \mathrm{FRE}_{\mathbf{v}}(\mathbf{r})\,\mathrm{FRE}_{\mathbf{w}}(\mathbf{r})\right\rangle = r^2\sigma^2\left(\frac{\hat{w}_1\hat{v}_1}{\Lambda_{22}^2+\Lambda_{33}^2}+\frac{\hat{w}_2\hat{v}_2}{\Lambda_{33}^2+\Lambda_{11}^2}+\frac{\hat{w}_3\hat{v}_3}{\Lambda_{11}^2+\Lambda_{22}^2}\right). \tag{89}$$

This term becomes zero for a certain $\hat{\mathbf{v}}$ and $\hat{\mathbf{w}}$. Fitzpatrick *et al.* [57] found a solution for $\hat{\mathbf{v}}$ and $\hat{\mathbf{w}}$ that makes this term zero in order to make $\left\langle \mathrm{TRE}_{\mathbf{v}}\mathrm{TRE}_{\mathbf{w}}\right\rangle$ equal zero.

With the help of Eq. (70) equation (89) can be rewritten as

$$\left\langle \mathrm{FRE}_{\mathbf{v}}(\mathbf{r})\,\mathrm{FRE}_{\mathbf{w}}(\mathbf{r})\right\rangle = r^2\left(\omega_1^2\hat{w}_1\hat{v}_1+\omega_2^2\hat{w}_2\hat{v}_2+\omega_3^2\hat{w}_3\hat{v}_3\right). \tag{90}$$

We are trying to find **v** and **w** that makes this equal zero, i.e.,

$$r^2\left(\omega_1^2\hat{w}_1\hat{v}_1+\omega_2^2\hat{w}_2\hat{v}_2+\omega_3^2\hat{w}_3\hat{v}_3\right)=0\,. \tag{91}$$

From (55), we see that this is same as

$$r_3v_1v_2\left(\omega_2^2-\omega_1^2\right)+r_2v_3v_1\left(\omega_1^2-\omega_3^2\right)+r_1v_2v_3\left(\omega_3^2-\omega_2^2\right)=0\,. \tag{92}$$

This is same as the expression that Fitzpatrick *et al.* [57] solved. If we assume that $\{i,j,k\}=\{1,2,3\}$, $\{2,3,1\}$, or $\{3,1,2\}$, then the solution is defined as follows:

Case 1: At least one of the components of **r** is zero. Suppose $r_i=0$, then there are two possible solutions, namely:

(a) Set $v_i=0$, choose any solution for $v_j$ and $v_k$ that satisfies $\mathbf{r}\cdot\mathbf{v}=0$, and then normalize the vector **v**.

(b) Set $v_i=1$ and $v_j=v_k=0$.

We can choose one of these two solutions for $\hat{\mathbf{v}}$ and the other for $\hat{\mathbf{w}}$.

Case 2: If $\omega_i^2=\omega_j^2$, then there are two simple solutions as follows:

1. Set $v_k=0$, choose any solution for $v_i$ and $v_j$ that satisfies the fact that $\mathbf{r}\cdot\mathbf{v}=0$, and then normalize the **v** vector
2. Set $v_k=1$ and $v_i=v_j=0$.

Like for case 1 we can choose one of these solutions for $\hat{\mathbf{v}}$ and the other for $\hat{\mathbf{w}}$.

Case 3: This is the general case when none of the components of $\mathbf{r}$ is zero and all the $\omega_i^2$ are distinct. We assume $v_k = 1$ for both the possible solutions. The two possible solutions for $v_i$ are the two solutions to the following quadratic equation:

$$r_i r_k \left(\omega_i^2 - \omega_j^2\right) v_i^2 + \left[\left(r_j^2 + r_k^2\right)\left(\omega_i^2 - \omega_j^2\right) + \left(r_i^2 + r_j^2\right)\left(\omega_j^2 - \omega_k^2\right)\right] v_i + r_i r_k \left(\omega_j^2 - \omega_k^2\right) = 0 \qquad (93)$$

The two solutions for $v_j$ are obtained by substituting each possible value of $v_i$ and $v_k$ in $\mathbf{r} \cdot \mathbf{v} = 0$ and solving for $v_j$. One of the two solutions is then chosen for obtaining $\hat{\mathbf{v}}$ and the other for $\hat{\mathbf{w}}$.

### 2.1. Expected Values

The expected value of the square of the magnitude of **FRE** at **r**, $\left\langle \mathrm{FRE}^2(\mathbf{r}) \right\rangle$ is given by

$$\left\langle \mathrm{FRE}^2(\mathbf{r}) \right\rangle = \left\langle \mathrm{FRE}_r^2(\mathbf{r}) + \mathrm{FRE}_v^2(\mathbf{r}) + \mathrm{FRE}_w^2(\mathbf{r}) \right\rangle. \qquad (94)$$

Since we are ignoring higher order terms, each component of **FRE** is a linear combination of elements of $F$, which are normally distributed with zero mean. This implies that the components of **FRE** also have zero mean. So the respective variances of its components—$\sigma_r^2$, $\sigma_v^2$, and $\sigma_w^2$—are same as their mean squared values. We can find these values from (49), (50), and (51) as follows:

$$\begin{aligned}
\sigma_r^2 &= \left\langle \mathrm{FRE}_r^2 \right\rangle = \left\langle \left(\mathbf{t} \cdot \hat{\mathbf{r}} - \mathbf{f}_\mathrm{r} \cdot \hat{\mathbf{r}}\right)^2 \right\rangle \\
&= \sum_{i=1}^{3}\sum_{j=1}^{3} \left\langle t_i t_j \right\rangle \hat{r}_i \hat{r}_j + \sum_{i=1}^{3}\sum_{j=1}^{3} \left\langle F_{ri} F_{rj} \right\rangle \hat{r}_i \hat{r}_j - 2\sum_{i=1}^{3}\sum_{j=1}^{3} \left\langle t_i F_{rj} \right\rangle \hat{r}_i \hat{r}_j \\
&= \frac{\sigma^2}{N} \sum_{i=1}^{3}\sum_{j=1}^{3} \delta_{ij} \hat{r}_i \hat{r}_j + \sigma^2 \sum_{i=1}^{3}\sum_{j=1}^{3} \delta_{ij} \hat{r}_i \hat{r}_j - 2\frac{\sigma^2}{N} \sum_{i=1}^{3}\sum_{j=1}^{3} \delta_{ij} \hat{r}_i \hat{r}_j = \sigma^2 \left(\frac{N-1}{N}\right).
\end{aligned} \qquad (95)$$

Suppose we define

$$\omega_r^2 = \sum_{i=1}^{K} \omega_i^2 \hat{r}_i^2, \ \omega_v^2 = \sum_{i=1}^{K} \omega_i^2 \hat{v}_i^2, \text{ and } \omega_w^2 = \sum_{i=1}^{K} \omega_i^2 \hat{w}_i^2. \qquad (96)$$

Then

$$
\begin{aligned}
\sigma_v^2 &= \left\langle \mathrm{FRE}_v^2 \right\rangle = \left\langle \left( r\boldsymbol{\Omega}\cdot\hat{\mathbf{w}} + \mathbf{t}\cdot\hat{\mathbf{v}} - \mathbf{f}_\mathbf{r}\cdot\hat{\mathbf{v}} \right)^2 \right\rangle \\
&= r^2 \sum_{i=1}^{3}\sum_{j=1}^{3} \left\langle \Omega_i \Omega_j \right\rangle \hat{w}_i \hat{w}_j + \sum_{i=1}^{3}\sum_{j=1}^{3} \left\langle t_i t_j \right\rangle \hat{v}_i \hat{v}_j + \sum_{i=1}^{3}\sum_{j=1}^{3} \left\langle F_{ri} F_{rj} \right\rangle \hat{v}_i \hat{v}_j \\
&\quad + 2r \sum_{i=1}^{3}\sum_{j=1}^{3} \left\langle t_i \Omega_j \right\rangle \hat{v}_i \hat{w}_j - 2\sum_{i=1}^{3}\sum_{j=1}^{3} \left\langle t_i F_{rj} \right\rangle \hat{v}_i \hat{v}_j - 2r \sum_{i=1}^{3}\sum_{j=1}^{3} \left\langle F_{ri} \Omega_j \right\rangle \hat{v}_i \hat{w}_j \\
&= r^2\sigma^2 \sum_{i=1}^{3}\sum_{j=1}^{3} \frac{\delta_{ij}\hat{w}_i \hat{w}_j}{\Lambda_{aa}^2 + \Lambda_{bb}^2} + \frac{\sigma^2}{N} \sum_{i=1}^{3}\sum_{j=1}^{3} \delta_{ij}\hat{v}_i \hat{v}_j + \sigma^2 \sum_{i=1}^{3}\sum_{j=1}^{3} \delta_{ij}\hat{v}_i \hat{v}_j \\
&\quad - \frac{2\sigma^2}{N} \sum_{i=1}^{3}\sum_{j=1}^{3} \delta_{ij}\hat{v}_i \hat{v}_j - 2\sigma^2 r \sum_{i=1}^{3}\sum_{j=1}^{3} \left( \frac{\delta_{il} r_k - \delta_{ik} r_l}{\Lambda_{kk}^2 + \Lambda_{ll}^2} \right) \hat{v}_i \hat{w}_j \\
&= r^2 \omega_w^2 + \sigma^2 \left( \frac{N-1}{N} \right) - 2\sigma^2 r^2 \left( \frac{\hat{w}_2\left(\hat{r}_3\hat{v}_1 - \hat{r}_1\hat{v}_3\right)}{\Lambda_{33}^2 + \Lambda_{11}^2} + \frac{\hat{w}_3\left(\hat{r}_1\hat{v}_2 - \hat{r}_2\hat{v}_1\right)}{\Lambda_{11}^2 + \Lambda_{22}^2} + \frac{\hat{w}_1\left(\hat{r}_2\hat{v}_3 - \hat{r}_3\hat{v}_2\right)}{\Lambda_{22}^2 + \Lambda_{33}^2} \right) \\
&= \sigma^2 \left( \frac{N-1}{N} \right) - r^2 \omega_w^2 .
\end{aligned}
\tag{97}
$$

And

$$
\begin{aligned}
\sigma_w^2 &= \left\langle \mathrm{FRE}_w^2 \right\rangle = \left\langle \left( -r\boldsymbol{\Omega}\cdot\hat{\mathbf{v}} + \mathbf{t}\cdot\hat{\mathbf{w}} - \mathbf{f}_\mathbf{r}\cdot\hat{\mathbf{w}} \right)^2 \right\rangle \\
&= r^2 \sum_{i=1}^{3}\sum_{j=1}^{3} \left\langle \Omega_i \Omega_j \right\rangle \hat{v}_i \hat{v}_j + \sum_{i=1}^{3}\sum_{j=1}^{3} \left\langle t_i t_j \right\rangle \hat{w}_i \hat{w}_j + \sum_{i=1}^{3}\sum_{j=1}^{3} \left\langle F_{ri} F_{rj} \right\rangle \hat{w}_i \hat{w}_j \\
&\quad - 2r \sum_{i=1}^{3}\sum_{j=1}^{3} \left\langle t_i \Omega_j \right\rangle \hat{w}_i \hat{v}_j - 2\sum_{i=1}^{3}\sum_{j=1}^{3} \left\langle t_i F_{rj} \right\rangle \hat{w}_i \hat{w}_j + 2r \sum_{i=1}^{3}\sum_{j=1}^{3} \left\langle F_{ri} \Omega_j \right\rangle \hat{w}_i \hat{v}_j \\
&= \sigma^2 r^2 \sum_{i=1}^{3}\sum_{j=1}^{3} \frac{\delta_{ij}\hat{v}_i \hat{v}_j}{\Lambda_{aa}^2 + \Lambda_{bb}^2} + \frac{\sigma^2}{N} \sum_{i=1}^{3}\sum_{j=1}^{3} \delta_{ij}\hat{w}_i \hat{w}_j + \sigma^2 \sum_{i=1}^{3}\sum_{j=1}^{3} \delta_{ij}\hat{w}_i \hat{w}_j \\
&\quad - \frac{2\sigma^2}{N} \sum_{i=1}^{3}\sum_{j=1}^{3} \delta_{ij}\hat{w}_i \hat{w}_j + 2r\sigma^2 \sum_{i=1}^{3}\sum_{j=1}^{3} \left( \frac{\delta_{il} r_k - \delta_{ik} r_l}{\Lambda_{kk}^2 + \Lambda_{ll}^2} \right) \hat{w}_i \hat{v}_j \\
&= r^2 \omega_v^2 + \sigma^2 \left( \frac{N-1}{N} \right) + 2\sigma^2 r^2 \left( \frac{\hat{v}_2\left(\hat{r}_3\hat{w}_1 - \hat{r}_1\hat{w}_3\right)}{\Lambda_{33}^2 + \Lambda_{11}^2} + \frac{\hat{v}_3\left(\hat{r}_1\hat{w}_2 - \hat{r}_2\hat{w}_1\right)}{\Lambda_{11}^2 + \Lambda_{22}^2} + \frac{\hat{v}_1\left(\hat{r}_2\hat{w}_3 - \hat{r}_3\hat{w}_2\right)}{\Lambda_{22}^2 + \Lambda_{33}^2} \right) \\
&= \sigma^2 \left( \frac{N-1}{N} \right) - r^2 \omega_v^2 .
\end{aligned}
\tag{98}
$$

Now from these variances we can compute $\left\langle \mathrm{FRE}^2(\mathbf{r}) \right\rangle$ to be

$$\begin{aligned}\left\langle \mathrm{FRE}^2(\mathbf{r})\right\rangle &= \sigma_r^2+\sigma_v^2+\sigma_w^2 \\ &= \sigma^2\left(\frac{N-1}{N}\right)+\sigma^2\left(\frac{N-1}{N}\right)-r^2\omega_w^2+\sigma^2\left(\frac{N-1}{N}\right)-r^2\omega_v^2 \\ &= 3\sigma^2\left(\frac{N-1}{N}\right)-r^2\left(\omega_v^2+\omega_w^2\right).\end{aligned} \tag{99}$$

Since $\hat{\mathbf{r}}$, $\hat{\mathbf{v}}$, and $\hat{\mathbf{w}}$ are orthogonal set of axes, we can see from (96) that

$$\omega_r^2+\omega_v^2+\omega_w^2=\omega_1^2+\omega_2^2+\omega_3^2\,. \tag{100}$$

This implies

$$\begin{aligned}\omega_v^2+\omega_w^2 &= \omega_1^2+\omega_2^2+\omega_3^2-\frac{r_1^2\omega_1^2+r_2^2\omega_2^2+r_3^2\omega_3^2}{r_1^2+r_2^2+r_3^2} \\ &= \frac{\omega_1^2\left(r_2^2+r_3^2\right)+\omega_2^2\left(r_1^2+r_3^2\right)+\omega_3^2\left(r_1^2+r_2^2\right)}{r^2}.\end{aligned} \tag{101}$$

Using this result in (99) yields,

$$\left\langle \mathrm{FRE}^2(\mathbf{r})\right\rangle = 3\sigma^2\left(\frac{N-1}{N}\right)-\left(\omega_1^2\left(r_2^2+r_3^2\right)+\omega_2^2\left(r_1^2+r_3^2\right)+\omega_3^2\left(r_1^2+r_2^2\right)\right). \tag{102}$$

If we express the distance of **r** from axis *i* as $d_i$, then $d_i=r_j^2+r_k^2$ for $\{i,j,k\}=\{1,2,3\}$, $\{2,3,1\}$, or $\{3,1,2\}$. Then we can express $\left\langle \mathrm{FRE}^2(\mathbf{r})\right\rangle$ as

$$\left\langle \mathrm{FRE}^2(\mathbf{r})\right\rangle = 3\sigma^2\left(\frac{N-1}{N}\right)-\sum_{i=1}^{3}d_i^2\omega_i^2\,. \tag{103}$$

$\Lambda_{jj}^2+\Lambda_{kk}^2$ is the sum of squared distance of the fiducial points from axis *i*. Using the definition of $\omega_i^2$ from (70), we can rewrite the above expression for $\left\langle \mathrm{FRE}^2(\mathbf{r})\right\rangle$ as follows:

$$\left\langle \mathrm{FRE}^2(\mathbf{r})\right\rangle = \sigma^2\left(3\left(\frac{N-1}{N}\right)-\sum_{i=1}^{3}\frac{d_i^2}{f_i^2}\right). \tag{104}$$

Substituting $\left\langle \mathrm{FLE}^2\right\rangle=3\sigma^2$, we get the same expression given by (44) that is the result found by Fitzpatrick *et al*. [56]. Thus, the variances we derived here agree with the previous results.

## 2.2. Expected Values in any Arbitrary Direction

We will now derive the expected square value of the component of **FRE** in any arbitrary direction $\hat{\mathbf{a}}$. From (52) we can say that the component of **FRE** in any direction $\hat{\mathbf{a}}$ is

$$\mathrm{FRE}_a(\mathbf{r}) = \mathrm{FRE}_r \hat{a}_r + \mathrm{FRE}_v \hat{a}_v + \mathrm{FRE}_w \hat{a}_w , \tag{105}$$

where $\hat{a}_r = \hat{\mathbf{a}} \cdot \hat{\mathbf{r}}$, $\hat{a}_v = \hat{\mathbf{a}} \cdot \hat{\mathbf{v}}$, and $\hat{a}_w = \hat{\mathbf{a}} \cdot \hat{\mathbf{w}}$. This also implies that

$$\left\langle \mathrm{FRE}_a^2(\mathbf{r}) \right\rangle = \left\langle \mathrm{FRE}_r^2 \right\rangle \hat{a}_r^2 + \left\langle \mathrm{FRE}_v^2 \right\rangle \hat{a}_v^2 + \left\langle \mathrm{FRE}_w^2 \right\rangle \hat{a}_w^2 . \tag{106}$$

Since $\mathrm{FRE}_r$, $\mathrm{FRE}_v$, and $\mathrm{FRE}_w$ are uncorrelated, the individual components of $\mathrm{FRE}_a(\mathbf{r})$ are also uncorrelated. Thus (106) is valid. From (95), (97), and (98), we expand (106) as follows:

$$\begin{aligned} \left\langle \mathrm{FRE}_a^2(\mathbf{r}) \right\rangle &= \sigma^2 \left( \frac{N-1}{N} \right) \hat{a}_r^2 + \left( \sigma^2 \left( \frac{N-1}{N} \right) - r^2 \omega_w^2 \right) \hat{a}_v^2 + \left( \sigma^2 \left( \frac{N-1}{N} \right) - r^2 \omega_v^2 \right) \hat{a}_w^2 \\ &= \sigma^2 \left( \frac{N-1}{N} \right) - r^2 \left( \hat{a}_v^2 \omega_w^2 + \hat{a}_w^2 \omega_v^2 \right). \end{aligned} \tag{107}$$

## 2.3. Distribution

We saw till now how to decompose the vector $\mathbf{FRE}(\mathbf{r})$ into three orthogonal components, namely $\mathrm{FRE_r}$, $\mathrm{FRE_v}$, and $\mathrm{FRE_w}$ along the $\hat{\mathbf{r}}$, $\hat{\mathbf{v}}$, and $\hat{\mathbf{w}}$ directions respectively. The three components are shown to be uncorrelated with each other. They are hence independent [64]. All the three components are linear combinations of *F*, which is a set of random variables drawn from the normal distribution $\mathcal{N}(0,\sigma)$. Thus the three components of $\mathbf{FRE}(\mathbf{r})$ along the $\hat{\mathbf{r}}$, $\hat{\mathbf{v}}$, and $\hat{\mathbf{w}}$ directions are also independent, normally distributed variables with zero mean and variances $\sigma_r^2$, $\sigma_v^2$, and $\sigma_w^2$ respectively. Then $\mathrm{FRE}^2(\mathbf{r})$ is distributed as the sum of three chi-square variables

$$\mathrm{FRE}^2(\mathbf{r}) \sim \sigma_r^2 \chi_1^2 + \sigma_v^2 \chi_1^2 + \sigma_w^2 \chi_1^2 . \tag{108}$$

Along an arbitrary direction $\hat{\mathbf{a}}$, $\mathrm{FRE}_a(\mathbf{r})$ is the sum of three independent, zero mean, normal variables as given by (105). Therefore we can say that $\mathrm{FRE}_a(\mathbf{r})$ is also a zero mean, normal variable with variance $\sigma_a^2$ that equals $\left\langle \mathrm{FRE}_a^2(\mathbf{r}) \right\rangle$ given by (107). Thus

$$\mathrm{FRE}_a(\mathbf{r}) \sim \mathcal{N}(0, \sigma_a). \tag{109}$$

## 3. Discussion

In this chapter we have derived a first order approximation for the distribution of the fiducial registration error (FRE) of any fiducial marker **r**. We have shown that FRE can be resolved into three orthogonal components along the directions $\hat{\mathbf{r}}$, $\hat{\mathbf{v}}$, and $\hat{\mathbf{w}}$ such that the three components are independent, zero-mean normal distributions with variances $\sigma_r^2$, $\sigma_v^2$, and $\sigma_w^2$ given by (95), (97), and (98) respectively. We see that the variance along the radial direction $\hat{\mathbf{r}}$ is larger than those in the two perpendicular directions. This difference is similar to that for the variances of the three components of TRE observed by Fitzpatrick *et al*. in 2001 [57], except that in the case of TRE the variance along $\hat{\mathbf{r}}$ is smaller than the variances in the two perpendicular directions. The $\mathrm{FRE}^2$ at any fiducial marker is shown to be distributed as the sum of three chi-square variables with variances $\sigma_r^2$, $\sigma_v^2$, and $\sigma_w^2$ as shown in Eq. (108). We also derived the distribution of FRE along any arbitrary direction. It is shown to be a normal distribution with zero mean and variance given by Eq. (107).

In the next chapter numerical simulations are presented that show that the results we derived here are valid.

# CHAPTER III

## SIMULATIONS

In this chapter we will verify by means of simulations the correctness of the results derived in Chapter II of this dissertation. It was shown in Chapter II that the distribution of $\mathrm{FRE}^2$ for a fiducial marker **r** is the sum of three chi-square variables

$$\mathrm{FRE}^2(\mathbf{r}) \sim \sigma_r^2 \chi_1^2 + \sigma_v^2 \chi_1^2 + \sigma_w^2 \chi_1^2, \tag{110}$$

where $\sigma_r^2$, $\sigma_v^2$, and $\sigma_w^2$ are the variances of FRE along the three orthogonal directions $\hat{\mathbf{r}}$, $\hat{\mathbf{v}}$, and $\hat{\mathbf{w}}$ respectively. In the first section of this chapter we will verify the correctness of this predicted distribution. Then in the second section we will verify the method proposed in Chapter II to compute the variance of FRE along any arbitrary direction, $\hat{\mathbf{a}}$. The simulations performed here are similar to those performed by Fitzpatrick *et al.* in [56] and [57].

Later in this chapter we will also perform simulations to verify the formula for finding the magnitude of $\mathrm{FRE}^2$ for any individual fiducial marker **r** [56]:

$$\left\langle \mathrm{FRE}^2(\mathbf{r}) \right\rangle = \left\langle \mathrm{FLE}^2 \right\rangle \left[ \left( \frac{N-1}{N} \right) - \frac{1}{3} \sum_{i=1}^{3} \frac{d_i^2}{f_i^2} \right], \tag{111}$$

where $N$ is the number of fiducial markers, $\left\langle \mathrm{FLE}^2 \right\rangle$ is the variance of the FLE distribution, $d_i^2$ is the squared distance of the fiducial marker **r** from the principal axis $i$, and $f_i^2$ is the sum of squared distances of all the fiducial points from the principal axis $i$. This formula is not new. It was initially derived by Fitzpatrick *et al.* in 1998 [56] as part of their analysis of the relationship between fiducial misalignment and target registration error (TRE), but the authors did not test its accuracy. As shown in Chapter II, Eq. (111) is also a consequence of results from our derivation of Eq. (110). Therefore, to complete the validation of FRE for a given fiducial marker, the FRE

formula given by (111) is verified in the present work by means of simulations along with the verification of the FRE distribution. We also present towards the end of this chapter an exploration of the response of the individual FRE to changes in the fiducial configuration. This response is not a new theory reported by this dissertation, but is provided to improve the understanding of registration errors. All the simulations were performed using Matlab software (Version 7.5.0.342, R2007b) on a Windows operating system.

## 1. Verification of the FRE Distribution

Six different values are chosen for the number of fiducials, *N*, for the test: *N* = 3, 4, 5, 10, 15, 20. A fiducial matrix *X* with *N* fiducial marker locations is generated by randomly choosing *N* three-dimensional locations with uniform distribution inside a cube of edge 200 mm. $\mathbf{x_i}$ is used to refer to the $i^{\text{th}}$ fiducial marker in *X*, $i = 1, 2, ..., N$. Two sets of simulations are performed for the verification of the FRE distribution. The first simulation is used to predict the distribution based on Eq. (110). (This distribution could be calculated via convolutions of three chi-square-degree-1 distributions but the required numerical evaluation of the integrals is more complex than our simulation approach.) The second simulation is performed to obtain the distribution of FRE for each fiducial marker using the point-based registration algorithm. The steps involved in both the simulations are explained below.

### 1.1. Simulation Based on the Predicted Distribution

1. Compute predicted variances: As derived in Chapter II, the predicted variances $\sigma_r^2$, $\sigma_v^2$, and $\sigma_w^2$ along the three orthogonal directions $\hat{\mathbf{r}}$, $\hat{\mathbf{v}}$, and $\hat{\mathbf{w}}$, respectively, for a fiducial marker **r** are computed as follows:

$$\sigma_r^2 = \sigma^2 \left( \frac{N-1}{N} \right), \tag{112}$$

$$\sigma_v^2 = \sigma^2\left(\frac{N-1}{N}\right) - r^2\omega_w^2, \tag{113}$$

$$\sigma_w^2 = \sigma^2\left(\frac{N-1}{N}\right) - r^2\omega_v^2, \tag{114}$$

where $r$ is the magnitude of the vector $\mathbf{r}$, $\sigma^2$ is the variance of FLE in a given direction, $\omega_v^2 = \sigma^2\sum_{i=1}^{3}\frac{\hat{v}_i^2}{\Lambda_{aa}^2 + \Lambda_{bb}^2}$, $\omega_w^2 = \sigma^2\sum_{i=1}^{3}\frac{\hat{w}_i^2}{\Lambda_{aa}^2 + \Lambda_{bb}^2}$, $\{i,a,b\} = \{1,2,3\}$, $\{2,3,1\}$, or $\{3,1,2\}$, and $[\Lambda_{11} \quad \Lambda_{22} \quad \Lambda_{33}]$ are the singular values of the demeaned version of $X$. $\sigma_r^2$, $\sigma_v^2$, and $\sigma_w^2$ values are computed for each fiducial marker.

2. Generate the distribution of FRE$^2$: For a fiducial marker three sets each of $\mathcal{M}_1$ random values are generated that are drawn from a zero-mean normal distribution with variances computed in the previous step. These represent the three components of FRE along the three orthogonal directions $\hat{\mathbf{r}}$, $\hat{\mathbf{v}}$, and $\hat{\mathbf{w}}$. All the FRE values along the three directions are then squared and added together to obtain the distribution of FRE$^2$ for that fiducial marker. Similarly the distribution is obtained for other fiducial markers.
3. Compute the distribution of FRE: The distribution of FRE for each fiducial marker is obtained by forming a frequency distribution of the square roots of the corresponding FRE$^2$ values generated in the previous step.

### 1.2 Simulation Based on the Point-based Registration Algorithm

1. Generate $Y$: $Y$ is the perturbed set of fiducial marker locations that needs to be registered to $X$. Each fiducial marker's location in $X$ is perturbed along the $x$, $y$, and $z$ directions using normally distributed random variables with zero mean and variance

$\sigma^2$ to obtain the corresponding fiducial marker location in *Y*. $\mathbf{y_i}$ refers to the $i^{\text{th}}$ fiducial marker in *Y*, $i = 1, 2, ..., N$ .

2. Register *X* to *Y*: Point-based registration is performed using the algorithm described in [1] to get the rotation matrix *R* and translation vector **t** by minimizing the total $\text{FRE}^2$ so that for all fiducials $i = 1, 2, ..., N$ , $\mathbf{y_i} \approx R\mathbf{x_i} + \mathbf{t}$ .

3. Compute individual FREs: The individual FRE values for each fiducial marker in *x*, *y*, and *z* directions are measured. If $\mathbf{new\_y_i} = R\mathbf{x_i} + \mathbf{t}$ , then

$$\text{FRE}_x(\mathbf{x_i}) = \text{new\_y}_{ix} - y_{ix}\,, \tag{115}$$

$$\text{FRE}_y(\mathbf{x_i}) = \text{new\_y}_{iy} - y_{iy}\,, \tag{116}$$

$$\text{FRE}_z(\mathbf{x_i}) = \text{new\_y}_{iz} - y_{iz}\,. \tag{117}$$

The overall $\text{FRE}^2$ for the $i^{\text{th}}$ fiducial marker is then computed as follows:

$$\text{FRE}^2(\mathbf{x_i}) = \text{FRE}_x^2(\mathbf{x_i}) + \text{FRE}_y^2(\mathbf{x_i}) + \text{FRE}_z^2(\mathbf{x_i})\,. \tag{118}$$

$\text{FRE}(\mathbf{x_i})$ is then the square root of $\text{FRE}_x^2(\mathbf{x_i})$ thus obtained. The values of $\text{FRE}_x(\mathbf{x_i})$, $\text{FRE}_y(\mathbf{x_i})$, and $\text{FRE}_z(\mathbf{x_i})$ are also used to find the error components for the $i^{\text{th}}$ fiducial marker along the three orthogonal directions $\hat{\mathbf{r}}$ , $\hat{\mathbf{v}}$ , and $\hat{\mathbf{w}}$ , which we will call $\text{FRE}_r(\mathbf{x_i})$, $\text{FRE}_v(\mathbf{x_i})$, and $\text{FRE}_w(\mathbf{x_i})$ respectively. $\text{FRE}_r(\mathbf{x_i})$, $\text{FRE}_v(\mathbf{x_i})$, $\text{FRE}_w(\mathbf{x_i})$, and $\text{FRE}(\mathbf{x_i})$ are computed for all fiducial markers in this manner.

4. Repeat steps 1, 2, and 3 $\mathcal{M}_2$ times.

5. Obtain the distribution of FRE: The distribution of FRE for each fiducial marker is calculated by forming the frequency distribution of the $\mathcal{M}_2$ FRE values computed from the previous steps. The variances $\sigma_r^2$ , $\sigma_v^2$ , and $\sigma_w^2$ of individual fiducial markers along their respective $\hat{\mathbf{r}}$ , $\hat{\mathbf{v}}$ , and $\hat{\mathbf{w}}$ directions are obtained by finding the variances of the $\mathcal{M}_2$ values of $\text{FRE}_r$ , $\text{FRE}_v$ , and $\text{FRE}_w$ respectively.

We choose RMS FLE to be 1 mm, which means that $\sigma^2$ = 1/3 mm$^2$, and we used the $\mathcal{M}_1$ = 500,000 and $\mathcal{M}_2$ = 500,000. The two simulations were repeated for ten different sets $X$ of fiducials for each value of $N$. For each $X$, two sets of 500,000 FRE values were generated for each fiducial marker by the two simulations. The variances $\sigma_r^2$, $\sigma_v^2$, and $\sigma_w^2$ were also computed for each fiducial marker by the two simulations. Table 1 shows a comparison of the variance values for each value of $N$. It compares the variance values as predicted by Eqs. (112), (113), and (114) with those obtained by finding the variances of the $\mathcal{M}_2$ values of $\text{FRE}_r$, $\text{FRE}_v$, and $\text{FRE}_w$ respectively from the second simulation. For each value of $N$, the fiducial marker that had the maximum difference between the simulated and predicted variance values among all the 10 sets of $X$ was selected, and the variance values corresponding to that fiducial marker are reported in Table 1.

Table 2 reports the mean and standard deviation values of the differences of the variance values along the $r$, $v$, and $w$ directions corresponding to all the fiducial markers for a particular $N$ value. For example, for the case $N$ = 4 we have 40 fiducial markers from the 10 sets of $X$ that were used. There are two sets of 40 values of $\sigma_r^2$, $\sigma_v^2$, and $\sigma_w^2$, where the two sets correspond to the predicted variances and the variances of the $M_2$ values of $\text{FRE}_r$, $\text{FRE}_v$, and $\text{FRE}_w$. Table 2 reports the mean and standard deviation of the differences between these two sets of values. We see that the differences are close to zero for all cases. The differences between simulated and theoretical values were compared using a paired t-test (p = 0.05). The differences were insignificant for all cases except for $N$ = 3 and 4 in the $\hat{\mathbf{w}}$ direction (p = 0.009740 and 0.047978 respectively).

**Table 1.** Variance values along the *r*, *v*, and *w* directions for the fiducial marker with maximum difference. (All units are in $mm^2$.)

| *N* | Predicted Values | | | Simulated Values | | | Maximum difference |
|---|---|---|---|---|---|---|---|
| | $\sigma_r^2$ | $\sigma_v^2$ | $\sigma_w^2$ | $\sigma_r^2$ | $\sigma_v^2$ | $\sigma_w^2$ | |
| 3 | 0.2222 | 0.0556 | 0.0000 | 0.2210 | 0.0557 | 0.0000 | -0.0012 |
| 4 | 0.2500 | 0.1315 | 0.0569 | 0.2514 | 0.1314 | 0.0568 | 0.0014 |
| 5 | 0.2667 | 0.0838 | 0.2001 | 0.2680 | 0.0837 | 0.2000 | 0.0013 |
| 10 | 0.3000 | 0.2940 | 0.2916 | 0.3002 | 0.2918 | 0.2913 | -0.0021 |
| 15 | 0.3111 | 0.2558 | 0.2617 | 0.3112 | 0.2566 | 0.2635 | 0.0017 |
| 20 | 0.3167 | 0.3115 | 0.3107 | 0.3168 | 0.3094 | 0.3115 | -0.0021 |

**Table 2.** Mean and standard deviation values of the differences in the variance values along the *r*, *v*, and *w* directions. (All units are in $mm^2$.)

| *N* | Mean and standard deviation of the differences in the variances (predicted variance – simulated variance) | | |
|---|---|---|---|
| | $\hat{\mathbf{r}}$ | $\hat{\mathbf{v}}$ | $\hat{\mathbf{w}}$ |
| 3 | 0.00007 ± 0.00046 | 0.00002 ± 0.00032 | -0.00007 ± 0.00013 |
| 4 | -0.00005 ± 0.00047 | -0.00001 ± 0.00022 | 0.00008 ± 0.00026 |
| 5 | -0.00003 ± 0.00054 | 0.00001 ± 0.00032 | 0.00001 ± 0.00031 |
| 10 | 0.00002 ± 0.00052 | 0.00001 ± 0.00050 | 0.00000 ± 0.00048 |
| 15 | -0.00001 ± 0.00057 | 0.00003 ± 0.00060 | -0.00002 ± 0.00053 |
| 20 | -0.00006 ± 0.00063 | 0.00004 ± 0.00057 | 0.00001 ± 0.00053 |

Figure 3 shows superimposed plots of probability distribution functions (pdf) of FRE for a fiducial marker obtained from the two simulations for different values of *N*. The stars refer to the pdf of the $\mathcal{M}_1$ FRE values (predicted distribution), and the solid line refers to the distribution obtained using the $\mathcal{M}_2$ FRE values. The fiducial marker for the plots was chosen to be the one

that had the maximum absolute percentage difference in the mean FRE values. We see that the plots match very closely suggesting that our approximate theoretical formulation as specified by Eq. (110) is accurate. The Kolmogorov-Smirnov test [65] was performed to compare the two distributions for the fiducial marker whose pdfs are shown in Figure 3. No significant difference was found between the two distributions for $N$ = 3, 4, 10, 15 and 20. For the case $N$ = 5, there was a significant difference (K-S test, p = 0.000336).

Figure 4 shows superimposed plots of the cumulative distribution functions (cdf) of FRE for a fiducial marker obtained from the two simulations for different values of $N$. The stars refer to the cdf of the $\mathcal{M}_1$ FRE values (predicted distribution), and the solid line refers to the distribution obtained using the $\mathcal{M}_2$ FRE values. The chosen fiducial marker for the plots was the one with maximum absolute percentage difference in the mean FRE values. We again see that our predicted distribution is accurate.

Figure 5 shows a plot of corresponding percentile values (stars) of FRE from the two simulations for the fiducial marker with maximum absolute percentage difference in the mean FRE values. The $x$ axis represents the percentile values for the FRE values obtained from the simulation based on point-based registration algorithm in increments of 5% ranging from $5^{th}$ to $95^{th}$ percentile value. The $y$ axis represents the same percentiles for the FRE values obtained from the simulation based on the predicted distribution. The percentile plot closely follows the straight line along $x = y$ (solid line) showing that the results from the two simulations match each other closely. This strongly indicates that our predicted distribution given by (110) is valid for the configurations on which we tested it.

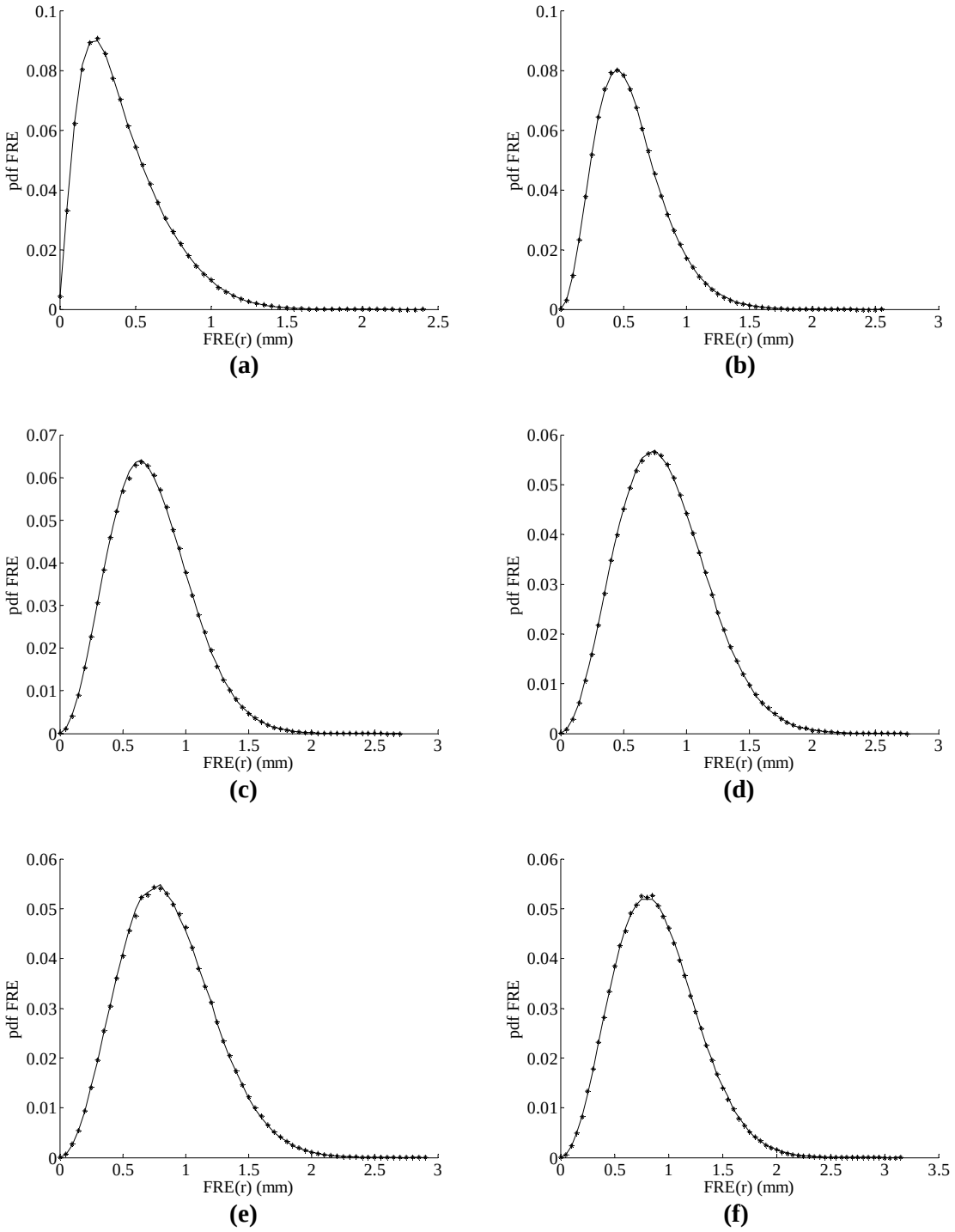


**Figure 3.** Superimposed plots of probability distribution functions of FRE of a fiducial marker obtained from the simulation based on the predicted variances (stars) and the simulation based on point-based registration algorithm (solid line) for different values of *N***.** The plot corresponds to the fiducial marker that had the maximum absolute percentage difference in the mean FRE values. (a) $N = 3$, (b) $N = 4$, (c) $N = 5$, (d) $N = 10$, (e) $N = 15$, and (f) $N = 20$.

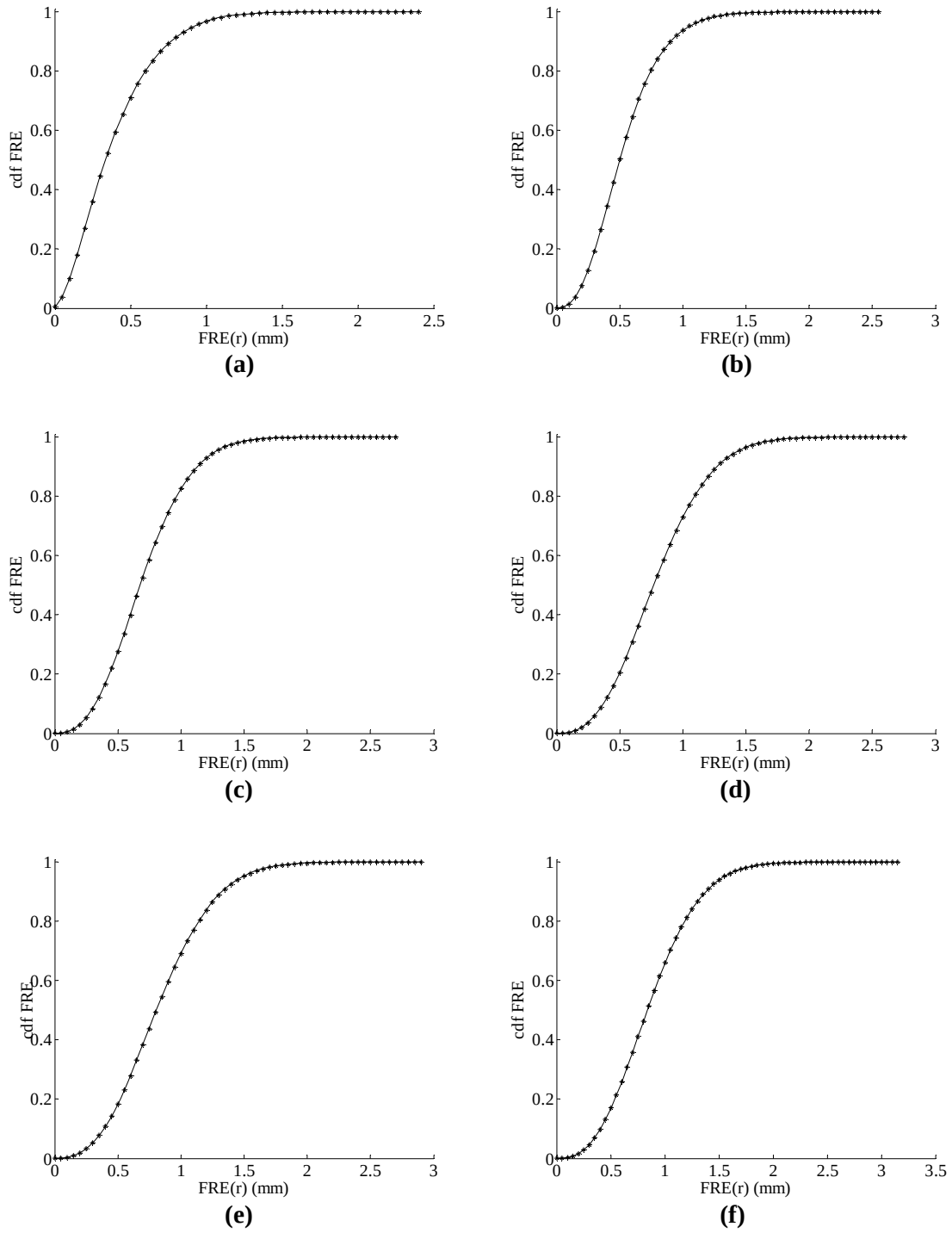


**Figure 4.** Superimposed plots of cumulative distribution functions of FRE obtained from the simulation based on the predicted variances (stars) and the simulation based on point-based registration algorithm (solid line) for different values of *N*. The plot corresponds to the fiducial marker that had the maximum absolute percentage difference in the mean FRE values. (a) $N = 3$, (b) $N = 4$, (c) $N = 5$, (d) $N = 10$, (e) $N = 15$, and (f) $N = 20$.

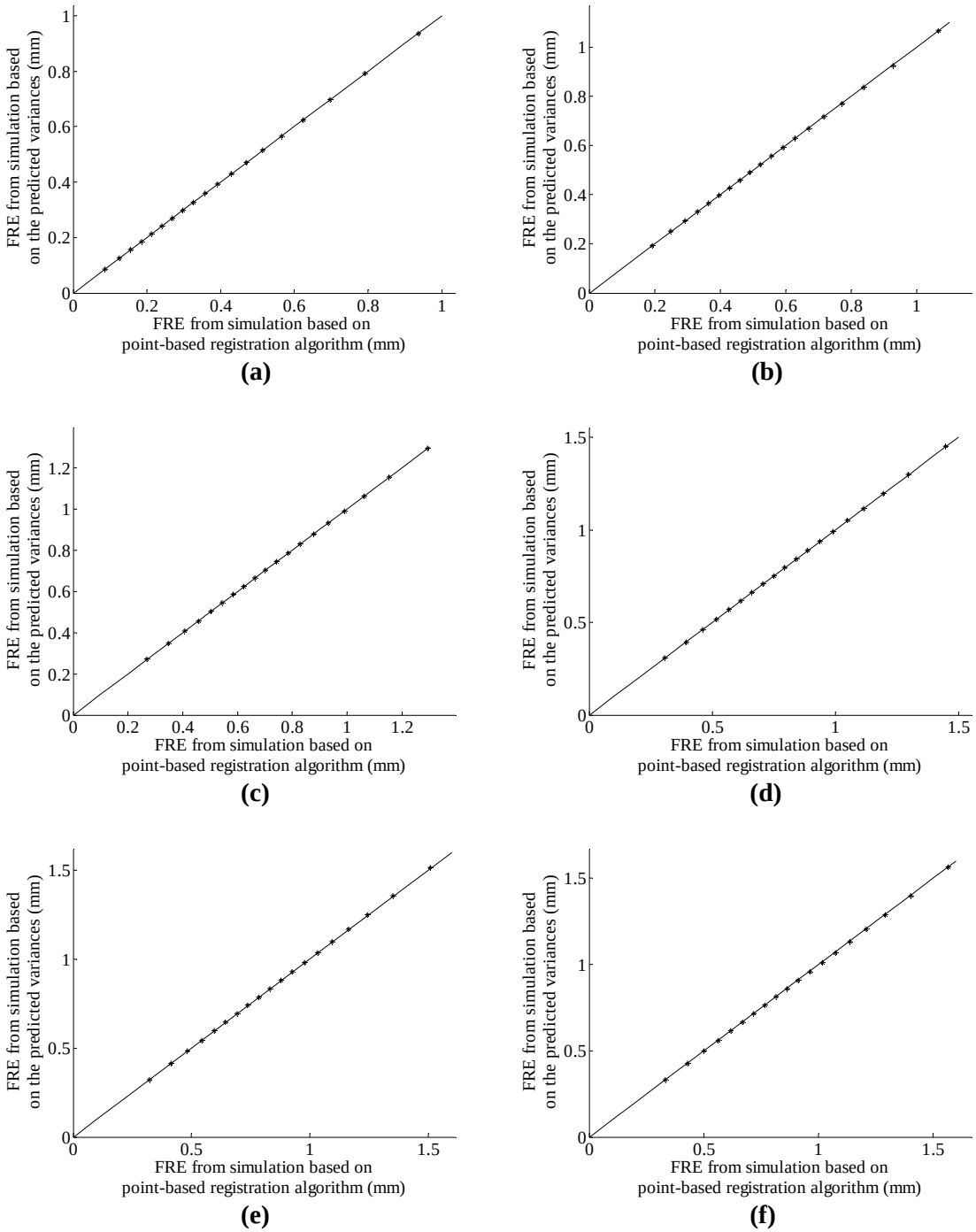


**Figure 5.** Plot of corresponding percentile values for FRE values of a fiducial marker (stars) from the two simulations from 5% to 95% in 5% increments. The *x* and *y* axes represent the percentile values for the FRE values obtained from the simulation based on point-based registration algorithm and the predicted distribution respectively. The plot corresponds to the fiducial marker that had the maximum absolute percentage difference in the mean FRE values. The solid line is the plot of points along the straight line $x = y$. All the stars lie almost on the line implying that the results from the two simulations match each other. (a) $N = 3$, (b) $N = 4$, (c) $N = 5$, (d) $N = 10$, (e) $N = 15$, and (f) $N = 20$.

### 2. Verification of the Variance of FRE along Arbitrary Direction

The same six values of $N$ were chosen once again: $N$ = 3, 4, 5, 10, 15, 20. The $X$ fiducial matrix is generated as before for each value of $N$. The simulation based on the point-based registration algorithm is performed for each value of $N$ as described before. As before, RMS FLE is set at 1 mm . Using the resultant $\mathcal{M}_2$ values of $\text{FRE}_x$, $\text{FRE}_y$, and $\text{FRE}_z$, the variances $\sigma_x^2$, $\sigma_y^2$, and $\sigma_z^2$ in the $x$, $y$, and $z$ directions respectively are computed for each fiducial marker.

Predicted variances $\sigma_r^2$, $\sigma_v^2$, and $\sigma_w^2$ along the three orthogonal directions $\hat{\mathbf{r}}$, $\hat{\mathbf{v}}$, and $\hat{\mathbf{w}}$, respectively, are computed for each fiducial marker as described before using Eqs. (112), (113), and (114). The expected variance in the $x$, $y$, and $z$ directions are computed using the following formula that was derived in Chapter II to find the variance of the component of FRE along any arbitrary direction $\hat{\mathbf{a}}$:

$$\sigma_a^2(\mathbf{r}) = \sigma^2\left(\frac{N-1}{N}\right) - r^2\left(\hat{a}_v^2\omega_w^2 + \hat{a}_w^2\omega_v^2\right), \tag{119}$$

where $\hat{a}_v = \hat{\mathbf{a}}\cdot\hat{\mathbf{v}}$ and $\hat{a}_w = \hat{\mathbf{a}}\cdot\hat{\mathbf{w}}$. The variances $\sigma_x^2$, $\sigma_y^2$, and $\sigma_z^2$ along the $x$, $y$, and $z$ directions are computed with $\hat{\mathbf{a}}$ = $\hat{\mathbf{x}}$, $\hat{\mathbf{y}}$, and $\hat{\mathbf{z}}$, respectively. Because of the randomness of the fiducial configurations, $\hat{\mathbf{x}}$, $\hat{\mathbf{y}}$, and $\hat{\mathbf{z}}$ represent arbitrary directions relative to $\hat{\mathbf{r}}$, $\hat{\mathbf{v}}$, and $\hat{\mathbf{w}}$. We choose these particular three vectors simply for programming convenience.

The variance values $\sigma_x^2$, $\sigma_y^2$, and $\sigma_z^2$ were computed for each fiducial marker for ten different sets of $X$ for each value of $N$. $\mathcal{M}_2$ = 500,000 was used for the simulations. The variance values were also computed using Eq. (119) by setting $\hat{\mathbf{a}}$ = $\hat{\mathbf{x}}$, $\hat{\mathbf{y}}$, and $\hat{\mathbf{z}}$.

Table 3 compares the resultant predicted variances using Eq. (119) with that from the simulation for the fiducial marker that had the maximum difference between the simulated and predicted variance values. We can see that the simulated and predicted results match very closely.

**Table 3.** Variance values along the *x*, *y*, and *z* directions for the fiducial marker with maximum difference. (All units are in $mm^2$.)

| *N* | Predicted Values | | | Simulated Values | | | Maximum difference |
|---|---|---|---|---|---|---|---|
| | $\sigma_x^2$ | $\sigma_y^2$ | $\sigma_z^2$ | $\sigma_x^2$ | $\sigma_y^2$ | $\sigma_z^2$ | |
| 3 | 0.1825 | 0.0243 | 0.2061 | 0.1814 | 0.0244 | 0.2057 | -0.0008 |
| 4 | 0.2434 | 0.1111 | 0.0839 | 0.2450 | 0.1109 | 0.0837 | 0.0017 |
| 5 | 0.2286 | 0.2235 | 0.1276 | 0.2286 | 0.2225 | 0.1277 | -0.0001 |
| 10 | 0.2946 | 0.2967 | 0.2943 | 0.2928 | 0.2966 | 0.2939 | -0.0018 |
| 15 | 0.2674 | 0.2747 | 0.2988 | 0.2656 | 0.2741 | 0.2986 | 0.0014 |
| 20 | 0.3157 | 0.3128 | 0.3134 | 0.3162 | 0.3149 | 0.3134 | -0.0002 |

**Table 4.** Mean and standard deviation values of the differences in the variance values along the *x*, *y*, and *z* directions. (All units are in $mm^2$.)

| *N* | Mean and standard deviation of the differences in the variances (predicted variance – simulated variance) | | |
|---|---|---|---|
| | $\hat{\mathbf{x}}$ | $\hat{\mathbf{y}}$ | $\hat{\mathbf{z}}$ |
| 3 | 0.00004 ± 0.00033 | -0.00002 ± 0.00019 | 0.00000 ± 0.00026 |
| 4 | -0.00002 ± 0.00041 | 0.00001 ± 0.00024 | 0.00004 ± 0.00035 |
| 5 | -0.00002 ± 0.00039 | 0.00004 ± 0.00034 | -0.00002 ± 0.00041 |
| 10 | 0.00004 ± 0.00052 | 0.00002 ± 0.00050 | -0.00003 ± 0.00051 |
| 15 | 0.00007 ± 0.00056 | -0.00002 ± 0.00060 | -0.00005 ± 0.00052 |
| 20 | -0.00000 ± 0.00054 | -0.00001 ± 0.00057 | 0.00001 ± 0.00055 |

Table 4 reports the mean and standard deviation values of the differences in the variance values along the *x*, *y*, and *z* directions corresponding to all the fiducial markers for a particular *N* value. We see that the difference is very close to zero for all cases. No significant difference was found between simulated and predicted values (p = 0.05). This indicates that our approximate

prediction of variance of FRE along an arbitrary direction works well for all the fiducial configurations that we tested on.

## 3. Extreme Case Analysis

We have seen that our predicted distribution works well for the cases on which we tested it. Our predicted distribution is an approximation up to first order of a rotation matrix, and it assumes that the second order term of the rotation matrix $R^{(2)}$ and other higher order terms are negligible. When this second order term becomes big, then our approximation will not work. As pointed out in [57], $R^{(2)}$ can be expected to be negligible as long as $\left\langle \mathrm{FLE}^2 \right\rangle$ is small compared to each of the moments of the fiducial configuration about its principal axes. This requirement holds for all reasonable fiducial configurations, which may be planar but not collinear, and for all reasonable FLEs. It may not hold though, when the fiducials are arranged in a near-collinear configuration and FLE is large. In this section we examine examples of extreme cases of linearity and large FLE. To generate these extreme cases we restrict the size of the box from which we randomly choose the fiducial markers. As before, simulations are then performed based on the predicted distribution and on the point-based registration algorithm to generate $\mathcal{M}_1$ and $\mathcal{M}_2$ values, respectively, of individual FRE values for each marker. The results from the two simulations are then compared.

$N = 4$ was chosen for this analysis. Three different box sizes were used for generating the $X$ fiducial matrix in order to compare the effect of the fiducial configuration on the results. The dimensions of the boxes were chosen to be:

1. Box1: 20 mm x 60 mm x 120 mm
2. Box2: 2 mm x 6 mm x 120 mm
3. Box3: 0.2 mm x 0.6 mm x 120 mm

Randomly chosen configurations from these three boxes can be expected to produce more linear fiducial configurations than those chosen from within the cubic boxes of our earlier simulations. The configurations will be moderately linear, highly linear, and extremely linear for boxes 1, 2, and 3 respectively.

A set of 3-by-$N$ random numbers were generated from a uniform distribution on a unit interval. They were then used to select random points in the three boxes to get a set of $X$ in each box. RMS FLE values of 1 mm, 3 mm, and 5 mm were used for the perturbation to study the effect of FLE. $\mathcal{M}_1$ = 100,000 and $\mathcal{M}_2$ = 100,000 were chosen for the two simulations. Figure 6, Figure 7, and Figure 8 show the effects of increase in the FLE on the fiducial markers inside Box1, Box2, and Box3 respectively. The superimposed probability density function plots, superimposed cumulative distribution function plots, and percentile plots are shown for each of the cases. In each case, the plots correspond to the fiducial marker which had the maximum absolute percentage difference in the mean FRE values from the two simulations—i.e., the worst case in agreement between our theory and experiment. We see from the plots that the distribution of FRE values of a fiducial marker from the two simulations match closely for RMS FLE = 1 mm for all three boxes, and inside Box1 for all values of RMS FLE that we simulated. We also see that the distributions match visibly for Box2 when RMS FLE is 1 mm or 3 mm, but when the RMS FLE reaches 5 mm a difference is just visible for Box2. The differences are clearly visible for Box3 when RMS FLE is 3 mm or 5 mm. A K-S test confirms these differences: Box1—no differences, Box2—no difference at 1 mm, different at 3 mm (not visibly different in our plots) and 5 mm (visibly different in our plots), Box3—no difference at 1 mm, but different at 3 mm (visibly different in our plots) and 5 mm (visibly different in our plots).

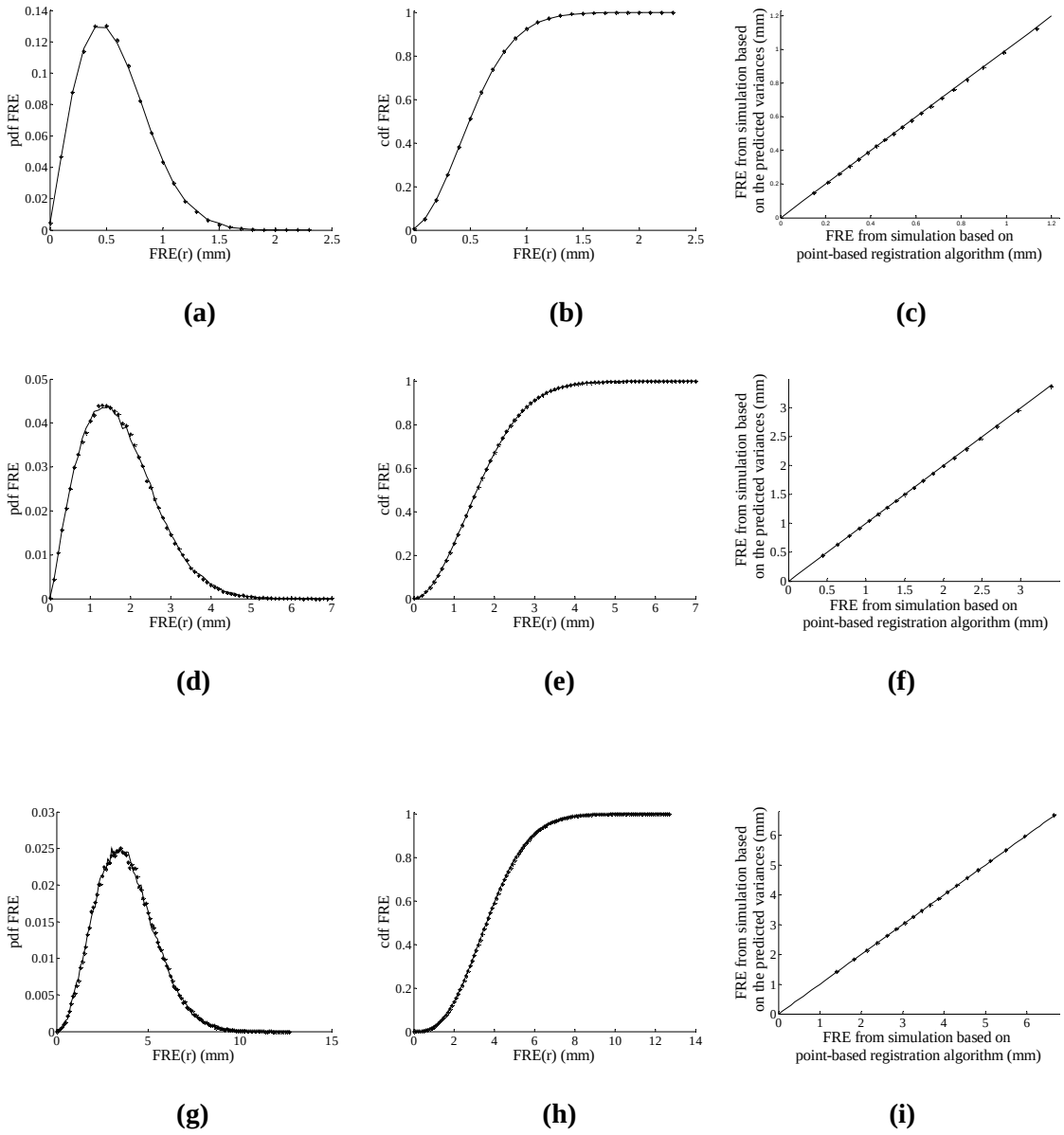


**Figure 6.** Effect of FLE on fiducial markers chosen inside Box1. (a, b, c) RMS FLE = 1 mm. (d, e, f) RMS FLE = 3 mm. (g, h, i) RMS FLE = 5 mm. (a, d, g) Superimposed plots of probability distribution functions. (b, e, h) Superimposed plots of cumulative distribution functions. The stars represent the results of the simulation based on the predicted variances, and the solid line represents the results of the simulation based on point-based registration algorithm. (c, f, i) Plot of corresponding percentile values for FRE values of a fiducial marker (stars) from the two simulations. The solid line represents the straight line $x = y$. We see that the results from both the simulations match closely for all the cases.

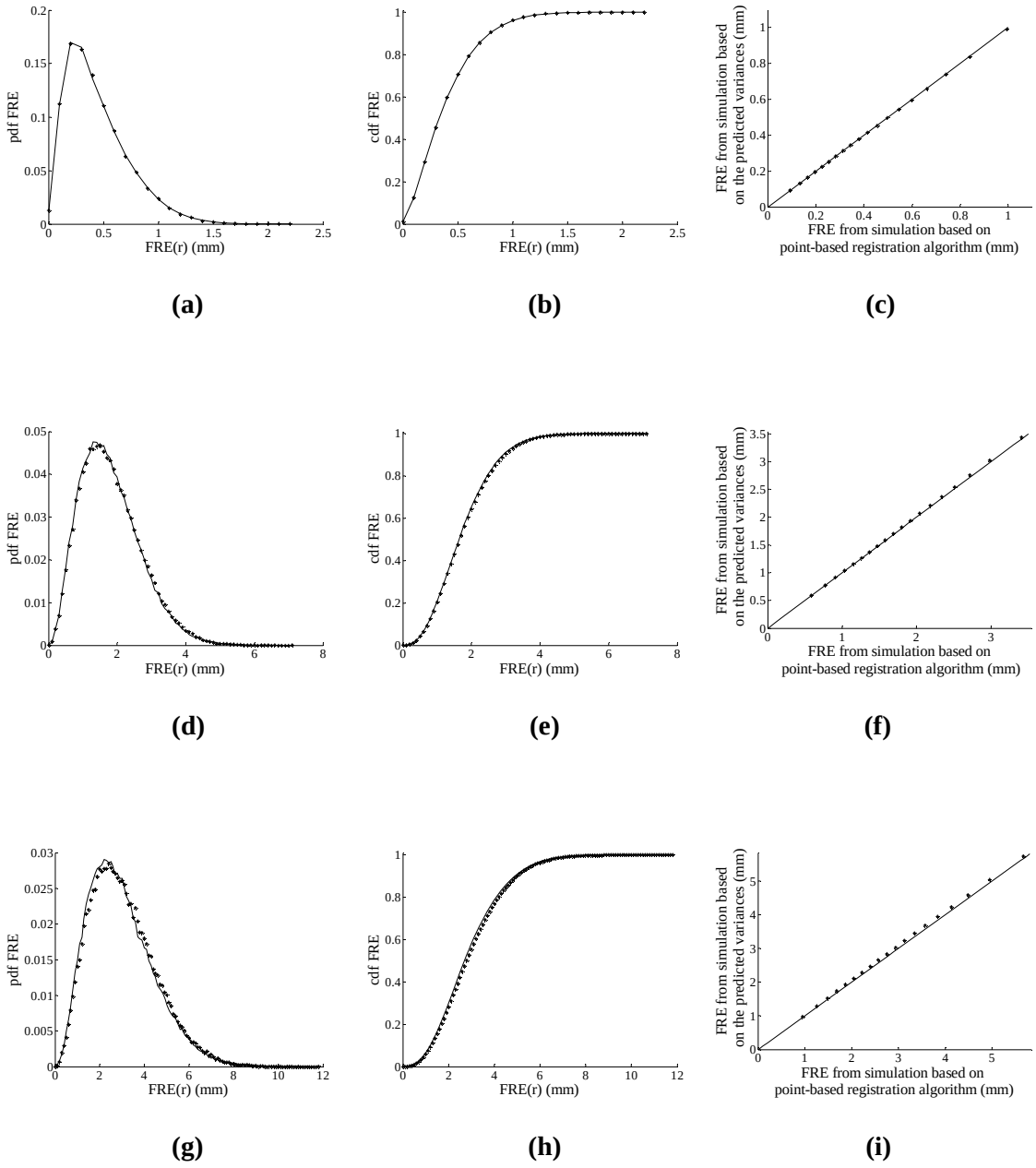


**Figure 7.** Effect of FLE on fiducial markers chosen inside Box2. (a, b, c) RMS FLE = 1 mm. (d, e, f) RMS FLE = 3 mm. (g, h, i) RMS FLE = 5 mm. (a, d, g) Superimposed plots of probability distribution functions. (b, e, h) Superimposed plots of cumulative distribution functions. The stars represent the results of the simulation based on the predicted variances, and the solid line represents the results of the simulation based on point-based registration algorithm. (c, f, i) Plot of corresponding percentile values for FRE values of a fiducial marker (stars) from the two simulations. The solid line represents the straight line $x = y$. We see that the results from both the simulations match visually for the cases RMS FLE = 1 mm and 3 mm. There are small but just discernable differences in the results for RMS FLE = 5 mm.

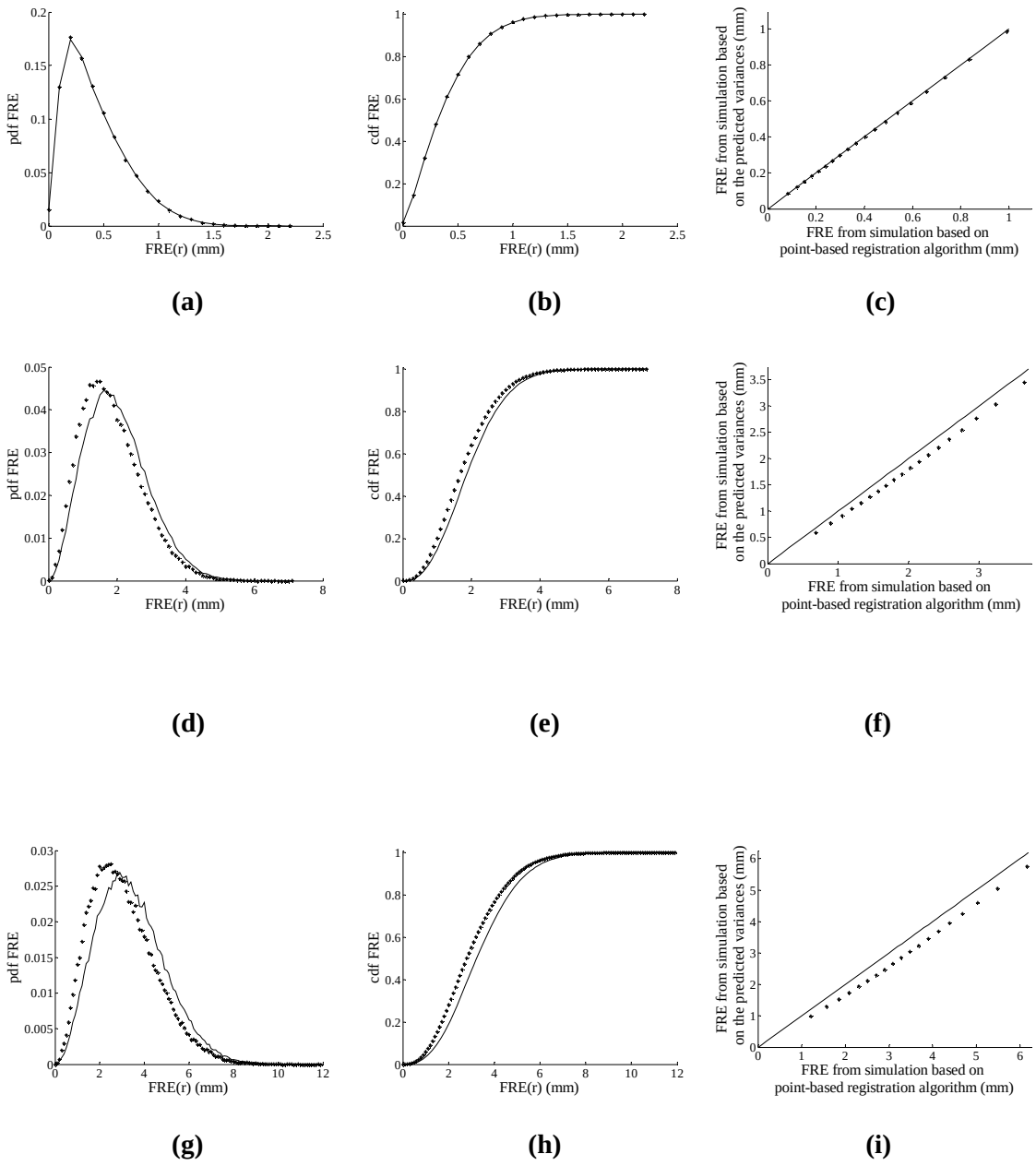


**Figure 8.** Effect of FLE on fiducial markers chosen inside Box3. (a, b, c) RMS FLE = 1 mm. (d, e, f) RMS FLE = 3 mm. (g, h, i) RMS FLE = 5 mm. (a, d, g) Superimposed plots of probability distribution functions. (b, e, h) Superimposed plots of cumulative distribution functions. The stars represent the results of the simulation based on the predicted variances, and the solid line represents the results of the simulation based on point-based registration algorithm. (c, f, i) Plot of corresponding percentile values for FRE values of a fiducial marker (stars) from the two simulations. The solid line represents the straight line $x = y$. We see that the results from both the simulations match closely for the case when RMS FLE = 1 mm, but they differ noticeably when the FLE is 3 mm or 5 mm.

We find that for linear configuration, when RMS FLE is sufficiently high, there are discernable and statistically significant differences between theory and experiment. It is important to recognize the possibility of this failure and to apply the predicted distribution only for those fiducial configurations where it is valid. However, we note that the fiducial configurations and RMS FLE values treated here, for which the predicted distribution fails, are extreme cases. For the application we concentrate on, which is image-to-image registration or image-to-physical registration based on fiducial markers attached to patients, these cases should never occur with properly working systems in the hands of knowledgeable practitioners.

## 4. Verification of Equation (111)

In this section we test the validity of the effect of fiducial position on individual FRE given by Eq. (111). The same six values of $N$ were chosen for this verification also, i.e., $N$ = 3, 4, 5, 10, 15, 20. The $X$ matrix is generated as before for each value of $N$. The simulation for this verification involved steps 1 through 4 of the simulation based on the point-based registration algorithm. As before, RMS FLE is set to 1 mm. For the verification of Eq. (111), we are concerned only with the computation of the $FRE^2$ values of each fiducial marker using Eq. (118). The mean $FRE^2$ value for each fiducial marker is computed from the $\mathcal{M}_2$ $FRE^2$ values for each fiducial marker. The $FRE^2$ values are compared with the values computed using the FRE formula given by Eq. (111).

For this verification $\mathcal{M}_2$ = 100,000 was chosen for the simulations. The mean $FRE^2$ was computed for each fiducial marker. Equation (111) was used to compute the expected value of $FRE^2$ for all the fiducial marker locations. This process was repeated for ten different sets of $X$ for each value of $N$. Table 5 compares the predicted values with the simulation results of $FRE^2$ for the fiducial marker that had the maximum absolute percentage difference between the two values from all the ten sets of X. We see that for all the cases the absolute percentage difference is less

than 1%. The last column of the table reports the mean and standard deviation values of the percentage difference for all the fiducial markers. We observe less than 0.1% absolute mean percentage values for all the cases. No significant difference was found between simulated and predicted values (p = 0.05). These results are strong evidence that (111) given by Fitzpatrick *et al*. in [56] is accurate even though it is an approximation. We will use this equation from now on to investigate the effect of FLE and fiducial configuration on $FRE^2$ of individual fiducial markers.

**Table 5.** Mean $FRE^2$ values from simulation and using Eq. (111).

| Number of fiducials | $\langle FRE^2(\mathbf{x}_i)\rangle$ ($mm^2$ units) | | Difference ($mm^2$) | Absolute % difference | % difference Mean ± Standard deviation |
|---|---|---|---|---|---|
| | Simulated | Predicted | | | |
| 3 | 0.2767 | 0.2789 | -0.0021 | 0.7702 | -0.08390 ± 0.29184 |
| 4 | 0.4069 | 0.4093 | -0.0024 | 0.5984 | -0.06944 ± 0.28874 |
| 5 | 0.5749 | 0.5788 | -0.0039 | 0.6759 | -0.00960 ± 0.28192 |
| 10 | 0.8344 | 0.8284 | 0.0060 | 0.7165 | -0.00098 ± 0.24398 |
| 15 | 0.8611 | 0.8678 | -0.0067 | 0.7816 | 0.00465 ± 0.28232 |
| 20 | 0.9069 | 0.9134 | -0.0065 | 0.7170 | 0.00524 ± 0.25321 |

## 5. Effect of FLE on FRE

In this section we analyze the effect of FLE on the individual FRE. For this analysis we used two sets of fiducial markers as follows:

1. Fiducial set 1: $N = 4$ was chosen for this set. The fiducial markers in $X$ were placed on a rectangle in the yz plane of width 200 mm and height 100 mm centered on the origin as follows: $(x, y, z) =$ (0, 100, -50), (0, -100, -50), (0, 100, 50), and (0, -100, 50) (units of mm).

2. Fiducial set 2: $N = 5$ was chosen for this set. This set had all the fiducial markers in the first set and a fifth marker lying on the x axis 50 mm from the center of the rectangle: $(x, y, z)$ = (50, 0, 0) (units of mm).

The expected $FRE^2$ value for each fiducial marker was computed using Eq. (111) with different values of $FLE^2$ ranging from 0 to 10 $mm^2$ in steps of 0.5 $mm^2$. The overall $FRE^2$ value was also computed for each case as the mean of the $FRE^2$ of all the individual fiducial markers. Figure 9 shows the plot of expected values of $FRE^2$ for each fiducial marker and the overall $FRE^2$ thus obtained for different values of $FLE^2$ for both the fiducial sets. The line in Figure 9(a) and the lower line in Figure 9(b) each refer to the 1st through 4th fiducial markers. Their four lines are identical because of their symmetric arrangement. The upper line in Figure 9(b) refers to the fifth fiducial marker in the second fiducial set. The stars represent the overall $FRE^2$ values. We can see that as $FLE^2$ increases, the individual $FRE^2$ for all fiducial markers increases linearly. The individual $FRE^2$ is directly proportional to $FLE^2$ and hence FLE. This is similar to the dependence of overall $FRE^2$ on FLE.

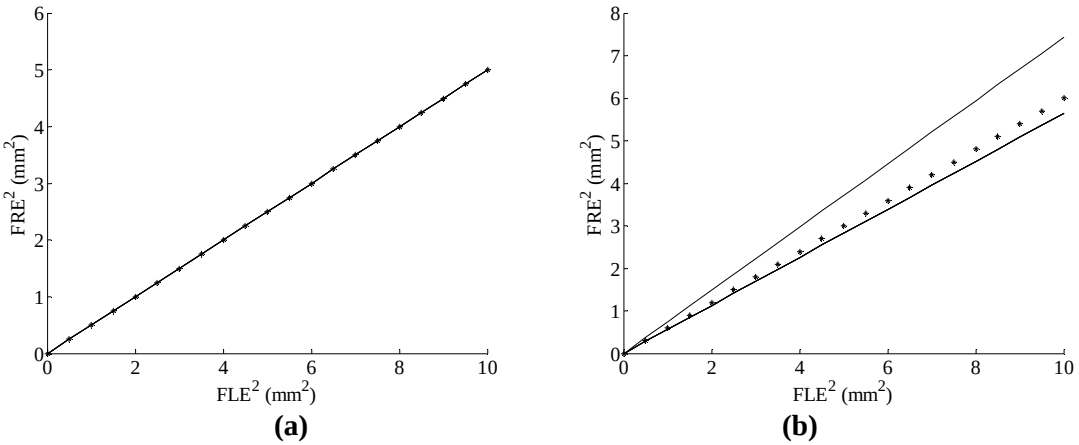


**Figure 9.** Plot of expected values of $FRE^2$ for each fiducial marker and overall $FRE^2$ for different values of $FLE^2$ ranging from 0 to 10 $mm^2$ in steps of 0.5 $mm^2$. (a) Fiducial set 1 with four fiducial markers. (b) Fiducial set 2 with five fiducial markers. The line in (a) and the lower line in (b) are each for fiducials 1 to 4, which all have the same values because of their symmetrical positions. The upper line in (b) is for fiducial 5. The stars represent the overall $FRE^2$ values.

## 6. Effect of Fiducial Configuration on FRE

In this section we will analyze the effect of the fiducial configuration, such as the number of fiducial markers, *N*, and variation in the arrangement of the fiducial markers, on FRE of an individual marker. The effect of *N* on FRE was studied by choosing different numbers of fiducial markers lying on a circle. A circle was selected because it is the only shape for which complete symmetry can be maintained regardless of the number of fiducials. Thus, the effect of changing *N* can be studied without any effects from changing the symmetry. Complete symmetry also simplifies the analysis because FRE is identical for each fiducial. *X* was generated with *N* fiducial markers at equal intervals on a circle of radius 100 mm. *N* was varied from 3 to 20. For each *N*, the expected individual $FRE^2$ values for each fiducial marker were computed using Eq. (111) with RMS FLE set to 1 mm. The overall $FRE^2$ value was also computed as the mean of the $FRE^2$ of all the individual fiducial markers. Since the fiducial markers were symmetrically arranged, the $FRE^2$ value was analyzed for just one of the fiducial markers. Because FLE is isotropic, the orientation of the circle has no effect. Thus, without loss of generality, the circle was chosen to lie in the yz-plane. Figure 10 shows the plot of expected $FRE^2$ of a fiducial marker (stars) in the fiducial system and the overall $FRE^2$ (triangles) with change in *N*. We see that $FRE^2$ value of the fiducial marker increases as *N* increases, but the rate of increase decreases with increase in the value of *N*. The ratio $(N-1)/N$ decreases with increase in *N*, which results in the decrease in the rate of increase of $FRE^2$ value with increase in *N*. This effect is similar to the effect of *N* on the overall $FRE^2$.

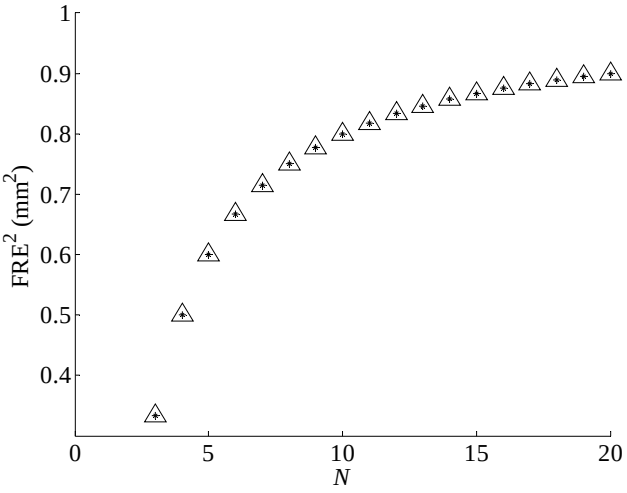


**Figure 10.** Plot of expected $FRE^2$ values of a fiducial marker (stars) and overall $FRE^2$ (triangles) for different values of *N* ranging from 3 to 20. *N* fiducial markers were chosen at equal intervals on a circle of radius 100 mm.

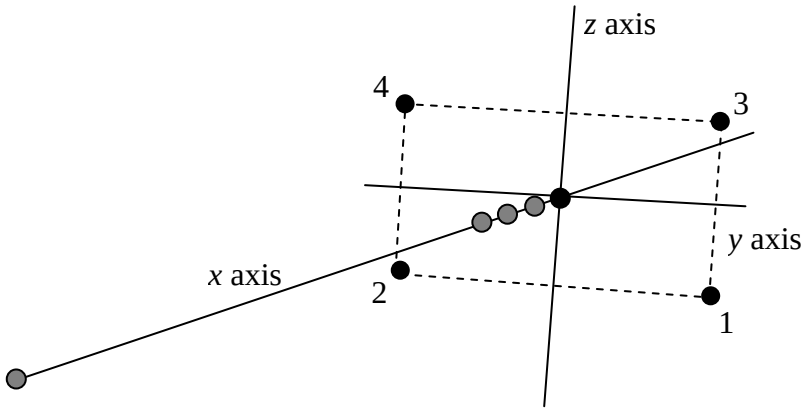


**Figure 11.** Fiducial configurations used to study the effect of configuration on FRE. The black circles show the initial configuration of the 5 fiducials. Fiducials 1-4 are numbered. The 5$^{th}$ is at the origin. The gray circles show the second, third, fourth, and 100$^{th}$ position of the 5$^{th}$ fiducial after it has been moved to produce the other configurations.

To study the effect of the variation in arrangement of fiducial markers on individual $FRE^2$, an initial fiducial configuration is chosen with 5 fiducial markers. One of the fiducial markers is

moved away from other markers, and the effect on the individual $FRE^2$ of fiducial markers and the effect on the overall $FRE^2$ are studied. The configurations are depicted in Figure 11.

The initial set of fiducial markers in $X$ was placed on the same rectangle used earlier lying in the yz plane and centered on the origin: $(x, y, z)$ = (0, 100, -50), (0, -100, -50), (0, 100, 50), and (0, -100, 50) (units of mm), but with a fifth fiducial placed at the origin (0, 0, 0). The expected value of individual $FRE^2$ for each fiducial marker was computed using Eq. (111) for this initial set of fiducial markers. The expected value of overall $FRE^2$ was computed as the mean of the individual $FRE^2$ of all the fiducial markers. Then the last fiducial marker was moved away from the other four fiducial markers by increasing its $x$ coordinate by 5 mm and changing its location to (5, 0, 0). The expected values of individual $FRE^2$ for each marker and the overall $FRE^2$ were computed. The $x$ coordinate of the last fiducial marker was again increased by 5 mm, and the expected values of individual $FRE^2$ for each marker and the overall $FRE^2$ were again computed. This was repeated till we had increased the $x$ coordinate's value to 500 mm. RMS FLE was set to 1 mm for all cases. Figure 12 shows effects of this change. The dotted line refers to fiducial markers 1-4. We see that they all overlap because of the symmetry in their arrangement. The solid lines correspond to the $5^{th}$ fiducial marker. The dashdot line represents the expected value of the overall $FRE^2$ value. Figure 12(a) shows the variation of the expected values of individual and overall $FRE^2$ with change in the distance of the $5^{th}$ fiducial from the origin. We note that the expected values of $FRE^2$ for the $5^{th}$ fiducial marker decreases with increase in distance, but at the same time the expected values of $FRE^2$ for each of the other four fiducial markers increases. According to Eq. (111), their respective changes are due to the variation of the distance-square ratio $\sum_{i=1}^{3} d_i^2 / f_i^2$ for each fiducial marker with change in the position of any fiducial marker. Figure 12(b) shows the variation of this distance-square ratio for each fiducial marker with change in the position of the last marker. The distance-square ratio decreases with increase in distance for the $5^{th}$ marker but increases for other markers. Thus, we can explain the

variation in the expected values of $FRE^2$ for individual fiducial markers with this change in the distance square ratio. Looking at Eq. (111), we can see that expected value of individual $FRE^2$ increase with decrease in the distance square ratio and decreases with increase in the distance square ratio. Figure 12(c) shows the variation of the expected values of individual and overall $FRE^2$ with change in the distance square ratio. For this plot, the *x* axis represents the values for the distance square ratio ( $\sum_{i=1}^{3} d_i^2 / f_i^2$ ) for the 5th fiducial marker. We can see clearly that the effect of the change in this value on the expected values of individual $FRE^2$ is linear. The expected values of overall $FRE^2$ though remain a constant throughout. This constancy and its dependence on FLE and *N* seen before agree with the result of Sibson's work in 1979 [55] according to which the overall $FRE^2$ is given by

$$\left\langle \mathrm{FRE}^2 \right\rangle = (1 - 2/N)\left\langle \mathrm{FLE}^2 \right\rangle . \tag{120}$$

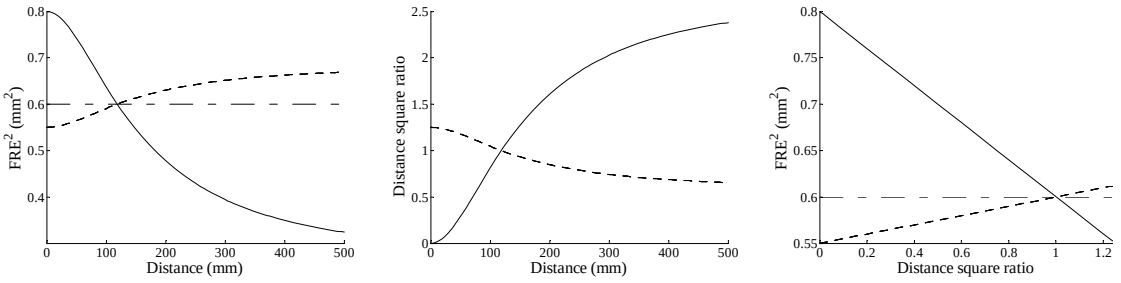


**Figure 12.** Effect of varying the fiducial marker arrangement by changing the distance of a fiducial marker along the *x* direction. (a) Plot of expected values of individual and overall $FRE^2$ with respect to change in distance. (b) Plot of variation of the distance square ratio with change in distance. (c) Plot of expected values of individual and overall $FRE^2$ with respect to change in the distance square ratio. The dotted line refers to fiducial markers 1-4. The solid line refers to the 5th fiducial marker. The dashdot line refers to the expected values of overall $FRE^2$.

Similar simulations were repeated by changing the *y* and *z* coordinates values of the 5th fiducial marker as we did with the *x* coordinates. Figure 13 and Figure 14 show plots similar to those in Figure 12 when the *y* and *z* coordinates were varied respectively. The solid line continues to represent the 5th fiducial marker in each of these figures, and the dashdot line represents the expected value of overall $FRE^2$. The key for the lines corresponding to other fiducial markers are as follows. Figure 7: 1 and 3 are dotted; 2 and 4 are dashed. Figure 8: 1 and 2 are dotted; 3 and 4 are dashed. The equalities of these pairs of fiducials are because of their symmetric arrangements. We still observe a decrease in the expected value of $FRE^2$ for the 5th fiducial marker with increase in its distance, but for the other fiducial markers the change depends on their placements and the consequent variations of their distance square ratios. The expected value of the overall $FRE^2$ remained the same throughout in agreement with Sibson's result [55].

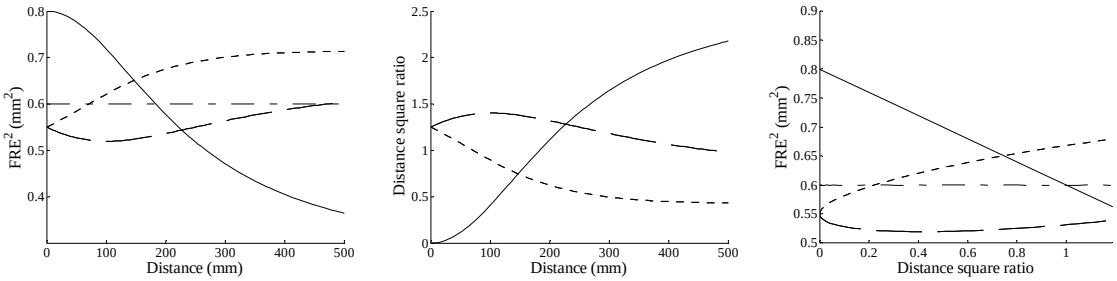


**(a)** **(b)** **(c)**

**Figure 13.** Effect of varying the fiducial marker arrangement by changing the distance of a fiducial marker along the *y* direction. (a) Plot of expected values of individual and overall $FRE^2$ with respect to change in distance. (b) Plot of variation of the distance square ratio with change in distance. (c) Plot of expected values of individual and overall $FRE^2$ with respect to change in the distance square ratio. The dotted line refers to fiducial markers 1 and 3. The dashed line refers to fiducial markers 2 and 4. The solid line refers to the 5th fiducial marker. The dashdot line refers to the expected values of overall $FRE^2$.

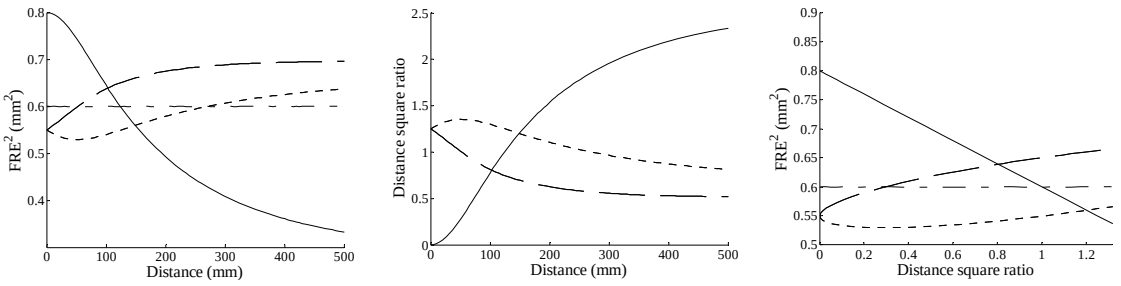


**(a)** **(b)** **(c)**

**Figure 14.** Effect of varying the fiducial marker arrangement by changing the distance of a fiducial marker along the *z* direction. (a) Plot of expected values of individual and overall mean $\mathrm{FRE}^2$ with respect to change in distance. (b) Plot of variation of the distance square ratio with change in distance. (c) Plot of expected values of individual and overall mean $\mathrm{FRE}^2$ with respect to change in the distance square ratio. The dotted line refers to fiducial markers 1 and 2. The dashed line refers to fiducial markers 3 and 4. The solid line refers to the 5$^{\text{th}}$ fiducial marker. The dashdot line refers to the expected values of overall $\mathrm{FRE}^2$.

## 7. Discussion

In this chapter we have shown that the approximate distribution for individual FRE that was derived in Chapter II works well for practical cases. We compared the predicted variances $\sigma_r^2$, $\sigma_v^2$, and $\sigma_w^2$ of the distribution of FRE components along the three orthogonal directions $\hat{\mathbf{r}}$, $\hat{\mathbf{v}}$, and $\hat{\mathbf{w}}$, respectively, with the variances that were obtained by simulations based on point-based registration algorithm that reflect typical situations, and found that they match very closely. Eq. (110) gives the distribution of $\mathrm{FRE}^2$ of a fiducial marker, which is the sum of three chi-square variables with variances $\sigma_r^2$, $\sigma_v^2$, and $\sigma_w^2$. We showed that this predicted distribution matches the results of simulation based on the point-based registration algorithm closely. We also verified that the method to compute the variance of FRE along any arbitrary direction is quite accurate. It is important to note though that the predicted distribution is just an approximation up to first order. They do not work so well for nearly-collinear fiducial configurations when RMS FLE is extremely high. Some examples of such extreme cases were shown. It is very rare though for those cases to occur in practice.

We also showed that the approximate formula to compute the magnitude of $FRE^2$ given by Eq. (111), matches the results of simulations based on point-based registration algorithm, and hence is confirmed as valid. This formula was derived in an earlier publication [56]. but had not heretofore been tested. This verification was performed to provide complete validation of FRE for a given fiducial marker. The formula is also a consequence of our distribution formula, and therefore, though not established explicitly by us here, it, like the predicted distribution, is expected to fail for extreme cases of linear configurations and large FLE.

Using Eq. (111) we have also examined the variation of the mean squared values of overall FRE and individual FRE with changes in *N*, with FLE, and with configuration. We found that, as expected from Sibson's early results [55], the overall FRE increases with increase in FLE and *N*. We find that the individual FRE also increases with FLE and *N*, in a similar to the overall FRE, as shown in Figure 9 and Figure 10. This similarity had not been established until now. The variation of overall FRE is simple to understand. It is a monotonic function of FLE and *N*. The variation of individual FRE with FLE is also simple, as is the variation with *N* when the overall shape of the configuration is not changed, but its dependence on shape is not simple as can be seen by plots in Figures 11-13. Because the shape of fiducial configurations vary with the shape of the object to which they are attached (e.g., the human head) and with the accessibility of that object (e.g., targets of resection affect where markers can be placed), it is important to take shape into account. Verification of formulas, such as those given by Eqs. (110) and (111), which simplify the calculation of expected FRE values is important to further the understanding of this variation.

The goal of any fiducial system is to register two spaces so as to produce the smallest possible TRE at the intended target regions. It has been a misconception to eliminate from registration the fiducial markers that have high individual FRE values, in order to improve the TRE [58-60]. This approach is based on the assumption that fiducial markers with high FRE are probably compromised. However, as can be seen from the simulations it is possible for

uncompromised fiducial markers to have considerably higher expected FRE values than those of other fiducial markers simply because of the difference in their positions. Thus, the value of individual FRE alone should not be a deciding factor to determine whether a fiducial marker is compromised or not. In the next chapter a possible solution is suggested to identify compromised fiducial markers based on the distribution of individual FRE.

# CHAPTER IV

## APPLICATION OF THE INDIVIDUAL FRE DISTRIBUTION

Rigid-body, point-based registration of fiducial markers is the basis for many image-guided surgical systems. It is a common practice to use bone-implanted fiducial markers or fiducial markers attached to some kind of rigid frame for highly critical cases. For less critical cases it might be possible to use skin-affixed markers. A radiographic image, such as CT or MR, is obtained with the fiducial markers attached to the patient, and the fiducial markers are localized in the image space. The locations of these fiducial markers are then obtained in physical space at the beginning of the procedure using commercially available tracking systems. The locations of all fiducial markers thus obtained from the image and physical space are used to register image space to physical space using a rigid-body, point-based registration algorithm [1]. This process defines the mapping between the two spaces.

It has been common practice to ignore a fiducial marker at position **r** if its measured individual fiducial registration, $\mathrm{FRE}(\mathbf{r})$, is high [58, 59, 60]. This practice is based on an assumption that a marker with high individual FRE is likely to have been compromised, and the further assumption that ignoring that fiducial will tend to reduce the target registration error (TRE). Both assumptions are reasonable when FRE is extremely high, but "extremely high" has never been quantified, and if the marker with high FRE has not been compromised, then ignoring that fiducial marker during the registration is unwarranted. By "compromised" we mean that the fiducial localization error of the marker is abnormally large because of poor localization technique or because the marker moved relative to the object to which it is attached during the time between localization in one space and localization in the other space, or a combination of

poor localization and movement. The assumption that high individual FRE implies that the marker is compromised ignores the fact that the expected size of individual FRE varies among the markers in the typical marker configuration—even in the absence of variation in FLE among them. Furthermore, while no proof exists, we will show below through examples based on simulations that ignoring an uncompromised fiducial marker from the registration appears always to increase the expected TRE.

The two key observations—that individual FRE varies among normally localized markers and that ignoring an uncompromised marker leads to a higher expected TRE—leads us to seek a method to determine whether a marker should, or should not, be ignored taking into account the variation of expected FRE. We present a possible method based on the distribution of individual FRE derived in Chapter II.

### 1. Effect on TRE of Removing Uncompromised Fiducial Markers

In this section we will see based on simulation the effect on TRE of removing uncompromised fiducial markers. Five different values are chosen for the number of fiducials, *N*, for this study: *N* = 4, 5, 10, 15, 20. A fiducial matrix *X* with *N* fiducial marker locations is generated by randomly choosing *N* three-dimensional locations with uniform distribution inside a cube of edge 200 mm. $\mathbf{x_i}$ is used to refer to the $i^{\text{th}}$ fiducial marker in *X*, $i = 1, 2, ..., N$. Let Ntars be the number of target positions at which TRE needs to be evaluated. The Ntars target locations are also generated randomly with uniform distribution inside the cube of edge 200 mm. $\mathbf{tar_i}$ refers to the $i^{\text{th}}$ target location, $i = 1, 2, ..., \text{Ntars}$. A simulation is performed using the point-based registration algorithm to study the effect of removing uncompromised fiducial markers on TRE. The steps involved in the simulations are explained below.

1. Generate *Y*: *Y* is the perturbed set of fiducial marker locations which needs to be registered to *X*. Each fiducial marker's location in *X* is perturbed along the *x*, *y*, and *z* directions using normally distributed random variables with zero mean and variance $\sigma^2$ to obtain the corresponding fiducial marker location in *Y*. $\mathbf{y}_i$ refers to the $i^{th}$ fiducial marker in *Y*, $i = 1, 2, ..., N$ .
2. Register *X* to *Y*: Point-based registration is performed using the algorithm described in [1] to get the rotation matrix *R* and translation vector **t** by minimizing the total FRE$^2$ so that for all fiducials $i = 1, 2, ..., N$ , $\mathbf{y}_i \approx R\mathbf{x}_i + \mathbf{t}$ .
3. Compute registration errors:
    a. Individual FRE: Calculate the distance between corresponding fiducial markers after registration to get the individual FRE, i.e.,
    $$\mathrm{FRE}(\mathbf{x}_i) = \left| R\mathbf{x}_i + \mathbf{t} - \mathbf{y}_i \right|. \tag{121}$$
    b. Overall measured RMS FRE ($\mathrm{FRE}_M$): $\mathrm{FRE}_M$ is defined as the square root of the measured sum of squares of all the individual FREs.
    c. TRE: The target registration error is computed similarly to the individual FREs as follows:
    $$\mathrm{TRE}(\mathbf{tar}_i) = \left| R\mathbf{tar}_i + \mathbf{t} - \mathbf{tar}_i \right|. \tag{122}$$
4. Remove a fiducial marker: The fiducial marker with the highest individual FRE is chosen, and, if its individual FRE is above a certain threshold, it is removed from the fiducial set for registration. New point sets, newX and newY, are obtained by removing this marker from the original *X* and *Y*.
5. Steps 2 and 3 are repeated with newX and newY, and a new set of registration errors are obtained.
6. Compute the changes in $\mathrm{FRE}_M$ and individual TRE resulting from dropping a marker.

7. Steps 1 through 6 are repeated for a total of $\mathcal{M}_3$[1] times.
8. Compute mean changes for $FRE_M$ and TRE: The mean changes are computed in two different ways:

a. Type1 mean = sum of all the changes divided by $\mathcal{M}_3$.

b. Type2 mean = sum of all the changes divided by the number of times a fiducial marker was removed. (Note that the change will be zero if no fiducial marker is removed. Note also that since the number of times a marker is removed must be less than or equal to $\mathcal{M}_3$, the Type2 mean must be greater than or equal to the Type 1 mean.)

Ten targets (ntars = 10) were chosen for analyzing the TRE changes. The simulation was performed for ten different sets of fiducial markers, each represented by a fiducial matrix *X*, for each value of *N*. $\mathcal{M}_3$ = 10,000 was used for the simulations. The RMS FLE was set to 1 mm for all cases. Though, as mentioned above, no standard is known for defining a high individual FRE, we set these five reasonable thresholds:

1. Threshold = 0: The fiducial marker with the highest individual FRE is removed irrespective of its value. (The Type1 and Type2 means are the same for this case.)
2. Threshold = 1: The fiducial marker with the highest individual FRE is removed if the corresponding individual FRE is greater than 1 mm.
3. Threshold = 1.5*$FRE_M$: The fiducial marker with the highest individual FRE is removed if the corresponding individual FRE is greater than 1.5 times the measured overall FRE.
4. Threshold = $1.5 * \langle \mathrm{FRE} \rangle$: The fiducial marker with the highest individual FRE is removed if the corresponding individual FRE is greater than 1.5 times the

[1] The numbering is continued from the previous chapter.

expected value of overall FRE. We can compute the expected value of overall FRE using Sibson's result [55] as follows:

$$\left\langle \mathrm{FRE}^2 \right\rangle = (1 - 2/N)\left\langle \mathrm{FLE}^2 \right\rangle, \tag{123}$$

where $\left\langle \mathrm{FLE}^2 \right\rangle = 1$ for our case.

5. Threshold for $i^{\text{th}}$ fiducial marker = $1.5 * \left\langle \mathrm{FRE}(\mathbf{x}_i) \right\rangle$: The fiducial marker with the highest individual FRE is removed if the corresponding individual FRE is greater than 1.5 times the expected value of the individual FRE for that fiducial marker. The expected value of the individual FRE at $\mathbf{x}_i$ is given by [56] and also in [Chapter II of this dissertation]:

$$\left\langle \mathrm{FRE}^2(\mathbf{x}_i) \right\rangle = \left\langle \mathrm{FLE}^2 \right\rangle \left[ \left( \frac{N-1}{N} \right) - \frac{1}{3} \sum_{i=1}^{3} \frac{d_i^2}{f_i^2} \right], \tag{124}$$

where $d_i^2$ is the squared distance of the fiducial marker $\mathbf{x}_i$ from the principal axis *i*, and $f_i^2$ is the sum of squared distances of all the fiducial points from the principal axis *i*.

The fourth and fifth thresholds are practical only if we know the $\left\langle \mathrm{FLE}^2 \right\rangle$ for the given system.

Table 6 and Table 7 report, for each value of *N*, the Type1 and Type2 mean changes, respectively, in $\mathrm{FRE_M}$ and RMS TRE observed over all these ten sets of fiducial markers for all the thresholds used. The Type1 and Type2 mean percentage changes are identical when the threshold on the maximum individual FRE for removing a fiducial marker is set to zero. (We planned to ignore the remote possibility of more than one fiducial marker having the same highest individual FRE, but it did not happen in our test cases.)

We see that FRE improves when a fiducial marker is removed from the system. This is an expected result according to Eq. (123). We observed the expected opposite effect in TRE: TRE tended to increase when we removed a fiducial marker. The effect is especially severe when the

number of fiducial markers is small. Even though FRE tends to be smaller with fewer fiducial markers, TRE tends to be larger, and TRE defines the accuracy for a fiducial system. This effect was observed for all thresholds. We see a big difference in the Type1 and Type2 means for lower values of *N*. This is because of the fact that, while fewer markers tend to be selected for removal based on the threshold, when a marker is removed the effect is more severe.

**Table 6.** Type1 mean change as a percentage of mean values for FRE and TRE.

| *N* | Threshold = 0 | | Threshold = 1 | | Threshold = $1.5*\text{FRE}_\text{M}$ | | Threshold = $1.5*\langle\text{FRE}\rangle$ | | Threshold for $\mathbf{x}_i$ = $1.5*\langle\text{FRE}(\mathbf{x}_i)\rangle$ | |
|---|---|---|---|---|---|---|---|---|---|---|
| | FRE | TRE | FRE | TRE | FRE | TRE | FRE | TRE | FRE | TRE |
| 4 | -45 | 265 | -23 | 117 | -10 | 22 | -19 | 96 | -17 | 136 |
| 5 | -30 | 61 | -21 | 39 | -11 | 13 | -14 | 25 | -13 | 37 |
| 10 | -13 | 14 | -12 | 14 | -9 | 9 | -8 | 9 | -8 | 9 |
| 15 | -8 | 10 | -8 | 10 | -7 | 9 | -7 | 8 | -7 | 8 |
| 20 | -6 | 8 | -6 | 8 | -6 | 7 | -6 | 7 | -6 | 7 |

**Table 7.** Type 2 mean change as a percentage of mean values for FRE and TRE.

| *N* | Threshold = 0 | | Threshold = 1 | | Threshold = $1.5*\text{FRE}_\text{M}$ | | Threshold = $1.5*\langle\text{FRE}\rangle$ | | Threshold for $\mathbf{x}_i$ = $1.5*\langle\text{FRE}(\mathbf{x}_i)\rangle$ | |
|---|---|---|---|---|---|---|---|---|---|---|
| | FRE | TRE | FRE | TRE | FRE | TRE | FRE | TRE | FRE | TRE |
| 4 | -45 | 265 | -62 | 319 | -64 | 139 | -65 | 324 | -66 | 521 |
| 5 | -30 | 61 | -37 | 71 | -43 | 48 | -42 | 75 | -43 | 120 |
| 10 | -13 | 14 | -13 | 14 | -15 | 15 | -15 | 17 | -16 | 17 |
| 15 | -8 | 10 | -8 | 10 | -9 | 11 | -10 | 12 | -10 | 12 |
| 20 | -6 | 8 | -6 | 8 | -7 | 8 | -7 | 9 | -7 | 9 |

All the increases in TRE observed by this study can be explained based on Chapter II and Chapter III. Based on the distribution derived in Chapter II for individual $FRE^2$ of a fiducial marker, we see that it is possible for certain uncompromised fiducial markers to have very high individual FRE. We also saw in Chapter III through simulations that certain fiducial markers have higher expected individual FREs than others, depending on the fiducial configuration. Thus when we suspect that a fiducial marker in the fiducial system is compromised, it is important to find out whether the chosen fiducial marker is actually compromised or not. We propose an algorithm in this chapter as a start towards solving the problem of identifying compromised fiducial markers in a given fiducial system. The method is based on the distribution of individual FRE components derived in Chapter II of this dissertation.

## 2. An Algorithm for Finding the Compromised Fiducial Marker

As we saw from the results in Table 6 and Table 7 it becomes imperative to estimate whether a fiducial marker is compromised or not. We will apply the information obtained from the distribution of individual FRE of a given fiducial marker for this purpose. The assumption made here is that we know the overall variance of FLE, $\langle \mathrm{FLE}^2 \rangle$ expected for that particular system from previous estimation. Then $\sigma^2 = \langle \mathrm{FLE}^2 \rangle / 3$ is the variance along the *x*, *y*, and *z* directions. This assumption is same as the one we made while setting the fourth and fifth thresholds in the previous section.

Suppose we have two sets of *N* corresponding fiducial markers—*X* and *Y*. After performing rigid-body point-based registration, the individual FRE of each fiducial marker in the *x*, *y*, and *z* directions can be measured as follows:

$$\mathbf{FRE}(\mathbf{x_i}) = R\mathbf{x_i} + \mathbf{t} - \mathbf{y_i}, \tag{125}$$

where $\mathbf{x_i}$ and $\mathbf{y_i}$ are the corresponding $i^{\text{th}}$ fiducial markers in *X* and *Y*, respectively, $i = 1, 2, ..., N$, and *R* and **t** are the resultant rotation matrix and translation vector after performing the

registration. Thus for a given fiducial marker **r**, we can measure its FRE error in the three orthogonal directions $\hat{\mathbf{r}}$, $\hat{\mathbf{v}}$, and $\hat{\mathbf{w}}$ which are chosen as described in Chapter II. Let us call these three FRE components $\text{FREmeasured}_k(\mathbf{r})$, $k=1,2,3$ for $\hat{\mathbf{r}}$, $\hat{\mathbf{v}}$, and $\hat{\mathbf{w}}$ directions respectively.

Based on the derivations in Chapter II, we know that the FRE of a fiducial marker located at **r** can be resolved into three orthogonal components along the directions $\hat{\mathbf{r}}$, $\hat{\mathbf{v}}$, and $\hat{\mathbf{w}}$ such that the three components are independent, zero mean normal distributions with variances $\sigma_r^2$, $\sigma_v^2$, and $\sigma_w^2$ which are given by

$$\sigma_r^2 = \sigma^2\left(\frac{N-1}{N}\right), \tag{126}$$

$$\sigma_v^2 = \sigma^2\left(\frac{N-1}{N}\right) - r^2\omega_w^2, \tag{127}$$

$$\sigma_w^2 = \sigma^2\left(\frac{N-1}{N}\right) - r^2\omega_v^2, \tag{128}$$

where $r$ is the magnitude of the vector **r**, $\omega_v^2 = \sigma^2\sum_{i=1}^{3}\frac{\hat{v}_i^2}{\Lambda_{aa}^2+\Lambda_{bb}^2}$, $\omega_w^2 = \sigma^2\sum_{i=1}^{3}\frac{\hat{w}_i^2}{\Lambda_{aa}^2+\Lambda_{bb}^2}$, $\{i,a,b\} = \{1,2,3\}$, $\{2,3,1\}$, or $\{3,1,2\}$, and $[\Lambda_{11} \quad \Lambda_{22} \quad \Lambda_{33}]$ are the singular values of the demeaned version of *X*. Thus it is possible to find the distribution of individual FRE along the corresponding $\hat{\mathbf{r}}$, $\hat{\mathbf{v}}$, and $\hat{\mathbf{w}}$ directions for every fiducial marker. Figure 15 shows an example distribution. The distribution of the magnitude is half-bell shaped (Figure 15(a)), while the distribution of the signed quantity is bell shaped (Figure 15(b)) and centered at zero. We have three distributions such as the ones shown in Figure 15, but with differing spreads, for the $\hat{\mathbf{r}}$, $\hat{\mathbf{v}}$, and $\hat{\mathbf{w}}$ directions for each fiducial marker. Based on these distributions and the measured error for each fiducial marker, we can construct an algorithm to estimate whether a fiducial marker is compromised or not.


**Figure 15.** Example of the distribution of individual FRE along a direction *k* for a fiducial marker. (a) The distribution of the magnitude of FRE is half-bell curve. (b) The distribution of the signed quantity is a full bell curve.

We begin by letting $P_r$, $P_v$, and $P_w$ represent the probabilities of observing an individual FRE for a given marker with a magnitude less than $\text{FREmeasured}_r(\mathbf{r})$, $\text{FREmeasured}_v(\mathbf{r})$, and $\text{FREmeasured}_w(\mathbf{r})$ along of the $\hat{\mathbf{r}}$, $\hat{\mathbf{v}}$, and $\hat{\mathbf{w}}$ directions respectively for a fiducial marker **r**. These probabilities refer to the area to the left of the line in Figure 15(a) and between the two lines in Figure 15(b). The value of this probability in a given direction gives us an idea of how large the measured FRE is in that direction relative to what is expected. A high the value of this probability implies that FRE is likely to be lower than the measured value in that direction, raising the suspicion that the marker is compromised. For a given registration, we can calculate these three probabilities for each fiducial marker. By setting a threshold for the probability we would like to observe, we can declare that the fiducial marker that has the highest probability value and whose value is greater than the threshold in any direction is a possibly compromised fiducial marker. In the unlikely event that more than one fiducial marker is selected on this basis, then we choose among them the fiducial marker that has the highest value of the product $P_r P_v P_w$. This product tells us the probability of observing relatively high FRE values simultaneously in all the three directions. Figure 16 can be used to explain the product of probabilities using Venn

diagram representation. There are three circles in the Venn diagram each to represent $P_r$, $P_v$, and $P_w$. The product $P_r P_v P_w$ is the probability of being in the common region shared by all the three circles at the center.

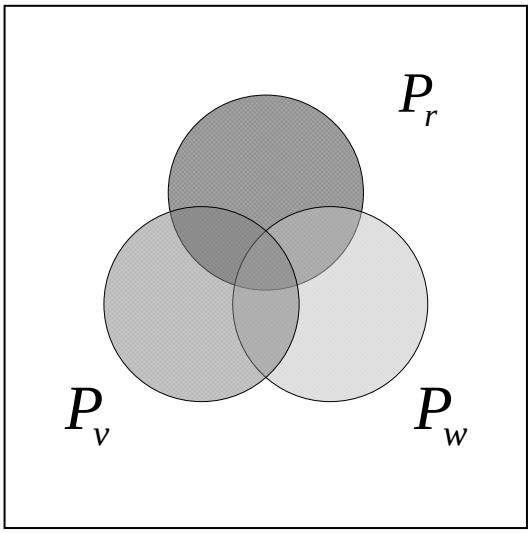


**Figure 16.** Venn diagram to explain the product $P_r P_v P_w$. Each of these circles represent $P_r$, $P_v$, or $P_w$. The product $P_r P_v P_w$ is the area that is common to all the three circles.

Given *X* and *Y*, our algorithm for finding the possible compromised fiducial marker is as follows:

1. Register *X* and *Y*: Perform point-based registration [1] between *X* and *Y* to get the rotation matrix *R* and translation vector **t**.
2. Measure individual FREs: The individual FRE values for each fiducial marker in *x*, *y*, and *z* directions are measured. If $\mathbf{new\_y_i} = R\mathbf{x_i} + \mathbf{t}$, then

$$\mathrm{FREmeasured}_x\left(\mathbf{x_i}\right) = \mathrm{new\_y}_{ix} - y_{ix}, \tag{129}$$

$$\mathrm{FREmeasured}_y\left(\mathbf{x_i}\right) = \mathrm{new\_y}_{iy} - y_{iy}, \tag{130}$$

$$\mathrm{FREmeasured}_z\left(\mathbf{x_i}\right) = \mathrm{new\_y}_{iz} - y_{iz}. \tag{131}$$

The values of $\text{FREmeasured}_x(\mathbf{x_i})$, $\text{FREmeasured}_y(\mathbf{x_i})$, and $\text{FREmeasured}_z(\mathbf{x_i})$ are used to find the error components for the $i^{\text{th}}$ fiducial marker along the three orthogonal directions $\hat{\mathbf{r}}$, $\hat{\mathbf{v}}$, and $\hat{\mathbf{w}}$, which we will call $\text{FREmeasured}_r(\mathbf{x_i})$, $\text{FREmeasured}_v(\mathbf{x_i})$, and $\text{FREmeasured}_w(\mathbf{x_i})$ respectively. These three components are computed for all fiducial markers.

3. Compute $P_r$, $P_v$, and $P_w$: The probabilities $P_r$, $P_v$, and $P_w$ for a fiducial marker $\mathbf{r}$ are computed as the area between $-\text{FREmeasured}_r(\mathbf{r})$ and $\text{FREmeasured}_r(\mathbf{r})$ under the normal curve $\mathcal{N}(0,\sigma_r)$, the area between $-\text{FREmeasured}_v(\mathbf{r})$ and $\text{FREmeasured}_v(\mathbf{r})$ under the normal curve $\mathcal{N}(0,\sigma_v)$, and the area between $-\text{FREmeasured}_w(\mathbf{r})$ and $\text{FREmeasured}_w(\mathbf{r})$ under the normal curve $\mathcal{N}(0,\sigma_w)$, respectively. These probabilities are computed for each fiducial marker based on the individual FRE values measured in the previous step along the $\hat{\mathbf{r}}$, $\hat{\mathbf{v}}$, and $\hat{\mathbf{w}}$ directions.
4. Find the possible compromised fiducial marker: We will have 3*N* probability values as a result of the previous step. We find the fiducial marker that has the maximum probability value among all these 3*N* values. If it is above a certain probability threshold, then it is a possible compromised fiducial marker. (Note that we can never say with 100% confidence that a fiducial marker is compromised without any prior information. Based on the threshold set, there is still a chance that we will declare a fiducial marker to be compromised when it is actually not). If no fiducial markers are selected, then there is possibly no compromised fiducial marker in the system. When more than one fiducial markers are selected, then we choose the one with the maximum value for the product $P_r P_v P_w$.

### 3. Simulations to Test the Algorithm for Finding the Compromised Fiducial Marker

We performed simulations to test the algorithm suggested in the previous section and to compare it to the simple class of methods in which all FREs within a given registration are compared to a common FRE threshold. If an FRE exceeds the threshold, the marker is labeled as compromised. We will call such methods "common-threshold" methods.

The same five values were chosen for the $N$ for this test: $N$ = 4, 5, 10, 15, 20. The fiducial matrix $X$ is obtained by generating $N$ fiducial markers randomly with uniform distribution inside a cube of 200 mm. $\mathbf{x_i}$ is used to refer to the $i^{\text{th}}$ fiducial marker in $X$, $i = 1, 2, ..., N$. One of the fiducial markers is purposefully compromised by adding error to its $z$-component. Since $X$ is generated randomly, the direction of the error we add is random relative to the principle axes of the marker configuration, despite the fact that it is always in the $z$ direction. A simulation is performed to compare the performance of our method to find compromised fiducial markers with that of methods based on a common threshold for the measured individual FRE values. The simulation is as follows:

1. Compute the predicted variances: The predicted variances $\sigma_r^2$, $\sigma_v^2$, and $\sigma_w^2$ are computed for the given $X$ for each fiducial marker along its respective $\hat{\mathbf{r}}$, $\hat{\mathbf{v}}$, and $\hat{\mathbf{w}}$ directions using Eqs. (126), (127), and (128) respectively.
2. Generate $Y$: Each fiducial marker's location in $X$ is perturbed along the $x$, $y$, and $z$ directions using normally distributed random variables with zero mean and variance $\sigma^2$ to obtain the corresponding fiducial marker location in $Y$. $\mathbf{y_i}$ refers to the $i^{\text{th}}$ fiducial marker in $Y$, $i = 1, 2, ..., N$.
3. Compromise a fiducial marker: The fiducial marker $m$ is compromised by adding error $e$ to its $z$-component as follows:

$$y_{m,z} = y_{m,z} + e. \tag{132}$$

This step is performed randomly such that the percentage chance of having a compromised fiducial marker is *C*.

4. Register *X* and *Y*: Perform point-based registration [1] between *X* and *Y* to get the rotation matrix *R* and translation vector **t**.
5. Measure individual FREs and overall RMS FRE: The FRE components $\text{FREmeasured}_x(\mathbf{x_i})$, $\text{FREmeasured}_y(\mathbf{x_i})$, $\text{FREmeasured}_z(\mathbf{x_i})$, $\text{FREmeasured}_r(\mathbf{x_i})$, $\text{FREmeasured}_v(\mathbf{x_i})$, and $\text{FREmeasured}_w(\mathbf{x_i})$ are computed for each fiducial marker as described in the algorithm in section 2. The individual FRE value at each fiducial marker is calculated as the square root of the sum of the squares of the FRE measured in the *x*, *y*, and *z* directions. The overall RMS FRE, $\text{FRE}_\text{M}$, is also computed.
6. Find a possible compromised fiducial marker using a common threshold: This is similar to the method explained in the first section of this chapter. The compromised fiducial marker is chosen to be the one with the maximum individual FRE among all fiducials whose individual FREs are greater than a threshold. Different thresholds used are
   a. T1 = $m_1$ (a constant value),
   b. T2 = $m_2 * \text{FRE}_\text{M}$,
   c. T3 = $m_3 * \langle \text{FRE} \rangle$,
   d. T4 = $m_4 * \langle \text{FRE}(\mathbf{x}_i) \rangle$.
7. Apply our new algorithm to find the possible compromised fiducial marker based on the expected distribution of the individual FRE: Execute steps 3 and 4 of the algorithm to find the possible compromised fiducial marker described in the previous section using a probability threshold T5. (Note that steps 1 and 2 of the algorithm described in the previous section are performed in Steps 4 and 5 of this simulation.)

8. Repeat steps 2 through 7 $\mathcal{M}_4$ times.

9. Compute elimination percentages: The percentage of times the correct fiducial marker *m* as compromised (true positive) was identified is computed for each method. Also the percentage of times an uncompromised fiducial marker was labeled as compromised (false positive) is computed for each method.

The simulation was performed for 10 different sets of *X* for each value of *N*. RMS FLE = 0.5 mm and 1 mm were used for the simulations. For each set *X*, the simulation was repeated for every possible fiducial marker *m* in that set. Thus 10**N* simulations were performed for a given *N* and RMS FLE. The value of *e* was chosen to be 5 mm. $\mathcal{M}_4$ = 1000 was used for the simulations. *C* was chosen to be 1%, i.e., a fiducial marker is intentionally compromised only 1% of the times. The thresholds T1, T2, T3, and T4 were obtained by using the values 1.5 and 2 for the threshold factors, $m_1$, $m_2$, $m_3$, and $m_4$, respectively. The threshold T5 was chosen such that the chance of choosing an uncompromised fiducial marker based on the probability value in one direction equals a desired false-positive rate, $m_5$. An approximate formula is $\mathrm{T5} = \left(1 - m_5\right)^{1/(3N)}$, but for $m_5 \leq 0.01$ we can further approximate it as follows:

$$\mathrm{T5} = 1 - \frac{m_5}{3N}. \tag{133}$$

For this set of simulations we chose the desired false-positive rate $m_5$ equal {1%, 0. 5%, 0. 1%}.

Table 8 and Table 9 report the results of the simulations. For each value of *N* and RMS FLE, Table 8 gives the mean and standard deviation of the chance of finding the compromised fiducial marker if it is present, which is the true-positive rate. The mean and standard deviation are computed based on the 10**N* simulations conducted for each value of *N* and each value of RMS FLE. *C* = 1% was used, and hence we would expect a true-positive value of 0.010 when all the compromised markers are found.

**Table 8.** Mean and standard deviation of the true-positive rate (percentage) for the four common-threshold methods and our new algorithm, for given values of threshold factors, FLEs and *Ns*.

| RMS FLE | | 0.50 | | | | | 1.0 | | | | |
|---|---|---|---|---|---|---|---|---|---|---|---|
| *N* | | 4 | 5 | 10 | 15 | 20 | 4 | 5 | 10 | 15 | 20 |
| Threshold parameters | | | | | | | | | | | |
| $m_1$ | 1.5 | 97 ± 4.4 | 98 ± 3.9 | 100 ± 0 | 100 ± 0 | 100 ± 0 | 93 ± 5.0 | 96.8 ± 3.8 | 100 ± 0 | 100 ± 0 | 100 ± 0 |
| | 2 | 91 ± 4.8 | 96 ± 5.0 | 100 ± 0 | 100 ± 0 | 100 ± 0 | 89 ± 4.1 | 92.8 ± 4.1 | 100 ± 0 | 100 ± 0 | 100 ± 0 |
| $m_2$ | 1.5 | 76 ± 10.7 | 93 ± 7.2 | 100 ± 0 | 100 ± 0 | 100 ± 0 | 63 ± 10.8 | 85.2 ± 6.7 | 100 ± 0 | 100 ± 0 | 100 ± 0 |
| | 2 | 0 ± 0 | 0 ± 0 | 100 ± 0 | 100 ± 0 | 100 ± 0 | 0 ± 0 | 0 ± 0 | 99.4 ± 0.5 | 100 ± 0 | 100 ± 0 |
| $m_3$ | 1.5 | 97 ± 4.4 | 98 ± 4.0 | 100 ± 0 | 100 ± 0 | 100 ± 0 | 94 ± 5.2 | 96.8 ± 3.8 | 100 ± 0 | 100 ± 0 | 100 ± 0 |
| | 2 | 97 ± 4.4 | 98 ± 4.0 | 100 ± 0 | 100 ± 0 | 100 ± 0 | 94 ± 5.0 | 96.8 ± 3.8 | 100 ± 0 | 100 ± 0 | 100 ± 0 |
| $m_4$ | 1.5 | 97 ± 4.4 | 98 ± 4.0 | 100 ± 0 | 100 ± 0 | 100 ± 0 | 94 ± 5.2 | 96.8 ± 3.8 | 100 ± 0 | 100 ± 0 | 100 ± 0 |
| | 2 | 97 ± 4.4 | 98 ± 4.0 | 100 ± 0 | 100 ± 0 | 100 ± 0 | 94 ± 5.2 | 96.8 ± 3.8 | 100 ± 0 | 100 ± 0 | 100 ± 0 |
| $m_5$ | 1% | 73 ± 8.1 | 82 ± 9.2 | 100 ± 0 | 100 ± 0 | 100 ± 0 | 70 ± 10.5 | 82.6 ± 6.9 | 99.7 ± 0.5 | 100 ± 0 | 99.9 ± 0.3 |
| | 0. 5% | 73 ± 8.1 | 82 ± 9.2 | 100 ± 0 | 100 ± 0 | 100 ± 0 | 69 ± 10.6 | 82.4 ± 6.8 | 99.7 ± 0.5 | 99.9 ± 0.3 | 99.6 ± 0.5 |
| | 0. 1% | 73 ± 8.1 | 82 ± 9.2 | 100 ± 0 | 100 ± 0 | 100 ± 0 | 67 ± 11.3 | 78.8 ± 6.8 | 98.1 ± 1.1 | 99.1 ± 0.7 | 99.0 ± 1.1 |

**Table 9.** Mean and standard deviation of the false-positive rate (percentage) for the four common-threshold methods and our new algorithm, for given values of threshold factors, FLEs and *Ns*.

| RMS FLE | | 0.50 | | | | | 1.0 | | | | |
|---|---|---|---|---|---|---|---|---|---|---|---|
| *N* | | 4 | 5 | 10 | 15 | 20 | 4 | 5 | 10 | 15 | 20 |
| Threshold parameters | | | | | | | | | | | |
| $m_1$ | 1.5 | 0 ± 0 | 0 ± 0 | 0 ± 0 | 0.001 ± 0.003 | 0.005 ± 0.01 | 3 ± 0.06 | 7 ± 0.20 | 31 ± 0.64 | 53 ± 0.52 | 68 ± 0.44 |
| | 2 | 0 ± 0 | 0 ± 0 | 0 ± 0 | 0 ± 0 | 0 ± 0 | 0.07 ± 0.03 | 0.26 ± 0.03 | 2 ± 0.13 | 5 ± 0.20 | 8 ± 0.30 |
| $m_2$ | 1.5 | 14 ± 0.26 | 28 ± 0.29 | 62 ± 0.43 | 80 ± 0.41 | 90 ± 0.26 | 14 ± 0.29 | 28 ± 0.30 | 62 ± 0.44 | 80 ± 0.41 | 90 ± 0.26 |
| | 2 | 0 ± 0 | 0 ± 0 | 2 ± 0.18 | 6 ± 0.21 | 10 ± 0.30 | 0 ± 0 | 0 ± 0 | 2 ± 0.18 | 6 ± 0.22 | 10 ± 0.30 |
| $m_3$ | 1.5 | 28 ± 0.29 | 34 ± 0.44 | 55 ± 0.47 | 70 ± 0.38 | 80 ± 0.39 | 28 ± 0.30 | 34 ± 0.45 | 55 ± 0.46 | 70 ± 0.39 | 80 ± 0.39 |
| | 2 | 5 ± 0.08 | 5 ± 0.25 | 7 ± 0.38 | 11 ± 0.30 | 14 ± 0.39 | 5 ± 0.08 | 5 ± 0.24 | 7 ± 0.38 | 11 ± 0.30 | 14 ± 0.39 |
| $m_4$ | 1.5 | 26 ± 0.09 | 31 ± 0.39 | 54 ± 0.51 | 70 ± 0.41 | 80 ± 0.36 | 26 ± 0.09 | 31 ± 0.39 | 54 ± 0.51 | 70 ± 0.42 | 80 ± 0.36 |
| | 2 | 5 ± 0.13 | 5 ± 0.16 | 7 ± 0.36 | 11 ± 0.29 | 14 ± 0.37 | 5 ± 0.14 | 5 ± 0.18 | 7 ± 0.36 | 11 ± 0.29 | 14 ± 0.37 |
| $m_5$ | 1% | 0.74 ± 0.07 | 0.93 ± 0.07 | 0.95 ± 0.09 | 0.97 ± 0.08 | 0.99 ± 0.11 | 0.81 ± 0.08 | 0.94 ± 0.07 | 0.95 ± 0.09 | 0.97 ± 0.08 | 0.99 ± 0.11 |
| | 0. 5% | 0.40 ± 0.05 | 0.47 ± 0.06 | 0.48 ± 0.07 | 0.50 ± 0.08 | 0.49 ± 0.07 | 0.45 ± 0.03 | 0.46 ± 0.06 | 0.48 ± 0.07 | 0.50 ± 0.08 | 0.49 ± 0.07 |
| | 0. 1% | 0.07 ± 0.02 | 0.09 ± 0.03 | 0.09 ± 0.03 | 0.10 ± 0.03 | 0.09 ± 0.03 | 0.09 ± 0.02 | 0.09 ± 0.03 | 0.09 ± 0.03 | 0.10 ± 0.03 | 0.09 ± 0.03 |

From the tables we can analyze and understand the results of each method. We look first at the four common-threshold methods, beginning with the T1 threshold. When the T1 threshold is used, it can be seen from Table 8 that the threshold factor $m_1 = 1.5$ provides a high true-positive rate, meaning that it works well in correctly labeling compromised markers, for cases when $N$ is 10, 15, or 20. When $N$ is 4 or 5, the true-positive rate is lower than 100% meaning that sometimes the compromised markers are not identified. The rate is higher when FLE is 0.5 mm than when it is 1 mm. From Table **9** it can be seen that the false-positive rate for $m_1 = 1.5$, meaning its rate of mislabeling uncompromised markers, is for all $N$ zero or very close to zero when FLE = 0.5 mm. However, the false-positive rate for $m_1 = 1.5$ becomes large when FLE = 1 mm. The increase in the false-positive rate with an increase in FLE is to be expected because individual FREs tend to have higher values when FLE is higher. The threshold is large enough for FLE = 0.5 mm, to keep all uncompromised markers from meeting the compromised-marker criterion (i.e., no false positives), but it is too small to avoid false positives at FLE = 1 mm. We can reduce the false-positive rate for T1 by increasing the threshold factor to $m_1 = 2$ mm as shown in Table **9**, but, as $N$ increases the false-positive rate again rises, not as much at this threshold, but still well above 1% for large $N$. Similar results are seen when the T2 threshold is used with the same factors $m_2 =$ 1.5 and 2. There are important differences, however. First, for $m_2 = 2$ the true-positive rate is zero for $N = 4$ and 5 (Table 8). Second, for $m_2 = 1.5$ the true-positive rate for $N = 4$ and 5 is lower than the T1 threshold, and also all false-positive rates are considerably higher than for the T1 threshold. Third, the false-positive rates are independent of FLE. This independence results from the fact that the T2 threshold is proportional to the measured FRE, which tends to be proportional to FLE. The false-positive rates are similarly independent of FLE for the T3 and T4 thresholds for the same reason. Results for T3 and T4 thresholds are similar for all cases. With the T3 and T4 thresholds, we see that the true-positive rates are good when $N$ is large (as also obesrved with T1 and T2), but the false-positive rates are high with the effect on the false-positive rate increasing as usual with increasing $N$. Still higher values for $m_3$ and $m_4$ will result in lower false-positive rates,

but they will reduce the true-positive rates. In summary the T1 threshold seems to work best, but all of the common-threshold methods suffer from inconsistencies in false-positive rates with change in FLE and/or in $N$. All the common-threshold methods also have trouble finding compromised markers when $N$ is small.

Our algorithm seems to work consistently well for all cases when $N$ is large but has difficulty with lower true-positive rates when $N$ is small. The compromised markers are almost always found when $N$ is 10, 15, or 20. An interesting result to note from Table 9 is the fact that the false-positive rate for all the cases is very close to $m_5$, which is the false-positive rate desired. This shows that once we set the value for $m_5$, using Eq. (133), it works for any fiducial configuration and FLE. The threshold can be lowered for small $N$ in order to improve the true-positive rate, but lowering the threshold will increase the false-positive rate.

Thus we see that the T1 method with $m_1$ = 1.5 or 2.0 works well for small $N$, while our new algorithm works well for large $N$. For any of these methods, the choice of threshold plays an important role in determining the true-positive and false-positive rate. We would like the false-positive rate to be as low as possible, i.e., we want fewer uncompromised fiducial markers to be erroneously labeled as compromised. We want to avoid this type of mislabeling because we want to avoid removing an uncompromised marker, and we want to avoid removing it because we saw earlier in this chapter that removing an uncompromised fiducial marker tends to decrease the accuracy of the system. The false-positive rate is decreased by setting the threshold to a higher value, but this increase in threshold at the same time may also decrease the true-positive rate. We saw from the results of our simulations of the common-threshold methods that different values of $m_1$, $m_2$, $m_3$, and $m_4$ yield different false-positive rates.

It is important to note that the effect on the false-positive rate of the threshold used in any of the common-threshold methods depends on the marker configuration, including the number of markers, and for the T1 method, which performed the best among the common-threshold methods, it depends on FLE as well. Thus, there is no specific value for $m_1$, $m_2$, $m_3$, or $m_4$ that will put the

false-positive rate at a desired level for all configurations. On the contrary with our proposed algorithm one value of $m_5$ is sufficient to set the false-positive rate for all marker configurations, all numbers of markers, and all values of FLE, as is evidenced by the results in Table 9. Thus, a distinct advantage of our new algorithm is that its threshold value can be set once and for all using Eq. (133) (or using the more precise formula given just above that equation), and it will remain valid always. The threshold has a simple dependence on N, given by that equation and is independent of the FLE.

## 4. Decision to Remove a Compromised Fiducial Marker

We presented in the previous section an algorithm to find a compromised fiducial marker, if any, in a fiducial system. The question now is—"Should we (a) remove the compromised fiducial marker and reregister, or (b) abandon the registration entirely?"

The effect of removing the compromised marker on TRE at a target location **r** can be determined using the expression for TRE [56] :

$$\left\langle \mathrm{TRE}^2(\mathbf{r}) \right\rangle = \left\langle \mathrm{FLE}^2 \right\rangle \left( \frac{1}{N} + \frac{1}{3} \sum_{i=1}^{3} \frac{d_i^2}{f_i^2} \right) \tag{134}$$

where $\langle \mathrm{FLE} \rangle$ is the expected fiducial localization error, $N$ is the number of fiducials used in the registration, $d_i^2$ is the squared distance of the target **r** from the principal axis $i$, and $f_i^2$ is the sum of squared distances of all the fiducial points from the principal axis $i$. The above expression can be used to estimate TRE when all the markers are used and when all the markers except the compromised marker are used. Removing a compromised marker from the calculation in Eq. (134) will always result in an increased expected TRE. If the increased TRE remains at an acceptable level, which will depend on the particular application, then we can remove the compromised fiducial marker and reregister using the remaining set of $N$-1 fiducial markers. There will be cases when TRE increases dramatically on removing the compromised marker. This increase in TRE

will happen when the compromised marker is the only marker which made the system non-collinear. After removing the compromised marker, the resultant fiducial arrangement is almost collinear, and hence is not a good fiducial system for registration. Such a collinear system will exhibit a small value for one of the $f_i$ in Eq. (134), which is likely to yield a high TRE within the region of interest, and thus is probably not suitable for use. The increase in TRE is also possible when the marker removed was the only one close to the region of interest. In such cases the removal of the compromised marker will cause one or more of the ratios, $d_i / f_i$ in Eq. (134) to become large, thus yielding a high TRE in the region of interest. Thus, as a safety measure, when the removal of a compromised marker results in a large TRE within the region of interest, whether because the resulting configuration is collinear or because it is far from the target area, it is advisable to abandon the use of the fiducial system and registration entirely.

Given the fiducial set $X$ of $N$ markers, expected FLE, intended target location **r**, and the compromised marker **M**, the algorithm to answer the question—"Should we (a) remove the compromised fiducial marker and reregister, or (b) abandon the registration entirely?"—can be summarized as follows:

1. Compute using Eq. (134) the expected TRE using $N$-1 markers in $X$, obtained after removing **M**, at the target location. Let us call it $TRE_{N-1}$.
2. If $TRE_{N-1}$ is less than the maximum allowed TRE, then remove the compromised marker **M** from the registration. Otherwise it is not safe to use the fiducial system, and so abandon the registration entirely.

The maximum allowed TRE depends on the application (e.g., ear surgery) and the user (e.g., surgeon) and will be chosen based on the critical nature of the application.

## 5. Discussion

In this chapter we have given an algorithm for finding a fiducial marker that is compromised when at most one marker is compromised. The algorithm uses a threshold selected to produce a desired false-positive rate that equals the fraction of times we are willing to allow an uncompromised fiducial marker to be labeled as compromised marker. We showed early in the chapter the effect of removing an uncompromised fiducial marker from the system on TRE. It tends to increase the TRE. Thus any method chosen for finding compromised marker should avoid choosing an uncompromised marker. It is common practice to declare a marker as compromised if its individual FRE is high. We have shown through the theory on FRE of individual markers that in an uncompromised fiducial system, it is possible for some fiducial markers to have a high FRE. Thus, it is good idea to use a basic understanding of the FRE statistics (derived in Chapter II of this dissertation) in identifying a compromised fiducial marker. An advantage of using this method is the universality of the threshold which is basically specifying the maximum allowed false-positive rate and is independent of the configuration of fiducial markers and of FLE. We have shown that it is not possible to come up with a single parameter like that for other methods.

The algorithm given here for finding the compromised marker is just a beginning. There is considerable scope for improvement in this method, especially improving the true-positive rate when $N$ is low. Though the suggested method is expected to work well with regard to controlling the false-positive rate for all cases, we see that when $N$ is low the true-positive rate is less than desired. It is definitely worthy of future work to analyze these cases in an attempt to determine what can be done to extend the method for cases when $N$ is low. Also we have not investigated the case in which there is more than one compromised fiducial marker. The effect of the presence of more than one compromised marker on the system is not clear, and its investigation also is left for future work.

We also provided a possible algorithm to answer the question—"Should we (a) remove the compromised fiducial marker and reregister, or (b) abandon the registration entirely?" This algorithm can provide advice to the user on what should be done after finding the compromised marker.

# CHAPTER V

## VALIDATION OF A FIDUCIAL FRAME SYSTEM FOR IMAGE-GUIDED OTOLOGIC SURGERY

Image-Guided Surgery (IGS) has found widespread use in neurosurgery. Bone-implanted fiducial markers are used for these surgeries and are known to provide submillimetric accuracy [25]. Such invasive fiducial systems are often used for malignant diseases such as brain tumors. However, for otologic surgery, though it shares many characteristics of neurosurgery, most of its cases are non-malignancies. Thus image-guided otologic surgeons would prefer a non-invasive fiducial system approach with submillimetric accuracy. Such a non-invasive system, called the EarMark™ system, has been developed here at Vanderbilt University for image-guided otologic surgeries. The system consists of a fiducial frame that can be attached rigidly to a patient using a custom-made dental bite block [48, 66-69]. Before using any fiducial system for surgery, it is important to validate its use by determining the accuracy of the system at the intended target regions. Previous validation studies based on cadaveric skulls have confirmed submillimetric accuracy for the EarMark™ system [66, 67, 70]. These studies were based on target markers implanted inside skulls in the target region. This method is not possible for validation using patients. Implanting markers inside the skull is clearly not appropriate for patient testing, and validating the system using anatomical landmark points selected during the surgery and in image space is not accurate because of the difficulty of finding the same point visually in both the spaces. To properly validate the accuracy of the system for patients a method is needed to find a target accurately in both spaces. We describe such a method in this chapter. The new method also has the advantage of collecting all data outside the operating room.

In this chapter we give a more detailed description of the fiducial system and the errors introduced by the EarMark fiducial frame system. Then we present the new validation method. This method, which can be used for any IGS system, involves estimating the TRE at one point based on the TRE measured at a different point. Later in the chapter the accuracy of the fiducial frame system is compared with another commercially available IGS system.

## 1. EarMark™ System

The EarMark™ system is a non-invasive fiducial system that was developed here at Vanderbilt University for image-guided otologic surgery. The fiducial system consists of a rigid frame with 12 fiducial markers mounted on 12 fiducial posts. The fiducial posts are configured such that they surround the surgical field of interest, namely the two ears. The frame is attached to a patient using a custom-made dental bite block. The frame is similar to one developed by Edwards *et al.* [71]. Figure 17 shows two versions of the fiducial frame attached to patients. Version 2, shown in Figure 17(b) is a revision of Version 1, shown in Figure 17(a). Version 1 uses Acustar-I markers(z-kat, Inc, Hollywood, FL): imaging markers for CT and/or MR acquisitions (Figure 14(a)) and physical markers, also known as “divot caps” because of an indentation into which a localization probe is placed during physical localization, for physical data acquisition (Figure 18(a)). Version 2 of the frame uses a new marker system developed at Vanderbilt: 5 mm titanium spheres (Figure 18(b)), which serve as fiducial markers in both CT space and physical space. (The markers in Version 2 do not show up in MR.) Since there is no need to change markers for imaging and physical data acquisition, Version 2 is easier to use and more importantly avoids error that might occur during the change from imaging marker to physical marker required with Version 1. Because each marker of Version 2 is rigidly (and permanently) attached to its post, error during physical localization is also potentially reduced relative that of Version 1 because the divot cap’s connection to the post in Version 1 is releasable and hence less rigid than that of Version 2. Different types of probes are required for physical

localization for the two versions, as shown in Figure 18. In Version 2, the fiducial posts on the horizontal leg are varied in height to minimize the possibility of two or more fiducials appearing in the same CT slice, hence eliminating streak artifacts. The vertical legs in Version 1 have been replaced with legs at 45 degrees to better surround the common surgical approaches around the ears.

The fiducial frame is attached to the patient using a custom-made dental bite block. Dental impressions are obtained for the upper teeth arrangement of the patient and then a bite block is custom-made to match that impression. To attach the frame to the patient, the dental bite block is first attached rigidly to the upper teeth of the patient using screws. The screws do not contact the teeth, but join two pieces of the block on each side of the mouth to hold the bite block tightly against the teeth to avoid any movement. They do not damage the teeth in any way. The frame is then attached to the patient by inserting it into the distal end of the bite block.

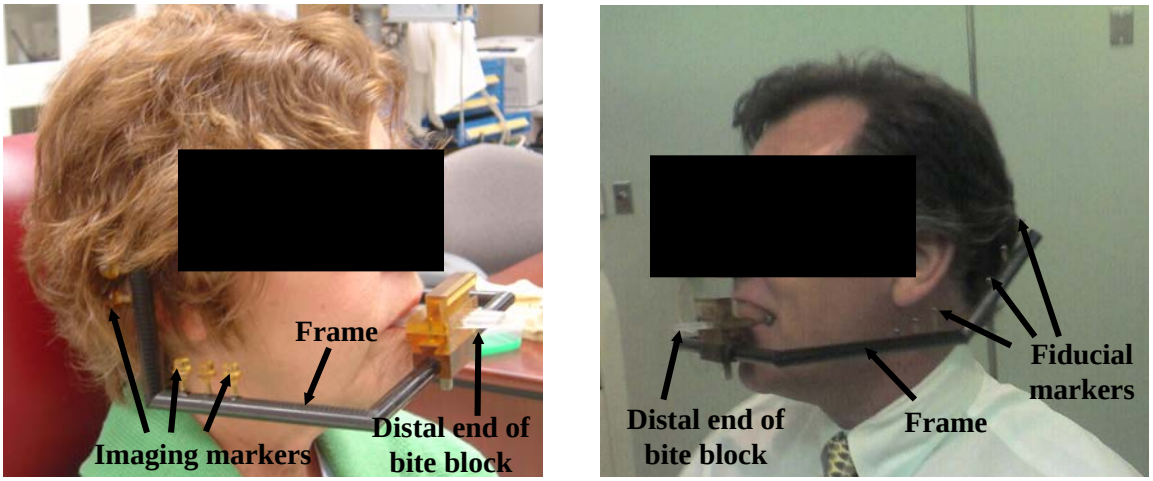


**Figure 17.** EarMark™ system: Fiducial frame attached to patients. (a) Version 1 and (b) Version 2 of the fiducial frame used for the validation study.

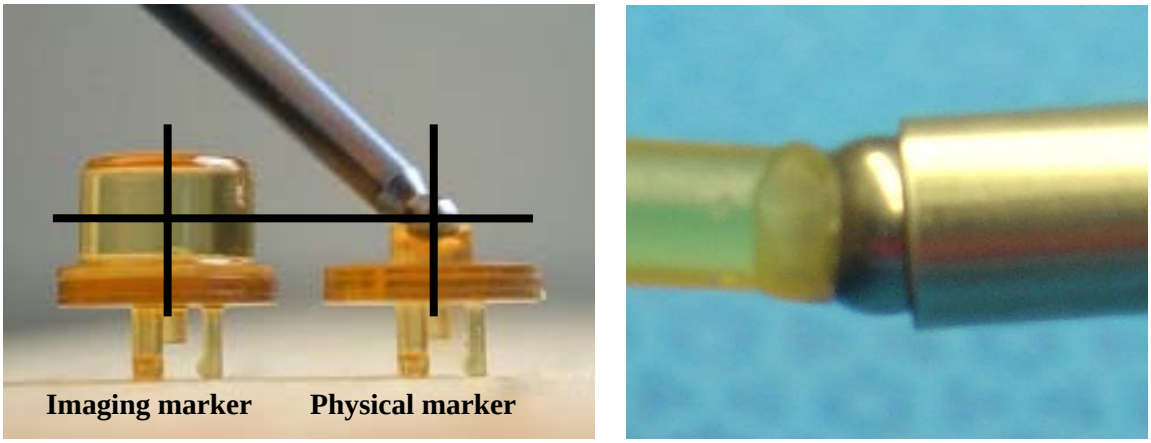


(a) (b)

**Figure 18.** Fiducial markers used in Versions 1 and 2 of the frame. (a) Version 1. Acustar-I imaging marker, which is visible in both CT and MR, and physical marker (also known as a "divot cap". The centers of the imaging marker and a 3 mm spherical probe tip that mates with the divot cap are in the same position relative to the post. (b) Version 2. Spherical titanium marker, visible in CT and localized in physical space via a hollow cylinder probe tip.

To obtain CT scans, the patient wears the bite block with a fiducial frame attached. The imaging markers are attached if needed (for the Version 1 frame). Then clinically applicable temporal-bone CT scans are obtained. The bite-block-fiducial-frame assemblage is then removed from the patient. The fiducial markers show up bright and clear in the CT image space (Figure 19). They can be localized using image processing techniques [72]. The locations of all the 12 fiducial markers in the image and physical space provide the transformation to map the image to physical space. To obtain the fiducial markers' locations in physical space commercially available tracking systems, such as the MicronTracker (Claron Technology Inc, Toronto, Ontario) and the hybrid Polaris (Northern Digital Inc, Waterloo, Ontario) shown in Figure 20, can be used. The fiducial frame is not attached to the patient during physical space localization. Instead, a different frame, called a coordinate reference frame (CRF), is attached to the bite block during the physical localization of the fiducials. The CRF has its own set of markers that can be tracked by the tracking system continuously in real time. The CRF is used only for physical data acquisition and not for imaging. Before the CRF is attached to the patient, a calibration procedure is

performed. For calibration, the fiducial frame is attached to the CRF rigidly and the locations of the fiducial markers in the physical space are obtained relative to this CRF as shown in Figure 21(a). Thus obtained physical locations are registered to the fiducial marker locations in the image space using a point-based registration algorithm [1]. The fiducial frame is then removed from the CRF and attached to the patient using the bite block (Figure 21(b)). Now it is possible to track the physical location of a probe or tool, and find its corresponding location in the CT image space.

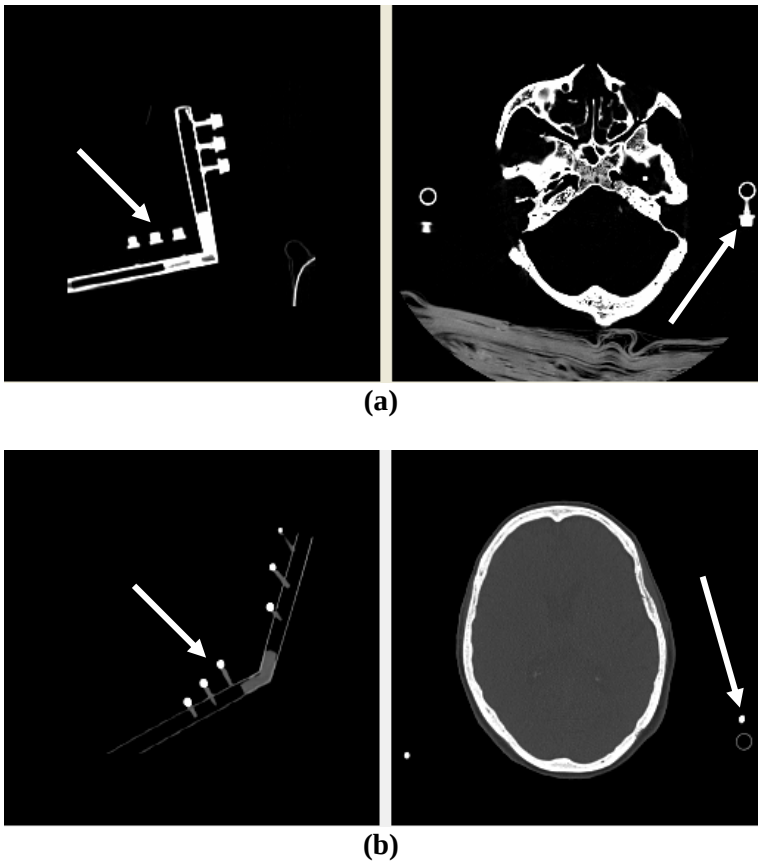

**Figure 19.** Fiducial markers in the CT image space. (a) Version 1 frame: Acustar-I imaging marker. (b) Version 2 frame: Titanium sphere markers. In each case the left image is sagittal and the right image is transverse. Arrows point to example fiducial markers.

**(a)** **(b)**

**Figure 20.** Tracking systems. (a) MicronTracker, (b) Hybrid Polaris.

The idea is that the CRF is attached such that the physical to image space mapping obtained earlier still holds. The advantage of using the CRF is that it allows movement of tracking camera relative to the patient (either or both the camera and patient can move) during the physical tracking, which is of crucial importance in the operating room. Maintaining everything in the same position is a major restriction that is rarely possible to satisfy.

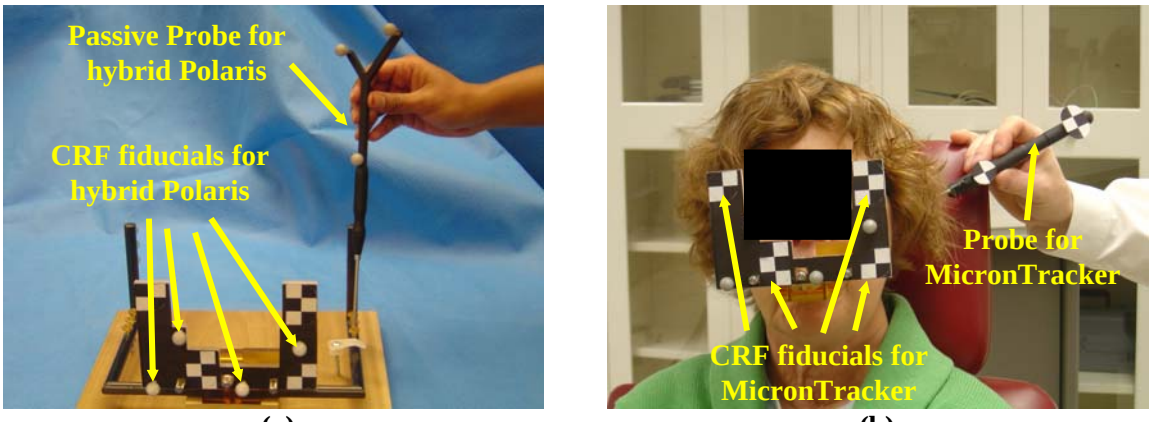


**(a)** **(b)**

**Figure 21.** Physical data acquisition with CRF. (a) Physical localization of fiducial markers on the fiducial frame using the hybrid Polaris system in passive mode. (b) Localization of physical target points on patients using the MicronTracker system (Note – We need to localize the fiducial markers using the MicronTracker system before this).

## 2. Errors Introduced by the EarMark™ System

In this section we will analyze the errors that are introduced while using the EarMark™ fiducial system. For any fiducial system, it is important to analyze the individual error components in order to determine how best to minimize the total error.

Target registration error (TRE) is the measure for analyzing the accuracy of a fiducial system. It is known that fiducial localization error (FLE) contributes to TRE [56, 57]. The fiducial markers on the fiducial frame are used to register the image space with physical space. FLE is the error in localizing the centers of the fiducial markers in the image and physical space. Because of this FLE, the point-based registration between the image and physical space markers is not perfect and hence introduces error at targets.

Though FLE is a contribution to the error in the EarMark™ fiducial system, the largest contribution to the TRE is likely to be due the coupling of the fiducial frame to the subject's dentition [70]. Every time we remove the bite block from the patient and reattach it, there is an inevitable error in repositioning the bite block relative to the teeth, and hence to the skull. This is a cause for the error between imaging and surgery. Figure 22 explains schematically this error due to bite block reposition error. As can be seen the position of the fiducial frame changes relative to the teeth, and hence relative to the patient's head, because of error made while reattaching the bite block.

Thus, for the EarMark™ system, the TRE at any point consists of two components:

1. $TRE_{FLE}$ : TRE due to fiducial localization error (FLE),
2. $TRE_{frame}$ : TRE due to repositioning of the bite block and hence the frame relative to the teeth.

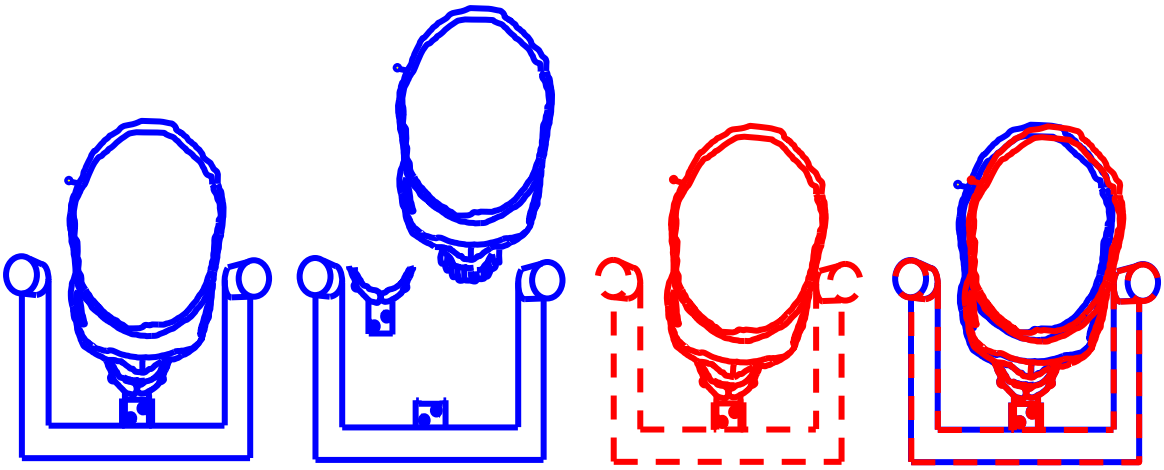


**Figure 22.** Effect of bite block reposition error. (a) The bite block and fiducial frame are attached to the patient during the CT imaging. (b) The bite block and fiducial frame are removed after the CT image volume is obtained. (c) The bite block is reattached to the patient for physical data acquisition. The fiducial frame is shown (dashed lines) even though it is not attached to the bite block to illustrate the bite block relocation error. (d) Overlap of the figures in (a) and (c). If we assume that there is no error in localizing the fiducials, then the fiducial frame overlaps perfectly after registration. Since the bite block did not fit to the patient the same way during the physical localization as it was during CT imaging, the head of the patient do not overlap perfectly.

We can measure the total error experimentally. Let us call it $\mathrm{TRE}_{\mathrm{total}}$. However it is not possible to measure experimentally the individual error components due to FLE and due to movement of the fiducial frame relative to the patient's head. These two error components are due to different reasons, and thus independent of each other. Hence their expected errors add in quadrature. Thus, at any target point **r**

$$\mathrm{TRE}^2_{\mathrm{total}}(\mathbf{r}) = \left\langle \mathrm{TRE}^2_{\mathrm{FLE}}(\mathbf{r}) \right\rangle + \left\langle \mathrm{TRE}^2_{\mathrm{frame}}(\mathbf{r}) \right\rangle . \tag{135}$$

We can estimate the error due to FLE by means of theoretical considerations. At any target point **r**, the expected $\mathrm{TRE}^2$ due to FLE is given by [56]:

$$\left\langle \mathrm{TRE}^2_{\mathrm{FLE}}(\mathbf{r}) \right\rangle = \left\langle \mathrm{FLE}^2 \right\rangle \left( \frac{1}{N} + \frac{1}{3} \sum_{i=1}^{3} \frac{d_i^2}{f_i^2} \right), \tag{136}$$

where $\langle \mathrm{FLE}^2 \rangle$ is the expected squared value of fiducial localization error, $N$ is the number of fiducials used in the registration, $d_i^2$ is the squared distance of the fiducial marker **r** from the principal axis $i$, and $f_i^2$ is the sum of squared distance of all the fiducial points from the principal axis $i$. The value of $\langle \mathrm{FLE}^2 \rangle$ can be estimated by using the relationship [55]:

$$\langle \mathrm{FRE}^2 \rangle = (1 - 2/N) \langle \mathrm{FLE}^2 \rangle, \tag{137}$$

where $\langle \mathrm{FRE}^2 \rangle$ is the expected squared fiducial registration error. FRE for a particular fiducial system can be measured experimentally. It is the root-mean-square (RMS) distance between corresponding fiducials after registration.

From (135), we can then estimate the error contribution of the fiducial frame at any target point **r** as follows:

$$\langle \mathrm{TRE}^2_{\mathrm{frame}}(\mathbf{r}) \rangle = \mathrm{TRE}^2_{\mathrm{total}}(\mathbf{r}) - \langle \mathrm{TRE}^2_{\mathrm{FLE}}(\mathbf{r}) \rangle . \tag{138}$$

We have conducted a study using three human skulls to estimate the individual error contributions. Intracranial fiducial markers were used to represent a "target system". Our report based on that study [70] shows that the major component of the total measured TRE is, as expected, the error due to the repositioning of the bite block. Table 10 summarizes the results of that study.

**Table 10.** RMS TRE Values

| | |
|---|---|
| $\mathrm{TRE}_{\mathrm{total}}$ | 0.73 mm |
| $\mathrm{TRE}_{\mathrm{FLE}}$ | 0.30 mm |
| $\mathrm{TRE}_{\mathrm{frame}}$ | 0.66 mm |

## 3. New Validation Method

Herein, we propose a new method to validate the Earmark™ system for image-guided otologic surgery. The importance of this method is that we can perform the study not only on phantoms and cadavers, but also on patients without intra-operative data collection. For this study we rely on patients who have had BAHA® (Bone-Anchored Hearing Aid) implants. For these patients, a titanium screw is surgically tapped into the skull behind the auricle for these patients. The BAHA® system (www.entific.com) consists of three parts—the titanium implant screw, an external abutment that affixes to the screw and protrudes beyond the skin, and a sound processor. The sound processor can be snapped on and off of the external abutment. For our validation method, a new fiducial post was designed, one end of which snaps onto the BAHA® abutment in place of the sound processor and the other end of which receives a target marker. Figure 23 shows the modified BAHA® target system.

A clinically applicable, temporal-bone CT image is obtained with the patient wearing the fiducial frame and a BAHA target imaging marker attached. The 12 fiducial markers on the frame and the BAHA target marker are then localized in the CT image space [72]. After the CT image is acquired, the bite-block/frame assemblage is removed from the patient. At a later time, the patient comes to a laboratory with a commercially available tracking system. A CRF is attached to the bite block and calibrated as described above and the bite block is re-attached to the patient. The corresponding position of the centers of all the markers (fiducial and target markers) in the physical space of the laboratory are then obtained using the tracking system. Using the 12 fiducial markers on the frame, point-based rigid registration is performed between physical and image space [1]. TRE can then be measured at the BAHA target position, using the locations of the target marker in image space and physical space. We call this measurement $\mathrm{TRE}_{\mathrm{measured}}(\mathrm{BAHA})$.

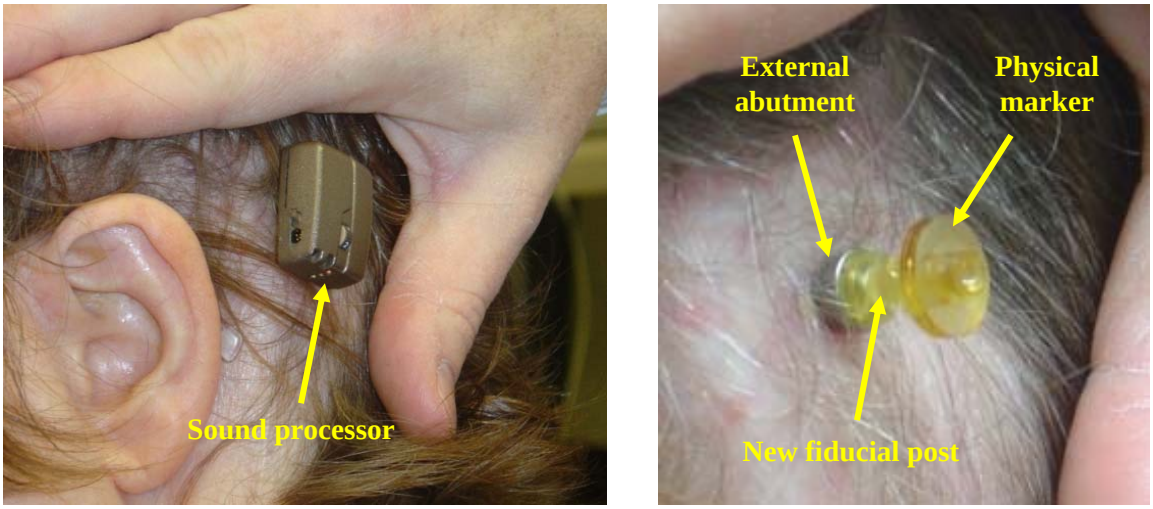


**Figure 23.** BAHA® Target System.

We saw in the previous section that the total TRE due to the EarMark™ system at any target position **r** consists of two components: $\mathrm{TRE}_{\mathrm{FLE}}(\mathbf{r})$ and $\mathrm{TRE}_{\mathrm{frame}}(\mathbf{r})$,which are related by Eq. (135). The measured error at the BAHA, $\mathrm{TRE}_{\mathrm{measured}}(\mathrm{BAHA})$, though, includes one more independent component— $\mathrm{TLE}_{\mathrm{BAHA}}$, which is the error in localizing the BAHA target marker (TLE stands for Target Localization Error). It is an additional error introduced by validation system and is not due to the fiducial system. Thus,

$$\mathrm{TRE}^2_{\mathrm{measured}}(\mathrm{BAHA}) = \left\langle \mathrm{TRE}^2_{\mathrm{FLE}}(\mathrm{BAHA}) \right\rangle + \left\langle \mathrm{TRE}^2_{\mathrm{frame}}(\mathrm{BAHA}) \right\rangle + \left\langle \mathrm{TLE}^2_{\mathrm{BAHA}} \right\rangle . \qquad (139)$$

We can then estimate $\mathrm{TRE}(\mathbf{r})$ at any position **r** from $\mathrm{TRE}_{\mathrm{measured}}(\mathrm{BAHA})$ as explained later in this section.

We will first estimate the value for individual error components at the BAHA target position. Because the marker used as a target is same as those used for the fiducials, we can assume that $\left\langle \mathrm{TLE}^2_{\mathrm{BAHA}} \right\rangle$ equals $\left\langle \mathrm{FLE}^2 \right\rangle$, which is the expected value of the square of the fiducial localization error. The value of $\left\langle \mathrm{FLE}^2 \right\rangle$ can be calculated using (137). $\left\langle \mathrm{FRE}^2 \right\rangle$ is the sum of squared distances between the corresponding fiducial markers after registration. Based on this

estimate of $\left\langle \mathrm{FLE}^2 \right\rangle$, $\left\langle \mathrm{TRE}^2_{\mathrm{FLE}}(\mathrm{BAHA}) \right\rangle$ can be estimated using (136). The error due to the fiducial frame is then given by the relation:

$$\left\langle \mathrm{TRE}^2_{\mathrm{frame}}(\mathrm{BAHA}) \right\rangle = \mathrm{TRE}^2_{\mathrm{measured}}(\mathrm{BAHA}) - \left\langle \mathrm{TRE}^2_{\mathrm{FLE}}(\mathrm{BAHA}) \right\rangle - \left\langle \mathrm{TLE}^2_{\mathrm{BAHA}} \right\rangle. \qquad (140)$$

We are interested in finding the expected target registration error at a point in the inner ear, which for this study is chosen to be the center of the cochlea. The total error at the cochlea, which we call $\mathrm{TRE}(\mathrm{cochlea})$, consists of similar error components. Thus,

$$\left\langle \mathrm{TRE}^2(\mathrm{cochlea}) \right\rangle = \left\langle \mathrm{TRE}^2_{\mathrm{FLE}}(\mathrm{cochlea}) \right\rangle + \left\langle \mathrm{TRE}^2_{\mathrm{frame}}(\mathrm{cochlea}) \right\rangle. \qquad (141)$$

Like $\left\langle \mathrm{TRE}^2_{\mathrm{FLE}}(\mathrm{BAHA}) \right\rangle$ above, $\left\langle \mathrm{TRE}^2_{\mathrm{FLE}}(\mathrm{cochlea}) \right\rangle$ can be computed based on our estimate of $\left\langle \mathrm{FLE}^2 \right\rangle$ by using (136). We can use estimate the value of $\left\langle \mathrm{TRE}^2_{\mathrm{frame}}(\mathrm{cochlea}) \right\rangle$ using the estimated value of $\left\langle \mathrm{TRE}^2_{\mathrm{frame}}(\mathrm{BAHA}) \right\rangle$ as follows. Because of the relatively large sizes of the distances between teeth and inner ear and between teeth and BAHA in comparison to the distance across the teeth themselves, we can expect the error due to repositioning of the fiducial frame to be dominated by rotational errors in the reattachment of the bite block. Because of this dominance, the error can be expected to be approximately proportional to the distance from the teeth. If we assume an exact proportionality then, we can use the following estimate:

$$\left\langle \mathrm{TRE}^2_{\mathrm{frame}}(\mathrm{cochlea}) \right\rangle \approx \left( \frac{d(\mathrm{cochlea})}{d(\mathrm{BAHA})} \right)^2 \left\langle \mathrm{TRE}^2_{\mathrm{frame}}(\mathrm{BAHA}) \right\rangle, \qquad (142)$$

where $d(\mathrm{cochlea})$ and $d(\mathrm{BAHA})$ are the distances of the cochlea and the BAHA, respectively, from the center of the teeth. We can use these estimated values of $\left\langle \mathrm{TRE}^2_{\mathrm{FLE}}(\mathrm{cochlea}) \right\rangle$ and $\left\langle \mathrm{TRE}^2_{\mathrm{frame}}(\mathrm{cochlea}) \right\rangle$ in (141) to get an estimation of the error at the cochlea due to the EarMark™ system.

# 4. Validation Study Results

## 4.1. Validation Study with Cadaveric Skulls

An initial validation study with this new method was conducted using dried human cadaveric skulls [73]. Two skulls with BAHA implants were used for this study. For each skull dental impressions were obtained and the bite blocks were manufactured. The fiducial frame was attached to the skull using the dental bite block. Only Version 1 of the fiducial frame (Figure 17(a)) was used for this study. The imaging markers were snapped onto the fiducial posts on the fiducial frame and the BAHA target imaging marker was also attached. Two different CT scans were obtained for each skull by placing the skull at different angles. The centers of all the 13 markers (12 fiducial markers and one BAHA target marker) were localized in the CT image [72]. The fiducial frame and bite block were removed from the skull after the imaging was completed.

In order to acquire physical data, a CRF was used as explained earlier in this chapter. The CRF was attached to the fiducial frame for calibration. During calibration the imaging markers on the fiducial frame were replaced with divot caps and the centers of all the fiducial markers in the physical space were obtained relative to the CRF. Then, after the calibration step was completed, the fiducial frame was removed and the CRF alone was attached to the skull using the bite block. The imaging marker at the BAHA target was also replaced with the physical marker (the "divot cap") and the position of the center of the BAHA target marker relative to the CRF was recorded.

Eight sets of physical acquisitions were acquired separately for each of the two skulls using two different tracking systems—the MicronTracker and the hybrid Polaris in active mode[2]. The bite block was removed every time from the skull and the fiducial frame. Point-based rigid registration [1] was performed between physical space and image space using the fiducial markers. The position of the target marker was acquired three times for each set of physical

[2] One of the fiducial posts in the fiducial frame was damaged and modified between the time the CT scan of Skull 1 was obtained and some of the physical data were acquired. So for 5 datasets of MicronTracker and all 8 datasets of hybrid Polaris only 11 out of 12 fiducials were used for the registration.

acquisitions to come up with an RMS TRE value at the BAHA. The approximate center of the cochlea was located manually in the image space. The cochlea from the same side of the ear as the BAHA implant was selected. It was found that for the two skulls that we used, the ratio $d(cochlea)/d(BAHA)$ was 0.75 and 0.62 respectively. The TRE value at the cochlea was then computed as explained in the previous section.

**Table 11.** Results of the cadaveric study using Version 1 of the fiducial frame. The error values reported are RMS values and are in mm units.

| | MicronTracker | | Hybrid Polaris | |
|---|---|---|---|---|
| | Skull 1 | Skull 2 | Skull 1 | Skull 2 |
| $\langle \mathrm{FRE}_{\mathrm{measured}} \rangle$ | 0.66 | 0.61 | 0.58 | 0.50 |
| $\langle \mathrm{FLE} \rangle$ | 0.73 | 0.67 | 0.64 | 0.54 |
| $\langle \mathrm{TRE}_{\mathrm{measured}}(\mathrm{BAHA}) \rangle$ | 1.22 | 1.52 | 1.20 | 1.09 |
| $\langle \mathrm{TRE}_{\mathrm{total}}(\mathrm{BAHA}) \rangle$ | 0.97 | 1.36 | 1.01 | 0.95 |
| $\langle \mathrm{TRE}_{\mathrm{FLE}}(\mathrm{BAHA}) \rangle$ | 0.29 | 0.25 | 0.25 | 0.20 |
| $\langle \mathrm{TRE}_{\mathrm{frame}}(\mathrm{BAHA}) \rangle$ | 0.93 | 1.34 | 0.98 | 0.93 |
| $\langle \mathrm{TRE}_{\mathrm{FLE}}(\mathrm{cochlea}) \rangle$ | 0.25 | 0.20 | 0.22 | 0.16 |
| $\langle \mathrm{TRE}_{\mathrm{frame}}(\mathrm{cochlea}) \rangle$ | 0.70 | 0.83 | 0.73 | 0.57 |
| $\langle \mathrm{TRE}(\mathrm{cochlea}) \rangle$ | 0.74 | 0.85 | 0.77 | 0.60 |

Table 11 gives the RMS error values that were observed over all trials. It was found that the RMS TRE values calculated at the cochlea using the MicronTracker and the hybrid Polaris system were 0.8 mm and 0.7 mm respectively. Thus using both the tracking systems on cadaveric skulls, we found that the EarMark™ system provided submillimetric accuracy at the inner ear. As

can be seen in that table, the major component of the total TRE is $\langle \mathrm{TRE}_{\mathrm{frame}}(\mathrm{BAHA}) \rangle$, which as explained above is due to the inaccuracy in reattaching the frame to a subject. This observation is similar to that reported in [70], where intracranial fiducial markers were used.

### 4.2. Validation Study with Patients

An IRB-approved study involving six patients with BAHA implants was conducted. The new validation method was used to estimate the TRE at the cochlea for the patients. This study was similar to the cadaveric experiments described in Section 4.1 above. Dental impressions were obtained for each patient and bite blocks were custom-made. The fiducial frame was attached to the patient using the bite block. Version 2 of the fiducial frame (Figure 17(b)) was used for this study. The sound processor of the BAHA system was replaced with the new fiducial post with the target marker. A clinically applicable temporal bone CT scan of the patient was obtained. The fiducial frame and bite block were removed from the patient. After the CT scan, the patient went to the laboratory in which physical data was to be collected. The target marker was left attached to the patient for those cases to avoid any error made while reattaching it. When the physical data could not be collected the same day, it was made sure that the patient came back to the laboratory for physical data acquisition within a few days. This was done to avoid the deterioration in the accuracy of the system over time [74]. The physical locations of the fiducial markers relative to the CRF were obtained few minutes before the patient comes for the measurements. Once the patient is back in the laboratory the bite block was reattached to the patient, and the physical location of the target marker was obtained (Figure 21(b)). The position of the target marker was acquired three times to come with an RMS TRE value at the BAHA. The bite block was then removed from the patient. The TRE values at the BAHA and the cochlea were computed as described above.

Data from six patients were collected for this study. The physical data were collected using two tracking systems—MicronTracker and hybrid Polaris in passive mode. The approximate center of the cochlea in the same side as the BAHA implant was located manually in the image space for each patient. The ratio $d(cochlea)/d(BAHA)$ for the six patients were found to be 0.61, 0.53, 0.53, 0.59, 0.70, and 0.54. Table 12 and Table 13 report the RMS error values that were observed for this study using the MicronTracker and hybrid Polaris tracking system, respectively. The RMS TRE at the cochlea was found to be 0.89 mm and 0.87 mm with the MicronTracker and hybrid Polaris tracking system respectively. It must be noted though that there were instances when the TRE at the cochlea was above 1 mm, but never above 1.5 mm. Also for Patient1's data with the hybrid Polaris tracking system, we observed that the total error due to the EarMark™ system is very negligible. Thus when the square error component at the BAHA due to the fiducial frame was computed using (138), it was a small negative value. This is possible if the bite block fit the patient in approximately the same way during the imaging and physical data acquisition. The fiducial frame component was hence assumed to be zero because it was a small negative value, which has no meaning in this case. We did not observe negative values with the MicronTracker system. This difference in behavior between the two systems is possible if the bite block moved even slightly in between the switch between the two tracking systems. Also we should note that we cannot arrive at an exact value without averaging over multiple trials. We did not have the luxury to perform multiple sets of physical acquisitions by removing the bite block, reattaching it, and then acquiring the data again as we did with skulls in the earlier study. The patient's comfort was a main concern, and hence multiple data set acquisitions were not acquired.

**Table 12.** RMS error values observed for the patients using the MicronTracker tracking system.

| | Patient1 | Patient2 | Patient3 | Patient4 | Patient5 | Patient6 |
|---|---|---|---|---|---|---|
| $\langle \mathrm{FRE}_{\mathrm{measured}} \rangle$ | 0.70 | 0.53 | 0.39 | 0.60 | 0.54 | 0.62 |
| $\langle \mathrm{FLE} \rangle$ | 0.77 | 0.58 | 0.43 | 0.66 | 0.59 | 0.68 |
| $\langle \mathrm{TRE}_{\mathrm{measured}}(\mathrm{BAHA}) \rangle$ | 1.62 | 1.83 | 2.03 | 1.56 | 0.89 | 1.90 |
| $\langle \mathrm{TRE}_{\mathrm{total}}(\mathrm{BAHA}) \rangle$ | 1.43 | 1.74 | 1.98 | 1.41 | 0.67 | 1.77 |
| $\langle \mathrm{TRE}_{\mathrm{FLE}}(\mathrm{BAHA}) \rangle$ | 0.33 | 0.35 | 0.31 | 0.25 | 0.21 | 0.25 |
| $\langle \mathrm{TRE}_{\mathrm{frame}}(\mathrm{BAHA}) \rangle$ | 1.39 | 1.70 | 1.96 | 1.39 | 0.64 | 1.76 |
| $\langle \mathrm{TRE}_{\mathrm{FLE}}(\mathrm{cochlea}) \rangle$ | 0.26 | 0.28 | 0.25 | 0.22 | 0.19 | 0.23 |
| $\langle \mathrm{TRE}_{\mathrm{frame}}(\mathrm{cochlea}) \rangle$ | 0.84 | 0.91 | 1.05 | 0.82 | 0.44 | 0.94 |
| $\langle \mathrm{TRE}(\mathrm{cochlea}) \rangle$ | 0.88 | 0.95 | 1.08 | 0.85 | 0.48 | 0.97 |

**Table 13.** RMS error values observed for the patients using the hybrid Polaris tracking system.

| | Patient1 | Patient2 | Patient3 | Patient4 | Patient5 | Patient6 |
|---|---|---|---|---|---|---|
| $\langle \mathrm{FRE}_{\mathrm{measured}} \rangle$ | 0.62 | 0.80 | 0.75 | 0.41 | 0.50 | 0.77 |
| $\langle \mathrm{FLE} \rangle$ | 0.68 | 0.87 | 0.82 | 0.45 | 0.54 | 0.84 |
| $\langle \mathrm{TRE}_{\mathrm{measured}}(\mathrm{BAHA}) \rangle$ | 0.69 | 1.36 | 2.44 | 2.11 | 1.19 | 1.53 |
| $\langle \mathrm{TRE}_{\mathrm{total}}(\mathrm{BAHA}) \rangle$ | 0.08 | 1.05 | 2.29 | 2.06 | 1.06 | 1.28 |
| $\langle \mathrm{TRE}_{\mathrm{FLE}}(\mathrm{BAHA}) \rangle$ | 0.29 | 0.35 | 0.31 | 0.17 | 0.19 | 0.30 |
| $\langle \mathrm{TRE}_{\mathrm{frame}}(\mathrm{BAHA}) \rangle$ | 0 | 0.99 | 2.27 | 2.05 | 1.04 | 1.25 |
| $\langle \mathrm{TRE}_{\mathrm{FLE}}(\mathrm{cochlea}) \rangle$ | 0.23 | 0.28 | 0.25 | 0.15 | 0.17 | 0.28 |
| $\langle \mathrm{TRE}_{\mathrm{frame}}(\mathrm{cochlea}) \rangle$ | 0 | 0.53 | 1.21 | 1.21 | 0.72 | 0.67 |
| $\langle \mathrm{TRE}(\mathrm{cochlea}) \rangle$ | 0.23 | 0.60 | 1.24 | 1.22 | 0.74 | 0.72 |

## 5. Comparison of IGS Systems

In the last two sections we saw a method to find the accuracy of the EarMark™ system using the BAHA patients. We were able to estimate the approximate accuracy of the EarMark™ fiducial system at the cochlea based on the TRE measured at the target marker attached to the BAHA abutment post. In this section we propose a method to compare two or more different IGS and tracking systems using the BAHA target marker. We can use the TRE measured at the BAHA target marker to our advantage, and compare the accuracy of two or more IGS systems that are based on different registration methods.

There are different registration methods available for performing image-to-physical registration. They could be surface-based methods [15-20] or point-based methods [1, 21-26]. Once the registration is performed, irrespective of which method is used, it should be possible to take a point in the image space and find its corresponding point in the physical space or vice versa. Due to the error in the registration method there will be an error in finding the corresponding point. The error can be evaluated if we know exactly the physical point that corresponds to the image space point being transformed or vice versa. In practice it is not possible because the points usually correspond to anatomical regions that make it difficult to visually find exact corresponding points in the other space. This is in fact the reason that we need a registration method. For experiments using cadaver skulls, it is possible to implant markers in the target region and use their location in the image and physical spaces as the gold standard. This is not possible though with patients. However, we can use the new fiducial post with a target marker at the BAHA to our advantage, because we know its actual location in both the spaces.

In order to compare different IGS systems, we can register image and physical space using the registration method for that IGS system. Using the registration transformation, we can transform the BAHA target marker location in the image space to the physical. The actual physical location of the BAHA target marker can also be obtained using a tracking system. The distance between the actual physical location and the transformed image space location of the

BAHA target marker gives the TRE at the BAHA target marker. For each registration method we can find the TRE at the BAHA target marker, and they can be used to compare the performance of different methods at that target region.

In this section we report the experiment performed to compare the accuracy of the EarMark™ system that is based on rigid-body, point-based registration with the accuracy of a commercially available IGS system, BrainLab VectorVision® system, that is based on surface-based registration. We will refer to the BrainLab VectorVision® system as BrainLab from here for ease of reference. The BrainLab system that we used for our study is used at our institution for functional endoscopic sinus surgery.

### 5.1. Computing TRE using the BrainLab VectorVision ® System

A CT volume of the patient is loaded on to the IGS system. The software available in the machine lets us choose the type of registration we would like to perform. We choose the surface-based registration method, which is the one used in the operating room, so that we can compare it with the point-based registration used by the EarMark™ system. The software installed in the system extracts the surface of the face of the patient. The surface points in the physical space are obtained by laser scanning the face to obtain corresponding facial features (Figure 24(a)). A reference head band, which is the CRF for this system, is attached to the patient before any physical data acquisition as shown in Figure 24. The software performs surface-based registration to best fit the surfaces in the image space and physical. After the registration the software reports if the registration was optimal, good, or bad. If the registration is reported to be bad, then the physical surface points are rescanned. The registration is accepted otherwise. The probe needed for physical point data collection is calibrated. The BAHA target marker is attached to the patient. The location of the BAHA target marker is acquired three times to come up with a mean value for the TRE. All these points are transformed to the CT image space and stored in log files by the software in the system. The TRE at the BAHA is computed by comparing thus stored locations

with the actual location of the marker in the CT image space. This gives us a measure of the TRE at the BAHA target using the BrainLab system.

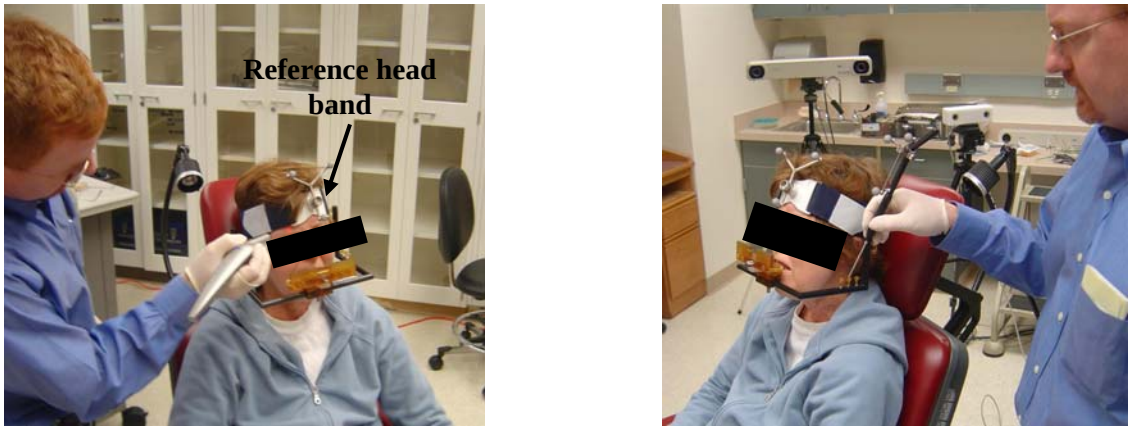


**Figure 24.** BrainLab system data acquisition. (a) Laser scanning of the surface points. (b) Data acquisition after registration is performed.

### 5.2. Results

Data was collected for the same six patients as for the validation of the EarMark™ fiducial system. The BAHA target marker location in the physical space was obtained three times each using both the IGS systems (EarMark and BrainLab). For the EarMark system the data was collected using both MicronTracker and hybrid Polaris tracking systems. The BrainLab IGS also collects data using hybrid Polaris tracking system, but not the same one we used for the EarMark system. Table 14 gives a comparison of the accuracy of the EarMark and BrainLab IGS systems based on the data collected using the six patients. Using the three acquisitions of the BAHA target marker for each patient and for each tracking system, we get three values of TRE at the BAHA from which we can compute a mean and standard deviation for each system and for each patient. These mean and standard deviation values are reported in Table 14. The overall mean, standard deviation, and RMS values of TRE at the BAHA target marker are also reported. Comparison between the groups using t-tests with Bonferroni correction shows that the EarMark system with

hybrid Polaris tracking system (p=0.033) and MicronTracker tracking system (p=0.033) performed significantly better than the BrainLab system. No significant difference was observed between the use of hybrid Polaris and MicronTracker tracking system for the EarMark system (p>0.7). We can see that the EarMark IGS is almost twice as accurate as the BrainLab IGS. The accuracy of surface-based registration probably reduced by the tendency of the skin to deform between the time the CT image is acquired and the physical data collected. It is important to note that the BrainLab system was designed for sinus surgery and hence may not be expected to perform well at the BAHA location, which is far from its main region of interest. The points collected on the facial surface do not surround the region of interest, and hence a higher TRE is expected [56].

**Table 14.** Comparison of the accuracy of EarMark and BrainLab IGS systems at the BAHA. (All units are in mm.)

| Patient | EarMark | | BrainLab |
|---|---|---|---|
| | Hybrid Polaris | MicronTracker | |
| 1 | 0.67 ± 0.18 | 1.62 ± 0.18 | 2.77 ± 0.41 |
| 2 | 1.36 ± 0.05 | 1.81 ± 0.34 | 4.42 ± 0.19 |
| 3 | 2.44 ± 0.04 | 2.00 ± 0.40 | 1.85 ± 0.04 |
| 4 | 2.09 ± 0.35 | 1.54 ± 0.34 | 4.59 ± 0.19 |
| 5 | 1.18 ± 0.16 | 0.81 ± 0.46 | 2.70 ± 0.01 |
| 6 | 1.50 ± 0.38 | 1.89 ± 0.17 | 2.90 ± 0.14 |
| **Mean ± St Dev** | **1.54 ± 0.63** | **1.61 ± 0.49** | **3.21 ± 1.02** |
| **RMS** | **1.66** | **1.68** | **3.36** |

## 6. Discussion

In this chapter we have presented a new method to validate fiducial systems. It is important to analyze the factors that contribute to error in a fiducial system in order to understand how to minimize the total error. A non-invasive fiducial system for image-guided otologic surgery has been described in this chapter, and its error contributions analyzed. Based on the individual error contributions and using to our advantage the possibility of introducing a marker

at the external abutment of the BAHA patients, we have a method to validate fiducial systems. We are able to estimate the TRE at the cochlea using the TRE measured at the BAHA target marker. This method could be applied to other fiducial systems with proper analysis of their error components. The accuracy of the EarMark™ system was determined using this method, and the RMS TRE at the cochlea was found to be 0.89 mm and 0.87 mm with the MicronTracker and hybrid Polaris tracking system respectively when validated with patients. We also used the accuracy measured at the BAHA target marker to compare different IGS systems and tracking systems. We found that the Earmark™ system is more accurate than the BrainLab® system. This also indicated that the point-based registration based on fiducials is more accurate than surface-based registration. We did not find any significant difference in using the two different tracking systems—MicronTracker and hybrid Polaris—for the EarMark™ system.

# CHAPTER VI

## ACCURACY EVALUATION OF MICROTARGETING™ PLATFORMS FOR DEEP-BRAIN STIMULATION USING VIRTUAL TARGETS

### 1. Introduction[3]

In 1998 FDA approval was granted for deep brain stimulation (DBS) for patients with Parkinson's disease and essential tremor. DBS is a surgical procedure that treats the tremor, rigidity, and drug-induced side effects in patients with these diseases by means of electrical stimulation. Since that year, the procedure has gained considerable recognition for the treatment of movement disorders [50, 51]. It requires that a 4-contact electrode be placed within small deep-brain target nuclei such as the subthalamic nucleus (STN), which is a structure approximately 6x4x5 mm in size [75]. Because of the small size of the targets, the placement of the electrodes traditionally requires the accuracy provided by stereotactic frames. The electrode must be placed within the target nucleus for effective stimulation [52]. If the contacts are away from the target by 3-4 mm, then the stimulation is ineffective because (a) it fails to stimulate the desired group of neurons, (b) undesired areas are stimulated resulting in unpleasant stimulation, or (c) it requires higher currents to produce the desired effect, thereby reducing the battery life of the implant. When the center of the electrode is placed within about 1 mm of the targeted neurons, these problems are avoided. Thus submillimetric accuracy is critical.

DBS targets include the Ventral intermediate nucleus (Vim), the subthalamic nucleus (STN), and the Ventrocaudalis nucleus. Targets are typically selected preoperatively in CT and/or MR images. They are not clearly visible in CT or MR images and are selected based partly on the nearby structures that are clearly visible [76]. The surgeon then adjusts the target position

[3] The virtual-target approach and our results on dual-target platforms were presented at the *2007 IEEE International Symposium on Biomedical Imaging: From Nano to Macro* in April 2007 [77].

intraoperatively based on the electrical feedback measured in the operating room. Thus the main steps for DBS electrode implantation are as follows [61]: (1) determining the approximate location of surgical targets preoperatively, (2) mapping the key features associated with the intended target interoperatively, (3) adjusting the final target of implantation interoperatively by appropriate shifts in three-dimensional space, and (4) implanting the 4-contact electrode with the contacts surrounding the final desired target.

Stereotactic frames are traditionally employed to guide the target localization and implantation process [61]. A recently developed alternative is a miniature platform—the STarFix™ microTargeting™ Platform (FDA 510(K), Number: K003776, Feb 23, 2001, FHC, Inc.; Bowdoin, ME, USA). Unlike the traditional frame, which requires intraoperative adjustments for every target, each platform[4] is fabricated so that it is pre-aimed at the planned target or targets. Thus, with a platform, intraoperative adjustments are necessary only if targets are changed intraoperatively. Figure 25 (A and B) shows the two types of platform available for unilateral and bilateral implantations respectively. Titanium anchors (WayPoint™, FHC, Inc.) are implanted into the patient's skull and act as bases for attaching the platforms to the patient (Figure 25 (C and D) ). Three and four anchors are needed for the single-target and dual-target platforms respectively. An MR image volume of the head is typically obtained and a CT image volume is obtained after implanting the anchors. The CT image is required in order to determine the positions of the anchors, which are invisible in MR. Because of its superior soft-tissue discrimination, MR facilitates target selection. (No MR images were acquired in this study because the phantom skulls contain no MR-imagable substance.) The two images are then registered, fused, and viewed by the surgeon. A platform is then designed and custom-made based on the trajectory path relative to the anchor locations, as determined in the images automatically by a computer program (see the Methods section below) [53]. The trajectory path is

[4] To avoid the repeated use of the name microTargeting™ Platform throughout this paper, we will henceforth use the term "platform".

defined by specifying the target location and an entry point. Thus the platform is specific to each patient and each procedure. During the surgery the platform is mounted on the anchors and then used to guide the implantation through a rigid guide-tube rigidly attached to the platform. Figure 25(E) shows a single-target platform along with guide-tubes attached to a phantom skull. The central guide-tube (arrow in Figure 25(F) ) is aimed to lead to the target position initially chosen. The other guide-tubes are used only if a new target location is chosen intraoperatively. The miniature platform has the following advantages over the traditional frame: (1) The image acquisition and the target planning can be done prior to the day of the surgery. (2) The smaller and lighter platform allows freedom of movement to the patient, who is awake during the procedure for movement evaluation. (3) Bilateral implantations can be performed during one procedure using either two single-target platforms or one dual-target platform.

The customized platform was shown to have submillimetric accuracy in reaching the target by its manufacturer for in vitro FDA testing. A phantom that included a physical target was used for the accuracy evaluation by the manufacturer. They reported difficulty with measurements due to collisions between the probe and target. An IRB-approved study was subsequently conducted by some of us [61] to measure the accuracy of the system in a clinical setting. Electrode placement error, which is the distance between the planned target location and the initial electrode placement (i.e., before correction based on intra-operative evaluation) was measured in that study. The mean error for 20 implantations was found to be 2.8 mm. This error reflected the error involved both in the surgical process and in a post-operative image-registration step. In an effort to reduce the overall error, it is important to isolate individual error contributions. To isolate the platform's contribution to the error, which arises both from error in the fabrication of the platform and error in its fixation to the head, we report here on an in vitro study using skull phantoms, which is based on the recently introduced concept of virtual targets [77]. Preliminary experiments have shown that dual-target platforms have submillimetric accuracy with 0.45 mm

root-mean-square (RMS) error [77]. In the current work we report the results of experiments conducted with both single-target and dual-target platforms.

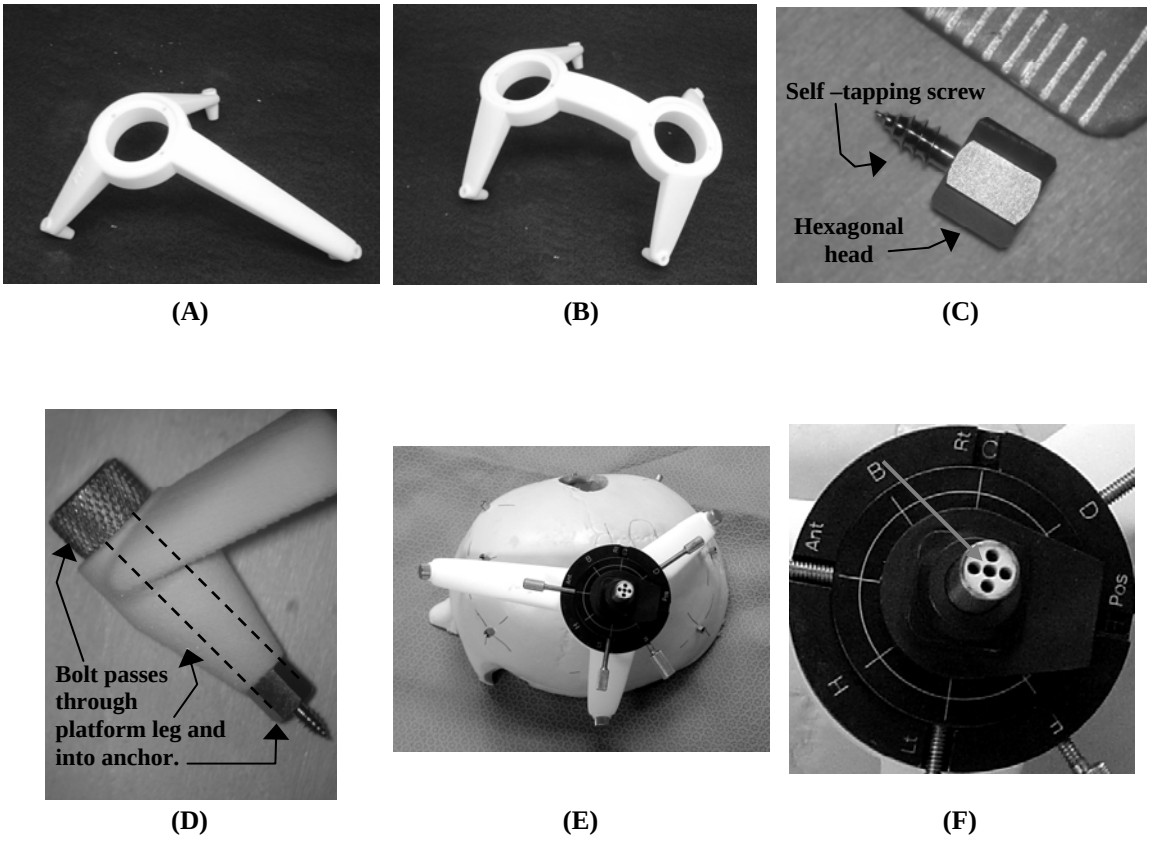


**Figure 25. MicroTargeting™ Platform system.** (A) Single-target platform. (B) Dual-target platform. (C) Anchors used in attaching a platform to the skull. One end of the anchor is a self-tapping screw which attaches to the skull. The other end is a hexagonal head that mates with a driver. The ruler is marked in millimeters. (D) The hexagonal portion has female threads in the top to accommodate a bolt, which passes through a leg of a platform and into the anchor to attach the platform to the anchor. (E) Single-target platform along with guide-tubes mounted on a phantom skull. (F) Guide-tubes attached to the platform. The central guide-tube (arrow) is aimed at the initially chosen target. The other tubes, each at a distance of 2 mm from the central tube are used for lateral adjustments. The cluster of 5 tubes can itself be shifted radially by 3 mm (not shown).

## 2. Methods

Our goal is to measure the distance by which a probe physically misses a target chosen within a phantom skull. The target is defined relative to a coordinate system fixed in the skull. The most direct approach would be to place a physical target in the skull and measure the distance from probe to target. Indeed this direct method was employed for the FDA testing of this platform mentioned above. However, with the direct method it is common for the probe to collide with the target, thereby preventing an accurate measurement. We have overcome this problem by replacing each physical target with a *virtual target*, which is a geometrical point specified relative to a fiducial system. The fiducial system is fixed in the skull and is not used as part of the platform's targeting system. It is important to note that there is no physical object located at the virtual target. Instead, there is a set of physical fiducials fixed in the skull that provides a means to define a coordinate system. By "fiducial" we mean specifically a point within some marker that can be accurately localized both in image space and in physical space. The fiducials are far enough from the virtual target that the probe will not collide with them. Any set of three coordinates *x,y,z* can specify a target relative to this fiducial system and hence relative to the skull, and any such target is a virtual target. In this section we will describe this method in detail.

In our testing we use an artificial plastic skull (Anatomical Chart Company, Skokie, IL) that is cut so that we have physical access to an interior region in which DBS targets are typically found. These represent the points at which the DBS electrodes are to be placed. To enhance the rigidity of the relatively pliable plastic, which plays the role of bone, we fill the hollow skull with a ceramic casting compound (Rescor 740, Cotronics Corp., Brooklyn, NY).

A circular ring, to which 16 fiducial markers are attached, is affixed to the inside of the skull (Figure 26). The fiducials are Titanium spheres of diameter 4.4 mm, whose centers can be localized accurately both in CT space and in physical space. Each phantom is imaged in a CT scanner, and then virtual targets are defined in image space relative to these fiducials. The 16 fiducials on the ring are positioned such that they surround the target region [59]. As mentioned

above, these fiducials are not involved in the platform targeting, but are used to provide a coordinate system fixed in the skull, relative to which virtual targets can be defined. It is important to note that, as can be seen in Figure 26, neither the fiducials nor the coordinate system defined relative to them is attached to the platform. They are attached only to the skull. Thus, any error in fixation of the platform relative to the skull will be revealed as an error in positioning of the probe relative to the virtual target, which is defined relative to the fiducial coordinate system.

In order to increase the relevance of our tests to DBS surgery, we obtain target positions by manually registering each skull CT volume to a single atlas CT volume obtained from another study [78], in which a cluster of target locations has been determined from a set of 31 DBS patients. Two target points are defined for each skull—a mean cluster position of the left STN and a mean cluster of the right STN. Random perturbations selected from a normal distribution with a standard deviation chosen to match that of the cluster are then applied to these positions to produce virtual targets in the CT image space. Entry positions, while not as critical as target positions, are also chosen so as to mimic typical entry positions for DBS patients. Each phantom CT is loaded into a planning software system (microTargeting WayPoint™ Planner, FHC, Inc.), which automatically locates each of the anchor positions, permits the user to enter the target and entry positions, and designs a platform to meet the specifications. The design parameters are then emailed to a fabrication facility (FHC, Inc.), and the platform is built and shipped back to us.

A rigid probe, shown in Figure 27(A) is used to play the role of the rigid guide-tube through which the DBS electrode implant is placed. The probe is a rigid cylindrical aluminum piece 124.75 mm in length with a sphere of diameter 9.5 mm at one end and an attachment piece at the other end shaped to mate with the platform. Once the platform arrives at the testing site, it is mounted on the anchors and the entry point(s) are marked on the skull. The platform is removed, and two burr holes are drilled in the skull, each one being at least large enough (25 to 35 mm in diameter) to allow free passage of a cylindrical aluminum probe of 12.7 mm diameter from the platform into the interior of the skull regardless of its angle (Figure 27(B) ). The

platform is then remounted on the anchors, and the probes are inserted into the platform through the burr holes and fixed rigidly to the platform with screws (Figure 27(C) ).

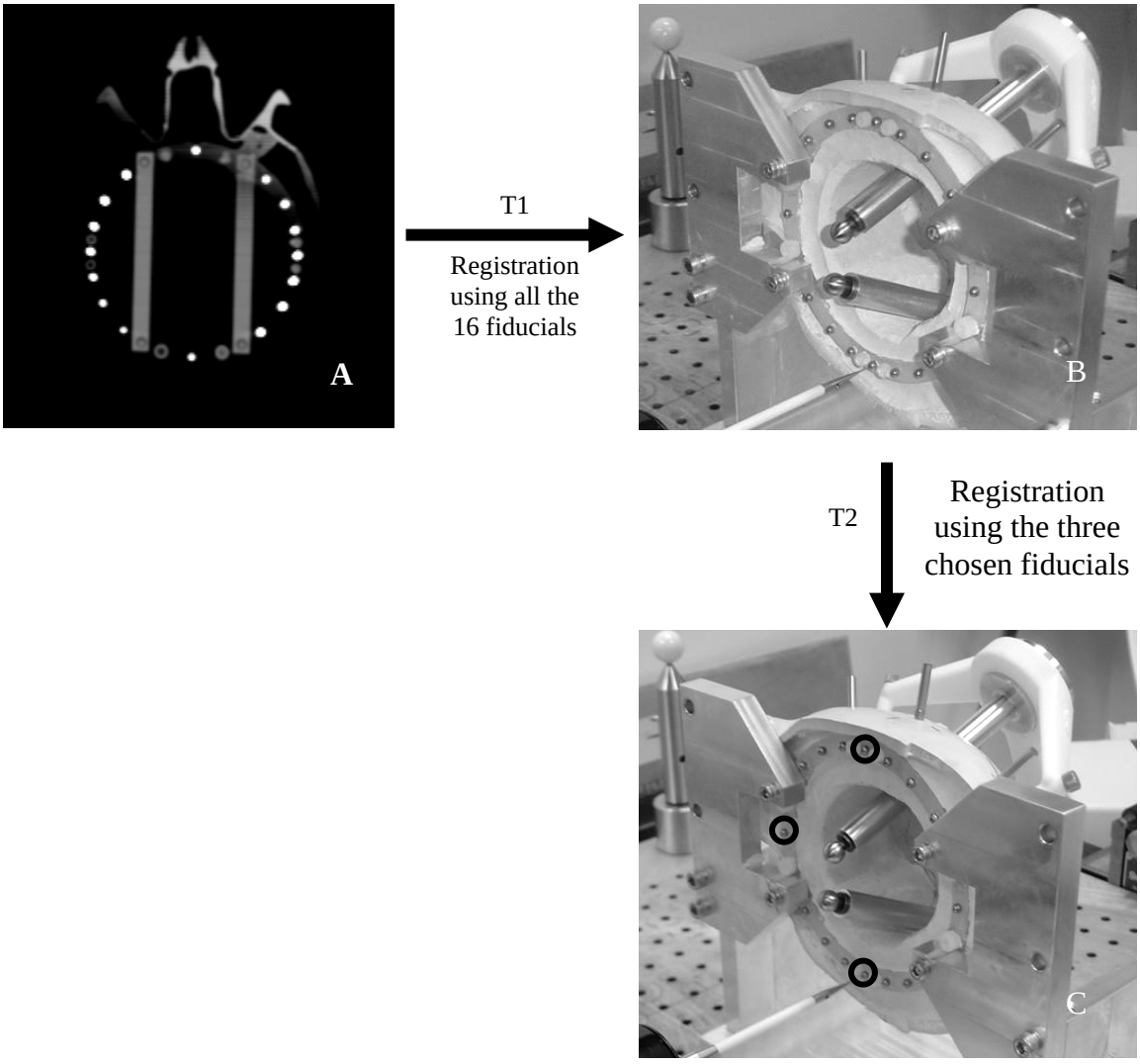


**Figure 26. Localization of fiducials.** (A) The 16 fiducial spheres in the CT image space. (B) Physical localization of the 16 fiducials for Platform 1 for a skull using the CMM. Skull is attached to a holder to avoid movement during the CMM measurements. (C) Physical localization of the 3 fiducials (highlighted using black circles) for Platform 2 for the same skull. For Platform 1, image space is mapped on to physical space using the transformation T1 obtained by registering all the 16 fiducials on the ring in physical and image space. For Platform 2, image space is mapped on to physical space by concatenating the transformations T1 and T2. T2 is obtained by registering the 3 chosen fiducials during the measurements for Platform 2 and Platform 1.

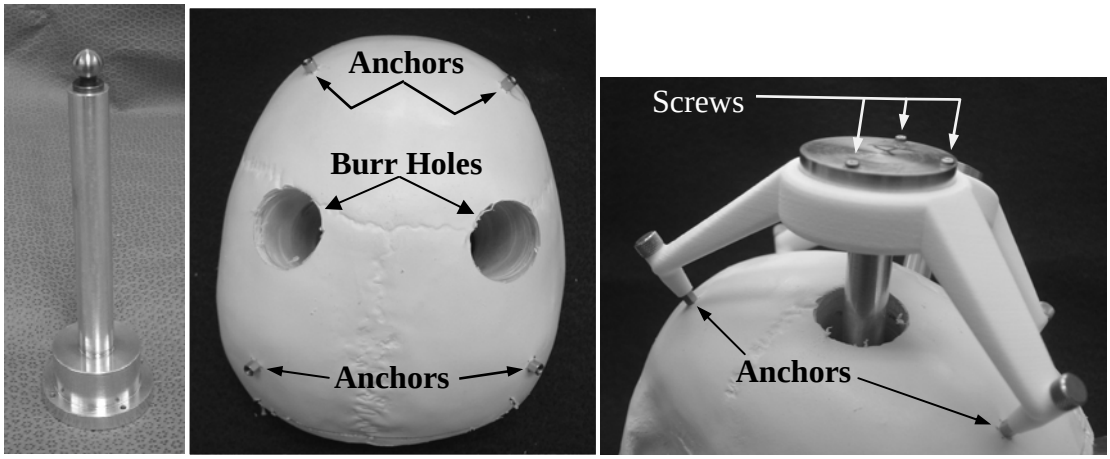


**Figure 27. Attachment of the Probe.** (A) The probe is a rigid aluminum piece 124.75 mm in length and 12.7 mm in diameter with a sphere at one end (top) of diameter 9.5 mm. At its other end is a piece that mates with a hole in the platform. (B) Top of skull showing anchors and burr holes drilled into the skull. Burr holes are of a size large enough (25 to 30 mm in diameter) to accommodate the probe regardless of its angle. (C) The platform is attached to the anchors, and then either one probe (for a single-target platform) or two probes (for a dual-target platform) are placed into the hole(s) in the platform and through the burr hole(s). Three screws fix each probe to the platform via its mating piece.

To comply with typical DBS approaches, the platform is constructed such that the distance of the target from the instrument mounting surface of the platform is 120 mm, and the probe is designed so that, once it is fixed to the platform, its shaft will pass through the entry point and the center of the ball at its tip will lie at the desired target position. The center of the ball at the probe tip is the representative position of the center of the DBS implant. The error of the platform is therefore defined as the physical distance from this center to the virtual target. We call this error the "target registration error" (TRE) in keeping with standard terminology from the field of image registration [1, 56].

Each virtual target is defined relative to the skull in the CT image volume, but it is necessary to know its position relative to the skull in physical space in order to measure the distance by which the physical probe misses the target. The probe can be expected to miss the target because its position is determined by the platform, whose attachment to the skull is subject to error and whose fabrication is subject to error. The physical position of the target relative to the

skull is determined by means of the fiducial markers on the ring that is attached to the skull. These markers are localized both in the image and physical space. Point-based registration [1, 56] is performed between image space and physical space to calculate the position of the target in physical space from its position in image space. At the conclusion of that calculation, the position of the target relative the skull in physical space is known.

All physical space data, namely the centers of the spherical fiducial markers and the centers of the probe tips, are acquired with a Brown and Sharpe, Chameleon coordinate measuring machine (CMM) (Wright Industries, Nashville, TN, calibration 4/11/06, certificate 4112006029735005) (Figure 26). The CMM probe makes contact with five or more points on the surface of a sphere to compute its center (using algorithms and programs residing on the CMM). The platform's measured targeting error is the distance between the center of the probe tip (measured by the CMM) and the virtual target obtained by transforming the image space target point on the basis of the positions of the fiducials in the two spaces. The measured target registration error, which we label $TRE_M$, is computed for each target for each platform. $TRE_M$ is not the true error, but is the magnitude of the vector sum of three error components, which arise from independent processes. One of these is the true error that we desire to measure, while the other are corrupting errors that arise from the measurement process:

1. $TRE_F$—which is the error in transforming the virtual target from image space to physical space caused by combined fiducial localization error (FLE) in image and physical space
2. $TLE$—target localization error, which is the error in the localization of the probe tip in physical space by the CMM
3. $TRE_P$—true error of the platform, which is the error contributed by flaws in the localization of the anchors, the fabrication of the platform based on these anchor localizations, and the mounting of the platform onto the anchors.

Thus,

$$\mathbf{TRE}_M = \mathbf{TRE}_F + \mathbf{TLE} + \mathbf{TRE}_P \tag{143}$$

While $\mathbf{TRE}_M$ is the error that we measure, it is $\mathbf{TRE}_P$ that we wish to report. The presence of $\mathbf{TRE}_F$ and **TLE** will result in a tendency of the magnitude $TRE_M$ , which we report in our Results section to have a mean on the order of 0.42 mm, to be an overestimate of the true magnitude of platform error, $TRE_P$. To minimize that problem, we have designed our measurement technique so that the first two errors are negligible in comparison with the third. Thus, we expect to have

$$\mathbf{TRE}_M \approx \mathbf{TRE}_P \tag{144}$$

In order to establish that Eq. (144) is correct, we show that $TRE_F$ and TLE are likely to be negligible by means of statistical estimates. First we note that the RMS value of $\mathrm{TLE}$ has been measured for the CMM machine by its manufacturer at 0.0055 mm, which is almost two orders of magnitude below our observed $TRE_M$, as reported below under Results. Secondly, we can also estimate TLE as follows: All the physical measurements for a skull are performed on the same day within a short period of time (less than 90 minutes) using the same CMM with no changes in the environmental conditions. Therefore, we can safely assume that the magnitude of the physical error in localizing the centers of the larger probe tips—the TLE—is approximately the same as, if not less than, that of the physical FLE made in localizing the smaller fiducial spheres on the ring. FLE can be estimated using the following equation [1, 56]:

$$\left\langle \mathrm{FLE}^2 \right\rangle = N \left\langle \mathrm{FRE}^2 \right\rangle \Big/ \left( N - 2 \right) \tag{145}$$

where $\langle . \rangle$ has the meaning, “expected value of”, and $\mathrm{FRE}$ is fiducial registration error, which is the root-mean-square (RMS) distance between corresponding fiducials after a registration. The physical locations of fiducial markers are obtained using the CMM for different platforms mounted on the same skull. Point-based registration [1] can be performed between corresponding fiducial marker locations and the FRE measured. Then using Eq. (145) FLE can be computed.

Using this method for all skulls, RMS FLE in physical space was found to be 0.0071 mm, which is comparable to the manufacturer's estimate and is likewise negligible compared to $TRE_M$.

RMS $TRE_F$ error can be estimated using the equation [1, 56]:

$$\left\langle \mathrm{TRE}_\mathrm{F}^2 \right\rangle = \frac{\left\langle \mathrm{FLE}^2 \right\rangle}{N}\left(1+\frac{1}{3}\sum_{k=1}^{3}\frac{d_k^2}{f_k^2}\right) \tag{146}$$

where $\left\langle \mathrm{FLE}^2 \right\rangle$ is computed using Eq. (145) using registrations between image space to physical space, $N$ is the number of fiducials, $d_k$ is the distance of the virtual target from the $k^{\text{th}}$ principal axis of the fiducial set, and $f_k$ is the RMS distance of the fiducials themselves from their $k^{\text{th}}$ principal axis. As given in our Results section below, the result is 0.0344 mm, which is an order of magnitude below the observed mean of $TRE_M$. Thus both $TRE_F$ and TLE can be expected to be an order of magnitude or more smaller than $\mathrm{TRE}_\mathrm{M}$, indicating that Eq. (144) is indeed correct. Therefore, while our results are expected to overestimate $TRE_P$, the overestimation is likely to be negligible.

## 3. Experiment

Measurements were made on twenty platforms—eight single-target platforms and twelve dual-target platforms—mounted on four skulls. Five platforms were fabricated for each of the four skulls. The single-target platforms, which are employed to perform unilateral procedures, require three anchors; the dual-target platforms, which are employed for bilateral procedures, require four anchors. For each of the four skulls, twelve anchors were implanted with anchor placements selected by a trained neurosurgical resident, and a CT scan was obtained on a Phillips Mx8000 IDT 16 (sixteen-slice acquisition, 120 kVp, 400mA, 750 milliseconds, slice thickness = 0.75 mm, pixel sizes = 0.422, 0.404, 0.586, and 0.490 mm for skulls 1, 2, 3, and 4, respectively). On each skull we defined two target points—left STN and right STN—and two entry points. As explained in our Methods section above, the target points were based on typical DBS targets, by

randomly perturbing the mean of the cluster of targets from a patient study—one cluster for left STN and one for right STN. The random perturbation was performed for each combination of skull, target, and platform using the standard deviations of the clusters, which were [0.91, 1.99, 2.05] and [1.24, 1.77, 1.76] mm along the [Left-Right, Posterior-Anterior, Superior-Inferior] directions for left STN and right STN respectively. Then, for each skull three dual-target platforms were built for the anchors, using three sets of four anchors with no anchor in common, and two single-target platforms were built—one for the left and one for the right STN target, using two sets of three anchors. All the dual-target platforms have different left STN and right STN locations. For each skull one of the dual-target platforms was mounted on the anchors, and the two entry points were marked on the skull in the vicinity of the probe mount. Then the platform was removed and burr holes were drilled at those points to provide an entry for the probe for that platform and for the other four platforms.

For each skull, each of its five platforms, was in succession attached to the anchors on the skull and target probes—two for a dual-target platform and one for a single-target platform—were outfitted (Figure 26). The skull was then rigidly attached to a holder to avoid any movement during the CMM measurements, and the holder with the attached skull was placed on the CMM table (Figure 27). The three dual-target platforms were attached and measured first, followed by the two single-target platforms.

After the holder was placed on the CMM table, the locations of the probe tips (or probe tip for a single-target platform) were obtained, and fiducials were localized as well. For each skull, upon its first placement on the table, and only for that first placement, all sixteen fiducials were localized. These sixteen points along with sixteen corresponding image points, which were obtained by localizing these same fiducials in image space, were later used in a registration step that makes it possible to transform the virtual target points in image space into their corresponding positions in physical space. The purpose of using such a large number of fiducials is to compensate somewhat for the relative inaccuracy of image localization. Next, the holder,

with the skull still rigidly attached, was removed from the CMM table. The target probes and Platform 1 were removed from the skull, and Platform 2 was fitted to a different set of anchors. The same probe(s) were then attached to Platform 2, and the holder plus skull was again placed on the CMM table.

Because the holder is unlikely to be replaced on the CMM table in the same position, it is necessary to obtain measurements to permit a re-registration with image space each time the holder is placed on the table. While the registration for Platform 2 could be performed in the same way as was done for Platform 1, i.e., by obtaining the locations of all sixteen fiducials and using them in an image-to-physical-space registration, it is not necessary. Instead, after the holder is replaced on the table with Platform 2 attached, only three of the sixteen fiducials were localized with the CMM. The registration from image space to physical space for Platform 2 was then accomplished using both these three fiducial localizations and the sixteen localizations performed for Platform 1, as illustrated in Figure 26. The registration is accomplished by composing two registration transformations: (1) a transformation based on all sixteen fiducials from image space to the physical space that maps the skull's CT image to the skull in its position on the CMM table with Platform 1 attached and (2) a transformation from physical space to physical space based on the three chosen fiducials that maps the skull in its position on the CMM table with Platform 1 attached to its position on the table with Platform 2 attached. The use of only three fiducials for the second platform reduces the measurement time considerably while causing only a negligible loss of accuracy relative to the use of all sixteen fiducials. The loss is negligible because no image localization is involved in Step (2), and the CMM accuracy of fiducial localization is an order of magnitude better than that of image accuracy of fiducial localization. The three chosen fiducials are well spread, as can be seen in Figure 26. Platforms 3, 4, and 5 were treated similarly to Platform 2. The entire process was repeated for each skull.

## 4. Results

Before making our accuracy measurements, we made estimates of the errors in our measurement technique. In particular, as explained at the beginning of our Methods section, we wished to estimate $\mathrm{TRE}_F$ and TLE. While the manufacturer gives a value for TLE, we made our own independent measurement of it by using the measured positions of the three fiducials that were localized on the CMM for each of the four skulls for Platforms 1 through 4 in a series of point-based registrations. As mentioned in the Methods section, by using these measurements in Eq. (143), we found by this method an estimated RMS(TLE) of 0.00708 mm over all four skulls.

Next, to estimate $\mathrm{TRE}_F$ we began by using the positions of the sixteen fiducials that were localized both in image space and physical space (i.e., from the CMM) for each skull's Platform 1 in a registration between image and physical space to estimate the fiducial localization error (FLE), again using Eq. (145). The resulting estimated image-to-physical $\mathrm{RMS}(\mathrm{FLE})$ over all skulls was 0.127 mm. Using this value in Eq. (146) for each of the target positions gives an estimated $\mathrm{RMS}(\mathrm{TRE}_F)$ of 0.0341 mm over all four skulls and both target positions. This estimate is strictly appropriate only for Platform 1, because with Platforms 2 through 5 a composition of two registrations was employed, as explained in our Methods section. To get an estimate that is appropriate for those platforms, we first used the physical-to-physical $\mathrm{RMS}(\mathrm{FLE})$ of 0.00708 mm for Platforms 2 through 5 for all skulls in Eq. (146) for each of the target, which results in an estimated physical-to-physical $\mathrm{RMS}(\mathrm{TRE}_F)$ of 0.00442 mm over all skulls. To estimate the measurement error resulting from the composition of the image-to-physical transformation and the physical-to-physical transformation for Platforms 2 through 4, we then combine the RMS TREs for image-to-physical and physical-to-physical in quadrature. That combination gives a total estimated $\mathrm{RMS}(\mathrm{TRE}_F)$ for Platforms 2 through 4 for all skulls of 0.0344 mm. The resulting estimates from all these measurements—RMS(TLE) = 0.00708 mm for

all platforms, $\mathrm{RMS}(\mathrm{TRE}_\mathrm{F})$ = 0.0341 mm for Platform 1, and $\mathrm{RMS}(\mathrm{TRE}_\mathrm{F})$ = 0.0344 mm for Platforms 2 through 4 are used only to estimate the error of our method, not to estimate the error of the platforms.

The measured platform errors and statistics are reported in Table 15-17. Table 15 and 16 report the results for the single-target and dual-target platforms, respectively. As we anticipated, the estimated RMS errors of our measurement technique are an order of magnitude below $\mathrm{RMS}(\mathrm{TRE}_\mathrm{M})$. Thus, Eq. (144) is correct, showing that our method overestimates $\mathrm{TRE}_\mathrm{P}$ only negligibly. We analyzed the directions of the errors and found no statistically significant directional bias at $p = 0.05$. Furthermore, we found no statistically significant difference ($p = 0.22$) between using one dual-target platform or two single-target platforms for bilateral procedures.

Table 17 reports the measured error values and statistics combining both types of platforms. Assuming a normal distribution, we find that $\mathrm{TRE}_\mathrm{M}$ is less than 0.80 mm at 99% and 0.90 mm at 99.9%. Thus, the platform attains submillimetric accuracy by a considerable margin.

**Table 15.** Error values for single-target platforms.

| | | **Left STN** | **Right STN** |
|---|---|---|---|
| Skull 1 | | 0.39 mm | 0.81 mm |
| Skull 2 | | 0.43 mm | 0.30 mm |
| Skull 3 | | 0.41 mm | 0.38 mm |
| Skull 4 | | 0.43 mm | 0.46 mm |
| All 4 skulls | | 0.42 mm | 0.53 mm |
| **All 4 skulls, both targets (*N*=8 targets)** | **RMS($\mathrm{TRE}_\mathrm{M}$)** | **0.47 mm** | |
| | **Mean ± SD** | **0.45 mm ± 0.15 mm** | |
| | **Max** | **0.81 mm** | |
| | **Min** | **0.30 mm** | |
| | **99%** | **0.85 mm** | |
| | **99.9%** | **0.96 mm** | |

**Table 16.** Error values for dual-target platforms.

| | **RMS values** | | **Mean values** | |
|---|---|---|---|---|
| | **Left STN** | **Right STN** | **Left STN** | **Right STN** |
| Skull 1 | 0.50 mm | 0.30 mm | 0.50 mm | 0.28 mm |
| Skull 2 | 0.49 mm | 0.46 mm | 0.46 mm | 0.46 mm |
| Skull 3 | 0.47 mm | 0.47 mm | 0.46 mm | 0.43 mm |
| Skull 4 | 0.28 mm | 0.38 mm | 0.27 mm | 0.36 mm |
| All 4 skulls | 0.45 mm | 0.41 mm | 0.42 mm | 0.38 mm |
| **All 4 skulls, both targets (*N*=24 targets)** | **RMS($TRE_M$)** | | **0.43 mm** | |
| | **Mean ± SD** | | **0.40 mm ± 0.15 mm** | |
| | **Max** | | **0.69 mm** | |
| | **Min** | | **0.14 mm** | |
| | **99%** | | **0.78 mm** | |
| | **99.9%** | | **0.89 mm** | |

**Table 17.** Error values for all the platforms.

| | **RMS values** | | **Mean values** | |
|---|---|---|---|---|
| | **Left STN** | **Right STN** | **Left STN** | **Right STN** |
| Skull 1 | 0.48 mm | 0.48 mm | 0.48 mm | 0.41 mm |
| Skull 2 | 0.47 mm | 0.43 mm | 0.45 mm | 0.42 mm |
| Skull 3 | 0.46 mm | 0.45 mm | 0.45 mm | 0.42 mm |
| Skull 4 | 0.32 mm | 0.40 mm | 0.31 mm | 0.38 mm |
| All 4 skulls | 0.44 mm | 0.44 mm | 0.42 mm | 0.41 mm |
| **All 4 skulls, both targets (*N*=32 targets)** | **RMS($TRE_M$)** | | **0.44 mm** | |
| | **Mean ± SD** | | **0.42 mm ± 0.15 mm** | |
| | **Max** | | **0.81 mm** | |
| | **Min** | | **0.14 mm** | |
| | **99%** | | **0.80 mm** | |
| | **99.9%** | | **0.90 mm** | |

## 5. Discussion

Our results show a remarkably high in vitro targeting accuracy for this device. High accuracy is critical for DBS because of the small size of the targets and the need to hit the desired target locations. As discussed above, a placement error on the order of 2-3 mm may have a substantial effect on the success of the procedure or the duration of the batteries. Other targeting

techniques can be employed for DBS, including traditional stereotactic frames and frameless systems based on bone-implanted fiducial markers in intra-operative tracking systems [79]. The most similar system is the NeXframe frameless system (Medtronic, Minneapolis, Minnesota). Our observed mean of 0.42 mm and 99.9% confidence level of 0.90 mm for this platform compare very favorably to in vitro results recently reported for the NeXframe. In a 25-site test involving 560 measurements on plastic skulls similarly to the present study, the NeXframe system exhibited a mean error of 1.25 mm and a 99.9% confidence level of 4.0 mm [80].

Clearly a more important measure of targeting accuracy is in vivo error, but it is difficult to measure the in vivo error for these systems, or for any targeting systems, because of the relatively large errors inherent in the in vivo evaluation itself. The fundamental difficulty is the determination of the true position of the target, which requires some means for an independent determination of target position. The error in that independent determination can be considerably larger than the targeting error of the device being evaluated, resulting in an over estimate of the error of the device. In vivo measurements using the single-target version of the platform, for example, in which the independent measurement was based on a post-operative CT being registered with a pre-operative CT, yielded a mean measurement error of 2.7 mm [61]. As reported in that work, errors arising from movement of the brain relative to the skull between the pre-op and post-op CT along with errors in the registration of the two CT images and the identification of the electrode center in the post-op image all contributed to the measured error. None of these errors affects the actual accuracy of electrode placement, but they tend to add to the measured error. The same problem plagues the in vivo evaluation of traditional frames and frameless systems, whose measured in vivo means range from 3 mm to 4 mm [61, 79, 81] for traditional frames and 3 mm for the NeXframe [79].

It is inevitable that the translation from plastic skulls in the laboratory to human skulls in the operating room will encounter some additional error. However, because human skulls are rigid, the increase is likely to be small. The error that we measure is the error in the placement of a

probe by the platform at a point relative to the skull, not relative to soft tissue, and this measured error is determined by factors that are very similar in humans and in plastic skulls. The anchors, which are made of titanium, are highly visible in CT and are considerably brighter than bone. The determination of the positioning of the platform is based only on the anchors, which are rigidly affixed to the skull, not on the shape or intensity pattern of the skull itself. Thus, differences in the imaging properties of skull and plastic will have a negligible effect, if any, on the targeting accuracy. The anchors fasten rigidly to the human skull, just as they do to a plastic one. Anchor attachment is easier for the plastic skull because of the absence of overlying scalp and muscle, which obscures the view of the anchor during implantation, but this problem can be overcome through practice and proper instrumentation. Thus, while in vitro evaluation tends to underestimate true application error, the similarity to the in vivo situation suggests that the underestimation is likely to be mild. On the other hand, in vivo evaluation tends to overestimate the error, and because of the confounding errors of the independent target determination, the overestimation is likely to be severe. Thus, it can be argued that, for placement of probes in the head, in vitro measurements are as credible a predictor of in vivo targeting accuracy as in vivo measurements, if not more so, and in view of the margin with which the platform achieved submillimetric accuracy in vitro, it seems quite safe to extrapolate our results to submillimetric targeting accuracy in the OR.

## 6. Conclusion

We have employed a method based on the concept of the virtual target to evaluate the accuracy of a new stereotactic frame—the microTargeting™ Platform—which is currently being used to guide surgeries for deep-brain stimulation. The virtual target eliminates the problem of collisions between the probe, which the platform is designed to place at a target, and the target itself and thus makes the evaluation more accurate. Each virtual target is defined relative to a fiducial system that is arranged such that it surrounds the target, thereby reducing the error due to

fiducial localization inaccuracies. In vitro experiments were performed with virtual targets chosen within plastic models of human skulls. The positions of the targets are based on the mean target positions of 31 DBS patients, and the planning procedure is performed similarly to the planning performed for DBS surgery. Both single-target and dual-target platforms were evaluated. Our method is likely to overestimate the platform error slightly, but our statistical estimates show that the overestimation is likely to be negligible. The mean of the observed targeting errors was 0.42 mm, and, if we assume normal error distributions, then in this testing environment fewer than one in a thousand errors would be expected to reach a millimeter. While the results apply strictly only to our in vitro testing, the similarity to the in vivo situation combined with the small size of the measured errors suggests with very high probability that for DBS surgery the microTargeting™ Platform is accurate to submillimetric level.

# CHAPTER VII

# CONCLUSIONS AND FUTURE WORK

## 1. Conclusions

In this dissertation we have discussed various errors involved in rigid-body point-based registration systems and methods to measure, analyze, and predict these errors. An introduction to the general problem and its background along with definitions of important terms and types of errors is given in Chapter I.

In Chapter II we derive approximate expressions for the distribution of fiducial registration error (FRE) of an individual fiducial marker **r**. No expressions for this error have been available before. We show that FRE can be resolved into three orthogonal components along the directions $\hat{\mathbf{r}}$, $\hat{\mathbf{v}}$, and $\hat{\mathbf{w}}$ such that the three components are independent, zero-mean normal distributions with variances $\sigma_r^2$, $\sigma_v^2$, and $\sigma_w^2$. The $\text{FRE}^2$ at any fiducial marker is thus distributed as the sum of three chi-square variables with variances $\sigma_r^2$, $\sigma_v^2$, and $\sigma_w^2$. We define the directions to be chosen for $\hat{\mathbf{r}}$, $\hat{\mathbf{v}}$, and $\hat{\mathbf{w}}$, and derive expressions for the variances in those directions. We note that the variance along the radial direction $\hat{\mathbf{r}}$ is larger than those in the two perpendicular directions. We also show that the distribution of FRE along any arbitrary direction $\hat{\mathbf{a}}$ is a normal distribution with zero mean and variance $\sigma_a^2$, and we derive an expression for that variance.

Our derivations are based on first-order approximations, but in Chapter III, we present the results of simulations that the expressions derived in Chapter II agree very closely to ground-truth simulations of point-based registration. Because our calculated distributions are approximations, they do not work so well for nearly-collinear fiducial configurations when

fiducial location error (FLE) is extremely high. Some examples of such extreme cases are shown, but it is very rare though for those cases to occur in practice. We validate the approximate formula for FRE of an individual fiducial marker **r**. We examine the variation in individual FRE with changes in different parameters of the fiducial system, such as the number of fiducial markers ($N$), FLE, and the arrangement of fiducial markers. We verify that the individual FRE increases with $N$ and with FLE, as predicted by the derivations of Chapter II. The individual FRE is also affected by the fiducial arrangement, which can be understood with the help of better understanding of the expected FRE as given by our derivations.

In Chapter IV, we use the knowledge of the distribution of FRE gained from Chapter II to produce an algorithm to find the compromised fiducial marker, if any, in a fiducial system. Though there are various possible threshold-based methods that compare the measured individual FRE value with a common threshold, such thresholds on the size of FRE need to be selected based on the given fiducial configuration. There is no single threshold that will work for all configurations to meet the desired accuracy in finding compromised markers and also avoid finding uncompromised markers, and even if the configuration is given, there is no single threshold that will work for all markers in that configuration. Our algorithm is based on setting a threshold on the *probability* of observing for a given fiducial marker its measured FRE in a given direction. We give a simple formula for calculating a probability threshold that will produce a desired false-positive rate for the identification of compromised markers That formula is based only on the desired rate and the number of markers, and with it and our algorithm, we have a universal approach that works for all numbers of markers, all configurations, and all values of FLE. We show in this chapter that this approach works through simulations that are similar to those of Chapter III. Finally, we suggest an algorithm to decide whether the fiducial system should be used after removing the compromised marker from registration or the use of the fiducial system should be abandoned.

We have also described in this dissertation two types of validation methods in which error in rigid-body point-based registration plays the central role. In Chapter V, we present a validation method for the evaluation of the accuracy of fiducial-frame systems. The method has the distinct advantage that it can be conducted outside the operating room and yet estimates accuracy at target regions reachable only in the operating room. The method relies on volunteers from a unique set of patients. These are patients with bone-attached hearing aids (BAHA®) implanted just behind the ear. The goal is to validate a fiducial frame based on fiducial mrkers that has been developed for image-guided otologic surgery. A target marker is introduced at the BAHA location via a specially designed attachment, and target registration error (TRE) is measured via that marker. In the validation method, the measured TRE at the BAHA location is analyzed into additive components, which are then used to estimate the TRE at other target locations—the ones reachable only in the operating room. We show using this method that the fiducial frame provides submillimetric accuracy at the cochlea. We also apply the validation method to the comparison of accuracies of different commercial systems for image-guided surgery (IGS). First, we compare two different tracking systems for use with the frame—the MicronTracker and the Hybrid Polaris and find that either can be employed with no significant loss in accuracy. Second, we compare the accuracy of the fiducial frame to that of a system based on surface-based registration—the BrainLab system—for otologic targets. We find that the frame system is more accurate than the BrainLab system in this region.

In Chapter VI we present our second validation method. The goal here is an in vitro evaluation of the accuracy of the StarFix microTargeting platform. This platform is a commercial system designed to guide the tip of a rigid probe to a target deep inside the human brain during surgery to implant a deep-brain stimulator. The common problem in evaluating such devices is collisions of the probe with the target, which leads to inaccurate measurement of the error due to the targeting system. We introduce the concept of “virtual targets” to avoid this problem. A fiducial system is rigidly fixed to plastic human skull models. Virtual targets are defined relative

to this fiducial system and hence to the skull, and are placed in the region of a cluster of target points derived from actual patient procedures. Our results show that the mean error of this platform is 0.42 mm.

It is highly important, while measuring error of a certain system, to eliminate error caused by extraneous factors due to the validation technique that are not contributed by the particular system being evaluated. Elimination of this extraneous error is a central issue in each of the two validation methods described Chapters V and VI but the approach is different in each. In Chapter V, we analyze the measured error into independent additive components which are due to identifiable factors, and calculate statistical estimates of the device error by estimating and then subtracting the error not contributed by it. This approach is appropriated when extraneous errors are non-negligible but it is possible to measure, compute, or estimate them. In Chapter VI, we solve the problem by carefully setting up the validation procedure such that extraneous errors are negligible and then justifying their neglect by estimating them.

Thus in this dissertation we analyzed in detail the different registration errors involved in fiducial systems. We first analyzed the nature of fiducial registration error. Then we analyzed the different components involved in the measured target registration error and used them to validate fiducial systems and targeting frames.

## 2. Future Work

There is a lot of scope for future research in the continuation of the theory on FRE. Our derivations assume equal weighting for all the fiducials during registration, but it could be extended to include unequal weighting. The main assumption in our derivation is that FLE for all the fiducials is independent and are drawn from a zero-mean normal distribution with equal variance for all fiducials in all directions, *i.e*. the FLE distribution is the same for all fiducials and is isotropic. This assumption is common in the analysis of errors in this field [55, 56, 57], and results based on this assumption have proven quite useful in the field of neurosurgery, orthopedic

surgery, and radiation oncology where bone-attached fiducial markers are being used. It must be noted though that FLE may be anisotropic in image space when the spatial resolutions in the image coordinate directions are different and anisotropic in the physical space when coordinate reference frames are used [82]. The problem of extending the derivations to include this anisotropy is difficult with no closed-form solution to the rigid-body point-based registration problem with different weights in different directions. Currently available solutions are iterative in nature [83, 84] and hence time consuming. With the necessity to perform the registration with high speed, it is preferred to assume isotropic FLE and use the closed-form solution for the registration. Wiles *et al.* [85] recently provided a statistical model for TRE when FLE is anisotropic but still used the closed-form solution for the registration purpose. It should be possible to extend the statistical model for FRE also using a similar approach.

The formulas derived in Chapter II can be used to understand better the accuracy of a fiducial system. The goal of any fiducial system is to register two spaces so as to produce the smallest possible TRE at the intended target regions. Knowledge of the distribution of the individual FRE of a fiducial marker could guide us find fiducials that are compromised. We provided such a method to find the compromised fiducials which can also reasonably avoid choosing good markers as bad markers. The current algorithm works well for $N$ greater than 10, but does not handle well cases when $N$ is less than 10. Cases in which $N$ is small are important, for example when bone-implanted markers are used because of the desire to reduce the invasive nature of the process. Thus it would be beneficial to refine the method to handle small $N$. We did not investigate cases in which more than one fiducial marker is possibly compromised. The analysis of the impact of having more than one compromised fiducial could result in a totally different approach to finding the compromised markers, because it is not obvious how the system would behave in such cases.

Once we identify the compromised fiducials, another important question is how to handle a compromised marker after identifying it. The two possible solutions suggested in Chapter IV are to remove the compromised marker and reregister using the remaining fiducials, or, as a safety measure, to abandon the use of the fiducial system. If some knowledge of the distribution of the error at the compromised marker can be estimated, then we could weight the compromised marker differently from other markers, perform weighted point-based registration [1], and use the fiducial system. We may be able to reduce the effect of compromised marker on the TRE by weighting the compromised marker appropriately. Thus, as a future work in this regard it will be beneficial to come up with a method to estimate the error distribution at the compromised marker location.

It is hoped therefore that this dissertation provides a start to future research efforts in the registration field to improve the registration accuracy that will lead to better outcomes when image guidance is used in surgical procedures.

# APPENDIX

## 1. Notations

| | |
|---|---|
| Expected value | $\langle . \rangle$ |
| Matrix | nonbold font |
| Scalar | nonbold font |
| Vector | bold font. Components of vectors are in nonbold font as they are scalars. |
| Unit vector | vector with a hat symbol ($\hat{}$) |

## 2. Symbols

NOTE: The symbols listed below are used in this work to represent specific meanings.

| | |
|---|---|
| $K$ | dimension of the space |
| $N$ | number of fiducials used for registration |
| $\sigma$ | standard deviation of the distribution of fiducial localization error |
| R | rotation matrix |
| $\mathbf{t}$ | translation vector |
| $X$, $Y$ | $N$-by-$K$ matrices with positions of $N$ corresponding fiducial markers in two $K$-dimensional spaces that need to be registered |
| $F$ | $N$-by-$K$ matrix with fiducial localization error corresponding to each fiducial in each direction |
| $\mathbf{x_i}$ | $i^{th}$ fiducial marker in $X$, which is the $i^{th}$ column in $X$ |
| $\mathbf{y_i}$ | $i^{th}$ fiducial marker in $Y$, which is the $i^{th}$ column in $Y$ |
| $\mathbf{f_i}$ | fiducial localization error corresponding to the $i^{th}$ fiducial marker, which is the $i^{th}$ column in $F$ |

## 3. Abbreviations

| | |
|---|---|
| BAHA | Bone-Anchored Hearing Aid |
| CRF | Coordinate Reference Frame |
| FLE | Fiducial Localization Error |
| FRE | Fiducial Registration Error |
| IGS | Image-Guided Surgery |
| RMS | Root-Mean-Square |
| TRE | Target Registration Error |

## 4. Glossary

NOTE: The notation in this glossary follows that of Merriam-Webster's Collegiate Dictionary series. The word or words to be defined are given in bold type. The word's part of speech (usually a noun or noun phrase) is given in italics after the word: *n* = "noun"; *vb* = "verb"; *adj* = "adjective". A bold-faced colon (**:**) introduces each definition. When a word has more than one sense, each sense enumerated with a bold-faced Arabic numeral (**1**, **2**, …).

**compromised marker** *n* **:** a fiducial marker whose fiducial point is subject to abnormal fiducial localization error because of some problem not ordinarily expected. For example, while fiducial localization error is to be expected because of noise in the image and because of digitization errors in optical detection in the operating room, error caused by bending of a marker caused by a forceful contact with some object would qualify the marker as being compromised. In this work, fiducial localization error of a compromised marker is expected to be much larger than the expected error.

**coordinate reference frame** *n* **:** (abbr., CRF) a rigid object whose position and orientation can be determined by an image-processing algorithm in image space or by a mechanical or optical device in physical space. The coordinate reference frame is designed to be attached to second

rigid object whose position and orientation cannot be directly determined, so that changes in position and orientation of the second object can be determined. Each point in the second object is measured once relative to the coordinate reference frame (hence the name), and thereafter by tracking changes in position and orientation of the coordinate reference frame, it is possible to infer the new position and orientation of the second object.

**fiducial** *n* **1 :** fiducial point **2 :** fiducial marker

**fiducial-frame system** *n* **:** a rigid apparatus on which fiducial markers are mounted that is designed to be attached to an object in order it is possible to perform rigid-body, fiducial registration for that object.

**fiducial localization** *n* **:** the determination of a fiducial point either by an image-processing algorithm in image space or by a mechanical or optical device in physical space.

**fiducial localization error** *n* **1 :** (abbr., **FLE**) the vector displacement between a true fiducial point and a measured fiducial point **2 :** (abbr., FLE) the distance between a true fiducial point and a measured fiducial point **3 :** (abbr., FLE) the square root of the expected squared distance between a true fiducial point and a measured fiducial point **4 :** (abbr., FLE) the square root of the mean squared distance between a true fiducial point and a measured fiducial point in some set of measurements.

**fiducial marker** *n* **:** any object designed such that it is possible to determine a fiducial point, or points within it, by means of fiducial localization. Fiducial markers may be attached to any object that will be subject to fiducial registration.

**fiducial point** *n* **:** a point in one space whose corresponding point can been determined reliably in a second space. Such corresponding point pairs are used in fiducial registration. Examples are a specific point within a fiducial marker (for example, its center or a divot in its surface), a small cavity in bone, or a vessel bifurcation.

**fiducial registration** *n* **:** a method of registration in which a transformation is found that minimizes some measure of fiducial registration error. In this dissertation it is assumed that the typical measure is minimized, which is the sum of squares of individual registration errors.

**fiducial registration error** *n* **:** (abbr., FRE) when fiducial registration is performed from one space to a second space, a single measure of the set of individual fiducial registration errors (see def.). The measure used in this work (and in most such works on rigid-body, fiducial registration) is the square-root of the mean over all fiducials used in the registration of squares of the magnitudes of the individual fiducial registration errors.

**image-guidance system** *n* **:** any system, typically comprising imagers, computers, real-time tracking systems, pointers, optical or magnetic tracking devices, and trackable instruments, designed to provide real-time tracking of the anatomy of a patient during surgery based on images of that patient. The images are typically acquired pre-operatively, but additional images may be acquired intra-operatively and used in conjunction with the pre-operative images.

**individual fiducial registration error** *n* **1 :** (abbr., **FRE**(**r**)) when fiducial registration is performed from one space to a second space, the resulting vector displacement between a fiducial point measured in one space after it has been transformed to the second space and the fiducial point measured in the second space **2 :** the same definition as 1, but "vector displacement" is replaced by "distance" **3 :** the same definition as 2, but "distance" is replaced by "square root of the expected squared distance" **4 :** the same definition as 2, but "distance" is replaced by "square root of the mean squared distance in some set of measurements".

**localize** *vb* **:** perform fiducial localization

**localization** *n* **:** fiducial localization

**point-based registration** *n* **:** fiducial registration

**register** *n* **:** perform registration

**registration** *n* **:** the determination of a transformation from a first space to a second space that aligns points in a view of an object in the first space with corresponding points in a view of that object in the second space.

**rigid** *adj* **:** moving such that distances between points are unchanged

**rigid-body transformation** *n* **:** a transformation for which the distance between every pair of points in the first space is unchanged by the transformation of the pair into a second space

**rigid-body registration** *n* **:** registration in which the transformation is restricted to be a rigid-body transformation.

**space** *n* **:** a set of positions specified by a coordinate system.

**target** *n* **:** a point of interest in one space whose corresponding point is desired in a second space. When a registration is performed between the two spaces, a target is typically not used as a fiducial.

**target registration** *n* **:** the determination of the corresponding point in one space of a target whose position is chosen in another space.

**target registration error** *n* **1 :** (abbr., **TRE**) when registration (not necessarily fiducial registration) is performed from one space to a second space, the resulting vector displacement between a target point measured in one space after it has been transformed to the second space and the target point measured in the second space **2 :** (abbr., TRE) the same definition as 1, but "vector displacement" is replaced by "distance" **3 :** the same definition as 2, but "distance" is replaced by "square root of the expected squared distance" **4 :** the same definition as 2, but "distance" is replaced by "square root of the mean squared distance in some set of measurements"

**transformation** *n* **:** a mathematical operation in which each of a set of points in one space is mapped to a point in a second space. In this work only rigid-body transformations are considered.

**uncompromised marker** *n* **:** a fiducial marker that is not a compromised marker

**virtual target** *n* **:** a target that is defined in terms of a set of fiducial points. There is no physical object present at the position of the virtual target.

## REFERENCES


1. J. M. Fitzpatrick, D. L. G. Hill, and C. R. Maurer, "Registration". *Medical Image Processing, Volume II of the Handbook of Medical Imaging*, M. Sonka and J. M. Fitzpatrick, ed., SPIE Press. 447-513, 2000.

2. J. V. Hajnal, D. L. G. Hill, and D. J. Hawkes, *Medical Image Registration*, The Biomedical Engineering Series, Series editor Michael R. Neuman, CRC Press.

3. Z. H. Cho, J. P. Jones, and M. Singh, *Foundations of Medical Imaging*, John Wiley and Sons, Inc., New York, 1993.

4. G. N. Hounsfield, Computerized transverse axial scanning (tomography), The *British Journal of Radiology*, 46: 1016-1022, 1973.

5. A. M. Cormack, "Representation of a function by its line integrals, with some radiological applications," *Journal of Applied Physics*, vol. 34, pp. 2722-2727, 1963.

6. R. V. Damadian, "Tumor Detection by Nuclear Magnetic Resonance," *Science*, 171:1151, 1971.

7. P. C. Lauterbur, "Image formation by induced local interactions: example employing nuclear magnetic resonance," *Nature*, 242:190-191, 1973.

8. A. Kumar, D. Welti, and R. R. Ernst, "NMR Fourier zeugmatography," *Journal of Magnetic Resonance*, 18:69-83, 1975.

9. Joseph P. Hornak, *The Basics of MRI*, http://www.cis.rit.edu/htbooks/mri/.

10. T. M. Peters, "Image-guidance for surgical procedures," *Physics in Medicine and Biology*, 51 (2006) R505–R540, 2006.

11. C. R. Maurer, Jr. and J. M. Fitzpatrick, "A review of medical image registration," in *Interactive Image-Guided Neurosurgery*, R. J. Maciunas, Ed., 17-44, American Association of Neurological Surgeons, Park Ridge, IL, 1993.

12. J. B. A. Maintz and M. A. Viergever, "A survey of medical image registration," *Medical Image Analysis*, vol. 2, 1-36, 1998.

13. J. P. W. Pluim, J. B. A. Maintz, and M. A. Viergever, "Mutual-information-based registration of medical images: a survey," *IEEE Transactions on Medical Imaging*, vol. 22, no. 8, pp. 986-1004, Aug 2003.

14. W. R. Crum, T. Hartkens, and D. L. G. Hill, "Non-rigid image registration: theory and practice," *The British Journal of Radiology*, 77(2004), S140-S153, 2004.

15. C. A. Pelizzari, G. T. Y. Chen, D. R. Spelbring, R. R. Weichselbaum, and C. T. Chen, "Accurate three-dimensional registration of CT, PET, and/or MR images of the brain," *Journal of Computer Assisted Tomography*, vol. 13, pp. 20–26, 1989.

16. P. J. Besl and N. D. McKay, “A method for registration of 3-D shapes,” *IEEE Transactions on Pattern Analysis and Machine Intelligence*, vol. 14, pp. 239–256, 1992.

17. D. Lemoine, D. Liegeard, E. Lussot, and C. Barillot, “Multimodal registration system for the fusion of MRI, CT, MEG, and 3D or stereotactic angiographic data,” *Medical Imaging 1994: Image Capture, Formatting, and Display*, Proc. SPIE 2164, 46-56, 1994.

18. H. Jiang, K. S. Holton, and R. A. Robb, “Image registration of multimodality 3-D medical images by chamfer matching,” *Biomedical Image Processing and Three-Dimensional Microscopy* 1992, vol. Proc. SPIE 1660, pp. 356-366, 1992.

19. H. Jiang, R. A. Robb, and K. S. Holton, “A new approach to 3-D registration of multimodality medical images by surface matching,” *Visualization in Biomedical Computing 1992*, vol. Proc. SPIE 1808, pp. 196–213, 1992.

20. A. Collignon, D. Vandermeulen, P. Suetens, and G. Marchal, “Registration of 3D multi-modality medical images using surfaces and point landmarks,” *Pattern Recognition Letters*, vol. 15, pp. 461–467, 1994.

21. W.R. Fright and A.D. Linney, “Registration of 3-D head surfaces using multiple landmarks,” *IEEE Transactions on Medical Imaging*, 12(3):515--520, September 1993.

22. D. L. G. Hill, D. J. Hawkes, M. J. Gleeson, T. C. S. Cox, A. J. Strong,W.-L. Wong, C. F. Ruff, N. D. Kitchen, D. G. T. Thomas, J. E. Crossman, C. Studholme, A. J. Gandhe, S. E. M. Green, and G. P. Robinson, “Accurate frameless registration of MR and CT images of the head: Applications in surgery and radiotherapy planning,” *Radiology*, vol. 191, pp. 447–454, 1994.

23. P. A. van den Elsen and M. A. Viergever, “Marker guided registration of electromagnetic dipole data with tomographic images,” in *Information Processing in Medical Imaging*, A. C. F. Colchester and D. J. Hawkes, Eds., 142--153. Springer-Verlag, Berlin, 1991.

24. C. R. Maurer, Jr., G. B. Aboutanos, B. M. Dawant, R. J. Maciunas, and J. M. Fitzpatrick, “Registration of 3-D images using weighted geometrical features,” *IEEE Transactions on Medical Imaging*, vol. 15, pp. 836–849, 1996.

25. C. R. Maurer, Jr., J. M. Fitzpatrick, M. Y. Wang, R. L. Galloway, Jr., R. J. Maciunas, and G. S. Allen, “Registration of head volume images using implantable fiducial markers,” *IEEE Transactions on Medical Imaging*, 16, 447-462, Aug 1997.

26. C. R. Maurer, Jr., R. J. Maciunas, and J. M. Fitzpatrick, “Registration of head CT images to physical space using a weighted combination of points and surfaces,” *IEEE Transactions on Medical Imaging*, vol. 17, pp. 753–761, 1998.

27. B. F. Green, “The orthogonal approximation of an oblique structure in factor analysis,” *Psychometrika*, vol. 17, pp. 429–440, 1952.

28. P. H. Schönemann, “A generalized solution of the orthogonal Procrustes problem,” *Psychometrika*, vol. 31, pp. 1–10, 1966.

29. J. L. Farrell and J. C. Stuelpnagel, “Problem 65-1: A least squares estimate of satellite attitude,” *SIAM Review*, vol. 8, pp 384-386, 1966.

30. G. H. Golub, and C. F. van Loan, *Matrix Computations*. Baltimore, MD: Johns Hopkins University Press, 1983.

31. R. Sibson, "Studies in the robustness of multidimensional scaling: Procrustes statistics," *Journal of the Royal Statistical Society Series B*, vol. 40, pp. 234–238, 1978.

32. O. D. Faugeras and M. Hebert, "The representation, recognition, and locating of 3-D objects," *The International Journal of Robotics Research*, vol. 5, pp. 27-52, 1986.

33. M. Froimowitz and S. Matthysse, "Geometrical correspondence between phenazocine and the enkephalins," *Journal of Medicinal Chemistry*, vol. 29, pp. 573-578, 1986.

34. K. S. Arun, T. S. Huang, and S. D. Blostein, "Least-squares fitting of two 3-D point sets," *IEEE Transactions on Pattern Analysis and Machine Intelligence*, vol. 9, pp. 698–700, 1987.

35. B. K. P. Horn, "Closed-form solution of absolute orientation using unit quaternions," *Journal of the Optical Society of America A*, vol. 4, pp. 629–642, 1987.

36. B. K. P. Horn, H. M. Hilden, and S. Negahdaripour, "Closed-form solution of absolute orientation using orthonormal matrices," *Journal of the Optical Society of America A*, vol. 5, pp. 1127–1135, 1988.

37. M.W. Walker and L. Shao, "Estimating 3-D location parameters using dualnumber quaternions," *CVGIP: Image Understanding*, vol. 54, pp. 358-367, 1991.

38. S. Umeyama, "Least-squares estimation of transformation parameters between two point patterns," *IEEE Transactions on Pattern Analysis and Machine Intelligence*, vol. 13, 376-380, 1991.

39. P. A. Viola, *Alignment by maximization of mutual information*. Ph.D. thesis, Massachusetts Institute of Technology, 1995.

40. R. P. Woods, S. R. Cherry, and J. C. Mazziotta, "Rapid automated algorithm for aligning and reslicing PET images," *Journal of Computer Assisted Tomography*, vol. 16, pp. 620–633, 1992.

41. R. P. Woods, J. C. Mazziotta, and S. R. Cherry, "MRI-PET registration with automated algorithm," *Journal of Computer Assisted Tomography*, vol. 17, pp. 536–546, 1993.

42. F. Maes, A. Collignon, D. Vandermeulen, G. Marchal, and P. Suetens, "Multimodality image registration by maximization of mutual information," *IEEE Transactions on Medical Imaging*, vol. 16, pp. 187–198, 1997.

43. W. M. Wells, III, P. Viola, H. Atsumi, S. Nakajima, and R. Kikinis, "Multi-modal volume registration by maximization of mutual information," *Medical Image Analysis*, vol. 1, pp. 35–51, 1996.

44. C. Studholme, D. L. G. Hill, and D. J. Hawkes, "An overlap invariant entropy measure of 3D medical image alignment," *Pattern Recognition*, vol. 32, pp. 71–86, 1999.

45. R. H. Clarke and V. Horsley, "On a method of investigating the deep ganglia and tracts of the central nervous system (cerebellum)," *Br. Med. J.*, vol. 2, 1799-1800, 1906.

46. V. Horsley and R. H. Clarke, "The structure and function of the cerebellum examined by a new method," *Brain*, vol. 31, 45-124, 1908.

47. E. A. Spiegel, H. T. Wycis, M. Marks, A. J. Lee, "Stereotaxic apparatus for operations on the human brain," *Science*, vol. 106, 349-350, 1947.

48. R. F. Labadie, M. Fenlon, H. Devikalp, S. Harris, R. Galloway, and J. M. Fitzpatrick, "*Image-guided otologic surgery*," In: H. U. Lemke, M. W. Vannier, K. Inamura, A. G. Farman, K. Doi, J. H. C. Reiber, eds. *Computer Assisted Radiology and Congress and Exhibition*. Amsterdam, The Netherlands: Elsevier Science, 627–32, 2003.

49. Schlaier J, Warnat J, and Brawanski A. "Registration accuracy and practicability of laser-directed surface matching," *Computer Aided Surgery*, 7:284-90, 2002.

50. A. L. Benabid, L. Vercucil, A. Benazzouz, A. Koudsie, S. Chabardes, L. Minotti, P. Kahane, M. Gentil, D. Lenartz, C. Andressen, P. Krack, and P. Pollak, "Deep brain stimulation: What does it offer?," *Advances in Neurology*, 91: 293–302, 2003.

51. G. Deuschl, R. Wenzelburger, F. Kopper, and J. Volkmann, "Deep brain stimulation of the subthalamic nucleus for Parkinson's disease: A therapy approaching evidence-based standards," *Journal of Neurology*, 250(suppl 1):143–146, February, 2003.

52. B. Schrader, W. Hamel, D. Weinert, and H. M. Mehdorn, "Documentation of electrode localization," *Movement Disorders*, 17(suppl 3): S167–S174, 2002.

53. J. I. Franck, P. E. Konrad, R. Franklin, and F. Haer, "StarFix™: A novel approach to frameless stereotactic neurosurgery utilizing a miniaturized customized pretargeted cranial platform fixture – technical description, unique features, and case reports," *Movement Disorder Society 7th International Congress of Parkinsons Disease and Movement Disorder*, Miami, 2002.

54. S. P. Langron and A. J. Collins, "Perturbation theory for generalized Procrustes analysis," *Journal of the Royal Statistical Society Series B*, vol. 47, pp. 277–284, 1985.

55. R. Sibson, "Studies in the robustness of multidimensional scaling: Perturbational analysis of classical scaling," *Journal of the Royal Statistical Society Series B*, 41:217-229, 1979.

56. J. M. Fitzpatrick, J. B. West, and C. R. Maurer Jr., "Predicting error in rigid-body, point-based registration," *IEEE Transactions on Medical Imaging*, 17, 694-702, 1998.

57. J. M. Fitzpatrick and J. B. West, "The distribution of target error in rigid-body, point-based registration," *IEEE Transactions on Medical Imaging* 20, 917-927, Sep 2001.

58. G Barnette, Comments on reference [59], *Neurosurgery*, 48, 816-7, April 2001.

59. J. B. West, J. M. Fitzpatrick, S. Toms, C. R. Maurer, Jr., and R. J. Maciunas, "Fiducial point placement and the accuracy of point-based, rigid-body registration," *Neurosurgery*, 48, 810–817, April 2001.

60. C. Snyderman, L. A. Zimmer, and A. Kassam, "Sources of registration error with image guidance systems during endoscopic anterior cranial base surgery," *Otolaryngology-Head and Neck Surgery*, 131(3), September 2004.

61. J. M. Fitzpatrick, P. E. Konrad, C. Nickele, E. Cetinkaya, and C. Kao, "Accuracy of customized miniature stereotactic platforms," *Stereotactic and Functional Neurosurgery*, vol. 83, no. 1, pp. 25–31, 2005.

62. R. Balachandran and J. M. Fitzpatrick, "The Distribution of Registration Error of a Fiducial Marker in Rigid-Body Point-Based Registration," accepted for presentation in SPIE Medical Imaging 2008, Feb 2008.

63. C. Goodall, "Procrustes methods in the statistical analysis of shape," *Journal of the Royal Statistical Society Series* B, 53, 285-339, 1991.

64. A. C. Rencher, *Linear Models in Statistics*, New York: Wiley, 2000.

65. W. H. Press, B. P. Flannery, S. A. Teukolsky, and W. T. Vetterling, *Numerical Recipes in C*, New York: Cambridge Univ. Press, 1990.

66. R. F. Labadie, R. J. Shah, S. S. Harris, E. Cetinkaya, D. S. Haynes, M. Fenlon, S. Juscyzk, R. L. Galloway, and J. M. Fitzpatrick, "Submillimetric Target-Registration Error using a Novel, Non-Invasive Fiducial System for Image Guided Otologic-Surgery," *Computer-Aided Surgery*, 9(4):145-53, 2004.

67. R. F. Labadie, R. J. Shah, S. S. Harris, E. Cetinkaya, D. S. Haynes, M. Fenlon, S. Juscyzk, R. L. Galloway, and J. M. Fitzpatrick. "In vitro assessment of image-guided otologic surgery: submillimeter accuracy within the region of the temporal bone," *Otolaryngology-Head and Neck Surgery*, 132(3):435-442, 2005.

68. R. F. Labadie, P. Choudhury, E. Cetinkaya, R. Balachandran, D. S. Haynes, M. Fenlon, S. Juscyzk, and J. M. Fitzpatrick, "Minimally-invasive, image-guided, facial-recess approach to the middle ear: Demonstration of the concept of percutaneous cochlear access in vitro," *Otology and Neurotology,* 26, 557-562, July 2005.

69. M. R, Fenlon, A. S. Jusczyzck, P. J. Edwards, and A. P. King, "Locking acrylic resin dental stent for image guided surgery," *The Journal of Prosthetic Dentistry*, 83(4):482-5, 2000.

70. J. M. Fitzpatrick, R. Balachandran, and R. F. Labadie, "Bite-Block Relocation Error in Image-Guided Otologic Surgery", *Medical Image Computing and Computer-Assisted Intervention*, 2004.

71. P. J. Edwards, A. P. King, C. R. Maurer Jr., D. A. de Cunha, D. J. Hawkes, D. L. G. Hill, R. P. Gaston, M. R. Fenlon, A. Jusczyzck, A. J. Strong, C. L. Chandler, and M. J. Gleeson, "Design and Evaluation of a System for Microscope-Assisted Guided Interventions (MAGI)", *IEEE Transactions on Medical Imaging*, 19(11): 1082-1093, 2000.

72. M. Y. Wang, C. R. Maurer Jr., J. M. Fitzpatrick, and R. J. Maciunas, "An automatic technique for finding and localizing externally attached markers in CT and MR volume images of the head," *IEEE Transactions on Biomedical Engineering*, 43:627-37, 1996.

73. R. Balachandran, R.F. Labadie, and J.M. Fitzpatrick, "Validation of a fiducial frame system for image-guided otologic surgery utilizing BAHA® bone screws," *IEEE International Symposium on Biomedical Imaging: From Nano to Macro, 2006*, 518-521, 2006.

74. R. Balachandran, R. F. Labadie, and J. M. Fitzpatrick, “Clinical determination of target registration error of an image-guided otologic surgical system using patients with bone-anchored hearing aids,” Proceedings of SPIE Medical Imaging, 6509, 650930, 2007.

75. EO Richter, T Hoque, W Halliday, AM Lozano, JA Saint-Cyr: Determining the position and size of the subthalamic nucleus based on magnetic resonance imaging results in patients with advanced Parkinson disease. Journal of Neurosurgery 2004; 100:541-546, March 2004.

76. P. A. Starr, C. W. Christine, P. V. Theodosopoulos, N. Lindsey, D. Byrd, A. Mosley, and W. J. Marks Jr., “Implantation of deep brain stimulators into the subthalamic nucleus: Technical approach and magnetic resonance imaging-verified lead locations,” *Journal of Neurosurgery*, 97: 370–387, 2002.

77. R Balachandran, J Mitchell, B Dawant, and JM Fitzpatrick, “Evaluation of targeting frames for deep-brain stimulation using virtual targets,” *IEEE International Symposium on Biomedical Imaging: From Nano to Macro, 2007*, 1184-1187, April, 2007.

78. P.-F. D’Haese, E. Cetinkaya, P. E. Konrad, C. Kao, and B. M. Dawant, “Computer-Aided Placement of Deep Brain Stimulators: From Planning to Intraoperative Guidance,” *IEEE Transactions on Medical Imaging*, vol. 24, no. 11, 1469-1478, Nov, 2005.

79. K. L. Holloway, S. E. Gaede, P. A. Starr, J. M. Rosenow, V. Ramakrishnan, and J. M. Henderson, “Frameless stereotaxy using bone fiducial markers for deep brain stimulation,” Journal of Neurosurgery, 103:404–413, 2005.

80. J. M. Henderson, K. L. Holloway, S. E. Gaede, and J. M. Rosenow, “The application accuracy of a skull mounted trajectory guide for image-guided functional neurosurgery,” Computer Aided Surgery, 9(4): 155–160, 2004.

81. K Rijkers, Y Temel, V Visser-Vandewalle, L Vanormelingen, M Vandersteen, P Adriaensen, J Gelan, EA M. Beuls, The microanatomical environment of the subthalamic nucleus, Journal of Neurosurgery, 107:198–201, 2007.

82. J.B. West and C.R. Maurer, Jr., “Designing optically tracked instruments for image-guided surgery”, IEEE Transactions on Medical Imaging 23, 533-545 (2004).

83. P. G. Batchelor and J. M. Fitzpatrick, “A study of the anisotropically weighted Procrustes problem”, IEEE Workshop on Mathematical Methods in Biomedical Image Analysis, Hilton Head, SC (Jun 2000).

84. R. Balachandran, J. M. Fitzpatrick, and R. F. Labadie, “Fiducial registration for tracking systems that employ coordinate reference frames,” Proc. SPIE Medical Imaging 2005, San Diego, CA, vol. 5744, 134–145 (Feb 2005).

85. A. D. Wiles, A. Likholyot, D. D. Frantz, and T. M. Peters, “A statistical model for point-based target registration error with anisotropic fiducial localizer error,” accepted for publication in IEEE Transactions on Medical Imaging.